Conference Proceedings

ECE-GRC 2012

Graduate Research Conference
Electrical and Computer Engineering

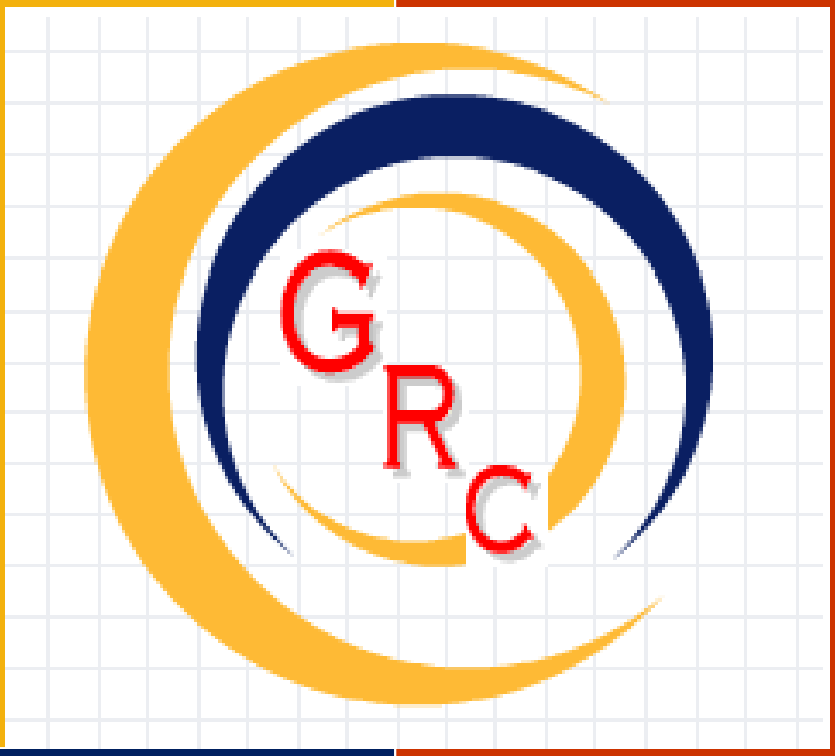

April 27th, 2012
Hilton UH Hotel & Conference Center
University of Houston

Conference Committee

General Chair
Dr. Pauline Markenscoff

Conference Coordination
MyTrang Baccam
Monica Sanchez

Financial Committee:
Dr. Steven Pei *Chair*

Judging Committee:
Dr. David Jackson
Dr. Ben Jansen
Dr. Jiming Bao

Technical Committee:
Dr. Wanda Wosik *Chair*
Sohini Sengupta
Anthony Lau

Communications Committee:
Dr. Bhavin Sheth *Chair*
Ruoli Jiang
Nitin Kushawaha

Local Arrangements Committee:
Dr. Ji Chen *Chair*

Printing is provided by **Texas Learning & Computation Center**

The 2012 CDC/GRC

gratefully acknowledges generous

support received from our

sponsors

Schlumberger

bp

Texas Instruments

KIPP & ZONEN
SINCE 1830

LTC

UNIVERSITY of HOUSTON | ENGINEERING

Department of Electrical & Computer Engineering

8th Annual Graduate Research Conference

April 27, 2012

The Hilton UH Hotel & Conference Center

Houston, Texas

Capstone Design Conference

Program

8:00 - 8:55 am	Breakfast and registration, Waldorf Astoria Room 210, Lobby
8:55 - 9:00 am	Opening Ceremonies, Plaza Room 247
	• Opening Remarks by Dr. Pauline Markenscoff, Conference Chair
	• Welcome to Technical Sessions by Dr. Wanda Wosik
9:00 - 10:00 am	Technical Program - Oral Session A, Plaza Room 247
10:00 - 10:30 am	Remarks by
	• Dr. Rathindra Bose, VC/VP for Research and Technology Transfer
	• Dr. Badri Roysam, Chairman, ECE Department
10:30 - 10:45 am	Coffee Break, Waldorf Astoria Room 210, Lobby
10:45 - 11:30 am	Technical Program - Oral Session B, Plaza Room 247
11:30 - 12:30 pm	Lunch, Waldorf Astoria Room 210
12:30 - 1:00 pm	Plenary Presentation, Dr. Stefan Murry, Waldorf Astoria Room 210
1:00 - 3:00 pm	Technical Program - Poster Session C, Shamrock Room 261
3:00 - 3:45 pm	Technical Program - Oral Session D, Plaza Room 247
3:45 - 4:00 pm	Coffee Break, Waldorf Astoria Room 210, Lobby
4:00 - 5:00 pm	Technical Program – Oral Session E, Plaza Room 247
5:30 - 6:30 pm	Reception and Awards, Waldorf Astoria Room 210

GRC 2012 TECHNICAL PROGRAM

The Hilton UH Hotel & Conference Center

April 27, 2012

8:00 – 8:55 am **Breakfast**

8:55 – 9:00 am **Opening Remarks in Plaza**

Session A: BIOENGINEERING AND SENSING

Session Type: Oral
Time: 9:00 – 10:00 am
Location: Plaza
Faculty Chair: Dr. Joe Charlson

10:00 – 10:30 am **Welcoming Remarks and Addresses in Plaza**

10:30 – 10:45 am **Coffee Break**

Session B: IMAGING AND ELECTROMAGNETICS

Session Type: Oral
Time: 10:45 – 11:30 am
Location: Plaza
Faculty Chair: Dr. Jarek Wosik

Session C: POSTER PRESENTATIONS

Time: 1:00 – 3:00 pm
Location: Shamrock
Faculty Chair: Dr. Ji Chen

Section P1: Imaging

Session D: Networks And Controls

Session Type: Oral
Time: 3:00 – 3:45 pm
Location: Plaza
Faculty Chair: Dr. Don Wilton

3:45 – 4:00 pm **Coffee Break**

Session E: MATERIALS AND DEVICES

Session Type: Oral

Time: 4:00 – 5:00 pm
Location: Plaza
Faculty Chair: Dr. Jack Wolfe

5:30 – 6:30 pm **Reception and Awards Ceremony in Waldorf Astoria**

Plenary Presentation by
Dr. Stephan Murry
Applied Optoelectronics, Inc. (AOI)

12:30 am - 1:00 pm in Waldorf Astoria

Customers and Other Irritants

Engineers are trained to utilize problem-solving skills and available technology to create useful things. We spend many years in academia perfecting the technical and analytical knowledge, which we hope to employ in a career, which will offer us intellectual fulfillment and pecuniary reward.

Many of us end up working for companies in order to pursue these careers. When we do, we are forced to confront some very curious characters: customers and suppliers, investors and analysts, co-workers and managers, salespeople and politicians. All of these "stakeholders" have competing interests and engineers are often challenged to adapt our practice of engineering to balance the interests of all the parties that we encounter in our business lives.

While this adaptation can at first seem daunting, the good news is that real, solid, and factual information is the second-most-valuable thing in business (right behind cash, which is always #1). Engineers are trained to deal with information in a way that many other professionals are not, and this training can be employed profitably in business, but only if we recognize that analytical skills alone are not enough to succeed.

This talk will distill some lessons learned in making the transition from academic to businessperson. It will explore the similarities and differences between the academic world and the business world, focusing on the skills that are most needed in business and are often under-taught in academia.

We will explore how companies approach uncertainty, the paramount importance of communications skills in business life, the value of intellectual property (IP) to a corporation and how this IP is created, protected, traded, and utilized, and the role that engineers and scientists play in the business world.

We will discuss the lifecycle of a company and how the roles of the various stakeholders change as the company evolves (or devolves) with an eye towards elucidating those skills that are most needed at each stage in the company's development. Depending on our career goals, choosing the right industry in which to work and the right "fit" in a prospective employer are two of the most important decisions we will make. Practical strategies are very important.

Stefan Murry, Ph. D.

Dr. Murry received his B.S. and M.S. in Physics from the University of Houston, in 1994 Electrical and 1997, respectively, and his Ph. D. in and Computer Engineering also from the University of Houston in 1999. His research concerned high-powered semiconductor laser devices, including topics related to advanced crystal growth techniques, fabrication technologies, and heat dissipation in laser devices.

While at UH, Mr. Murry supported the Wake Shield Facility's three shuttle missions, including working as a Payload Specialist at the Johnson Space Center. In this capacity he extended the crystal growth techniques pioneered in the University's laboratories to the Wake Shield's orbiting laboratory.

In 1997, along with then-Associate Professor Thompson Lin, Dr. Murry participated in the founding of Applied Optoelectronics, Inc. (AOI), a company formed to commercialize the semiconductor technology developed at UH.

Dr. Murry has spent the last 15 years directing AOI's expansion from a niche supplier of mid-infrared lasers into the world's largest supplier of fiber-optic components and equipment for the cable television industry, and one of the largest manufacturers of fiber-optic devices overall. Dr. Murry has been responsible for AOI's global sales and marketing activities since its founding. Today, AOI employs over 750 people in Sugar Land, TX, Ningbo, China, and Taipei, Taiwan. The company's revenues are approaching $70 million annually, and it counts among its customers companies including Cisco Systems, Motorola, Amazon.com, Huawei, Microsoft, and more than 300 other companies in 27 countries around the world.

Dr. Murry lives in Houston, along with his wife Adrienne (a graduate of the UH Bauer College of Business in 2003) and two daughters, Caton (8) and Charlotte (5). He has served on the Board of Directors of the UH Cullen College of Engineering Alumni Association and in 2011 was awarded the Entrepreneurship/Innovation alumni award from the Association.

In addition to his professional activities, Dr. Murry is a nationally-ranked sailplane racing pilot who serves on the Board of Directors of the Greater Houston Soaring Association, where he is an active flight instructor.

THIS PAGE IS INTENTIONALLY BLANK

ABSTRACTS FOR ORAL PRESENTATIONS

DECODING REPETITIVE FINGER TAPPING MOVEMENTS WITH SCALP ELECTROENCEPHALOGRAHY

Andrew Y. Paek*, Harshavardhan Agashe, Jose L. Contreras-Vidal
Department of Electrical and Computer Engineering
University of Houston
Houston, TX 77204-4005

Abstract

In this study, we investigated if brain activity recorded with scalp electroencephalography (EEG) can be used to predict the finger movements of human subjects. The study called for healthy subjects to repetitively tap their index finger while finger position and EEG were recorded. A decoder was developed, which models the finger movements as a linear combination of EEG signals.

Introduction

A brain-machine interface (BMI) is a communication pathway between the brain and an external device. These BMI systems can be used to assist individuals with motor deficiencies such as paralysis or amputations. A BMI system requires a neural interface that can decode movement intentions from brain activity. Such decoders have been developed recently for hand movements, where researchers have been able to predict finger movements using invasive brain recording techniques such as neural spike recordings with implanted microelectrode arrays [1, 2] and brain rhythm recordings with electrocorticography (ECoG) [3, 4]. While potentially effective, these techniques require surgical intervention which may limit their applications as BMI. Scalp electroencephalography (EEG) provides a noninvasive alternative where it extracts neural activity from the surface of the scalp. The goal of this study was to investigate the feasibility of using scalp EEG to decode finger movements.

Methods

The study called for healthy subjects to perform a finger tapping task. In particular, the subjects were instructed to tap their right index finger in three times in rapid succession followed by a few second pause. While the subjects performed this task, brain activity was recorded with 64 channel scalp electroencephalography and index finger movements were recorded with a data glove that contained bend sensors across the finger joints.

The EEG and the finger recordings were low pass filtered (<3Hz) as previous studies have found that these low frequency brain rhythms play a large role in decoding hand movements. These low frequency signals served as the input for the decoder, which modeled the finger movements as a linear combination of signals from the EEG channels. The model also incorporates EEG data in temporal points in the past to predict the present finger movement. The decoder was trained and tested in a 10-fold cross validation scheme. The Pearson Correlation Coefficient between the predicted finger trajectories from the model and the observed finger trajectories were calculated as the accuracy of the decoder.

Results and Discussion

In the best case scenario, shape of the predicted trajectories appear to follow the general shape of the observed trajectories as shown in Fig 1A. Across all the subjects, the decoding accuracy has a median of r=.403 and peaks at r=0.704 as shown in Fig. 1B. The performance varies widely across subjects, which can be attributed to emotional states, physiological differences, and artifacts. A future study of interest would be to see if the decoder used in this study can be used with a subject to control a robotic finger or perform a virtual finger movement task solely through brain activity.

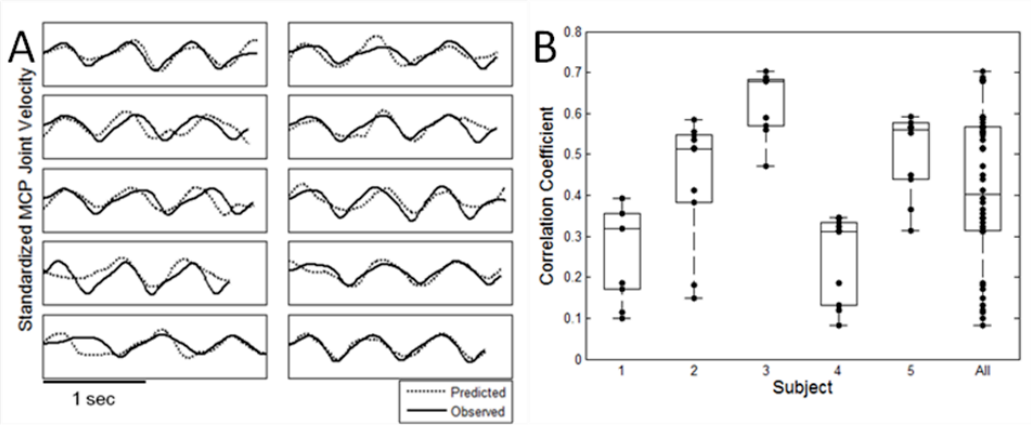

Fig. 1A. Examples of observed and predicted trajectories taken from the fold with the highest decoding performance. The decoded trajectory is shown as a dotted line while the observed trajectory is plotted as a solid line. **Fig. 1B.** Box plots of Pearson correlation coefficients of the decoder's predicted trajectories against the observed trajectories across the 10 cross validation folds for all subjects. Individual r-values from the 10 folds are plotted as dots overlaid over the boxplots. The boxplot on the right describes the distribution of r-values from all subjects.

References

[1] S. B. Hamed, M. H. Schieber, and a Pouget, "Decoding M1 neurons during multiple finger movements.," *Journal of neurophysiology*, vol. 98, no. 1, pp. 327-33, Jul. 2007.
[2] A. K. Bansal, C. E. Vargas-Irwin, W. Truccolo, and J. P. Donoghue, "Relationships among low-frequency local field potentials, spiking activity, and three-dimensional reach and grasp kinematics in primary motor and ventral premotor cortices.," *Journal of neurophysiology*, vol. 105, no. 4, pp. 1603-19, Apr. 2011.
[3] S. Acharya, M. S. Fifer, H. L. Benz, N. E. Crone, and N. V. Thakor, "Electrocorticographic amplitude predicts finger positions during slow grasping motions of the hand.," *Journal of neural engineering*, vol. 7, no. 4, p. 046002, May 2010.
[4] J. Kubánek, K. J. Miller, J. G. Ojemann, J. R. Wolpaw, and G. Schalk, "Decoding flexion of individual fingers using electrocorticographic signals in humans.," *Journal of neural engineering*, vol. 6, no. 6, p. 066001, Dec. 2009.

DEVELOPMENT OF FLEXIBLE MULTIMODAL NEURAL PROBES FOR STIMULATION AND RECORDING IN THE CENTRAL NERVOUS SYSTEM

Mufaddal M. Gheewala*[1], John C. Wolfe[1], Wei-Chuan Shih[1], John A. Dani[2]
Nanosystem Manufacturing Center
[1]Department of Electrical and Computer Engineering
University of Houston
Houston, TX 77204-4005
[2]Division of Neuroscience
Baylor College of Medicine
Houston, TX 77030

Abstract

Handcrafted "tetrodes", formed by twisting 4 wires together, fusing the insulation, and clipping off the end, are the preferred recording electrodes for monitoring in vivo neuronal unit activity from freely moving animals (usually rodents or non-human primates). This paper reports the development of a technology platform for fabricating integrated conductors and electrical contacts on fine, needle-like neural probes, including wires and optical fibers, for deep brain sensing and stimulation. The proof-of-concept device is a 65 μm optical fiber with 25 μm wide thin film conductors and 625 μm^2 contacts. Specifically, we demonstrate the formation of multiple conductor lines and contacts whose impedance in 0.9 % saline solution agrees well with model predictions.

Introduction

Neural probes having multiple modalities for sensing and stimulation can provide the means to better understand and possibly "reverse engineer" the brain. Electrophysiology has traditionally been the standard for neuronal recordings and stimulation. Advances in optical microscopy and other spectroscopy techniques as well as optogenetics have led to the evolution of a new modality for monitoring and controlling the neuronal signals. Integration of the two modalities – electrical and optical – can lead to transformational discoveries in neuroscience.

This project aims at developing a manufacturing technology for the fabrication of multimodal neural probes (optitrodes – see fig. 1) where tetrode type electrical contacts are integrated on the surface of an optical waveguide. Such a configuration has a wide range of functionality including 3-D mapping of action potentials in the cylindrical volume surrounding the tetrode, optogenetic control of neuronal signals with high spatial resolution and genetic specificity, optical monitoring of hemodynamic and ion channel activity and characterization of tissue impedance. Multi-tier electrical recording sites along the optitrodes can achieve stimulation of and 3-D recording from different neuronal layers simultaneously.

High throughput along with low cost fabrication of these optitrodes largely relies on parallel processing techniques such as DC magnetron sputter deposition (for metal coating), sputter etching/reactive ion etching, plasma enhanced chemical vapor deposition having nanoscale conformity (for resist and dielectric coatings) and neutral particle lithography, a diffraction free, nanoscale resolution, high throughput parallel printing, proximity exposure technique. Alignment of the probes for patterning the conductor lines is achieved by using a micro-machined silicon jig (fig. 2). Grooves on the

opposite side of the jig intersect those holding the probes to form a perfectly aligned conductor mask. Finally, nanoporous gold contacts provide ultra-low impedance for these optitrodes. Low contact impedance reduces the thermal noise (v_n α √R) which in turn increases the signal-to-noise ratio (SNR).

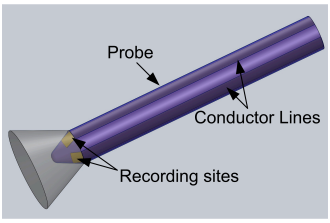

Fig. 1. Probe concept with electrical recording sites on a flexible, light-guiding substrate. The cone represents a light beam radiating from the probe tip.

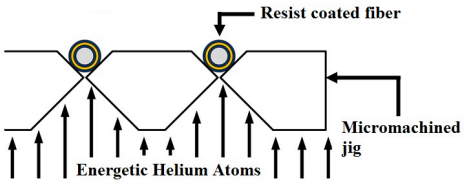

Fig. 2. Micromachined jig for aligning conductor masks with probe fibers. Flooding the mask with energetic helium atoms transfers the mask pattern to the resist on the fibers.

Beyond this project, we also envisage next generation of optitrodes having multiple tiers of tetrodes integrated on multimode optical fibers having openings for light delivery along the length of the fiber. Such probes could also find use in a wide variety of application in neuromuscular stimulation and creating brain-machine interfaces that will one day enable paralyzed patients to move under their own volition.

References

[1] M. Gheewala, S.-T. Lin, W.-C. Shih, J. A. Dani, J. C. Wolfe, "A multi-tiered tetrode with an integrated optical channel for neuronal unit recording with localized light delivery," *Society for Neuroscience*, Washington DC, November 12-16, 2011

[2] Mufaddal Gheewala, John C. Wolfe, John A. Dani, Wei Chuan Shih, "Fabrication of 3D multisensing optrodes for in vivo neuronal unit recordings", *ECE Graduate Research Conference at UH*, Houston, TX, April 29, 2011

[3] Szu-Te Lin, Mufaddal Gheewala, John C. Wolfe, John A. Dani, Wei Chuan Shih, "A Flexible Optrode for Deep Brain Neurophotonics", *IEEE EMBS Conference on Neural Engineering of the IEEE Engineering in Medicine and Biology Society*, Cancun, Mexico, April 27 - May 1, 2011

[4] J. C. Wolfe, M. M. Gheewala, W-C. Shih, J. A. Dani, "Fabrication of 3D multisensing neural probes for single unit recording", *Society for Neuroscience*, San Diego, CA, November 13-17, 2010.

[5] Dhara Parikh, Barry Craver, Hatem N. Nounu, Fu-On Fong, and John C. Wolfe, "Nanoscale Pattern Definition on Nonplanar Surfaces Using Ion Beam Proximity Lithography and Conformal Plasma-Deposited Resist," *Journal of Microelectromechanical Systems*, vol. 17, no. 3, Jun. 2008.

[6] J. C. Wolfe and B. P. Craver, "Neutral particle lithography: a simple solution to charge-related artefacts in ion beam proximity printing", *J. Phys. D: Appl. Phys.* 41, Jan. 2008.

DEVELOPMENT OF SELF-ALIGNED INTER-DIGITATED ELECTRODES WITHIN A MICROFLUIDIC CHANNEL FOR AN ELECTROCHEMILUMINESCENCE SENSOR

Gauri A. Samel* and Paul Ruchhoeft
Nanostructures Laboratory
Department of Electrical and Computer Engineering
University of Houston
Houston, TX 77204-4005

Abstract

The aim of this project is to fabricate microchannels with inter-digitated electrodes from an SU-8 photoresist that can be used for diagnostics in an electrochemiluminescence platform. The microfluidic channels were formed by contact lithography using SU-8 and the pattern contained an array of fins that were the basis for forming inter-digitated electrodes. The design of the fins allows for self-aligned deposition of metal at angles without the need for lithographic or etching steps. The fabrication also included the optimization of the pre-exposure bake, exposure dose, post exposure bake, and the development time and bath setup. The channel contains a 4mm long array of fins that are 20 microns wide and 50 microns tall. The structure will be electrically evaluated to ensure that the electrodes are continuous and, given enough time, electrochemiluminescence will be studied within the channel.

Introduction

Microfluidic devices have gained popularity because of advantages they offer over macro-channel devices, including easy manipulation and control of fluids within the channel, increased contact area of fluids with the channel walls hence, improved sensitivity, and reduced reagent volumes [1]. SU-8 2050 polymer is a popular choice in fabricating these devices since it allows for the fabrication of structures with very high aspect ratio, and is mechanically and thermally stable [2]. The microfluidic channel for this work consists of an inter-digitated design of fins where each alternate fin will be connected to the positive or negative electrode respectively by double-angled evaporation technique. The device formed will be used to demonstrate electrochemiluminescence effect within the channel on applying an electric field across the electrodes.

Method

The microfluidic channels were formed by spin coating the SU-8 epoxy resist, exposing the resist by contact lithography, implementing pre- and post exposure bakes, and a development step. While fabricating micro-channels with the recommended process parameters, there were several issues like under exposure, stress related problems such as buckling and cracking of walls, and shorting of electrodes. Hence, the processing parameters were optimized and the channel thus obtained was devoid of any stress effects as seen in Figure 1.

Double-angled evaporation technique was implemented to form the contact electrodes as well as to coat walls of the channel. This technique takes advantage of the channel walls ability to cast shadows in metal evaporation step that allows the coating of the fin sidewalls without shorting the electrodes.

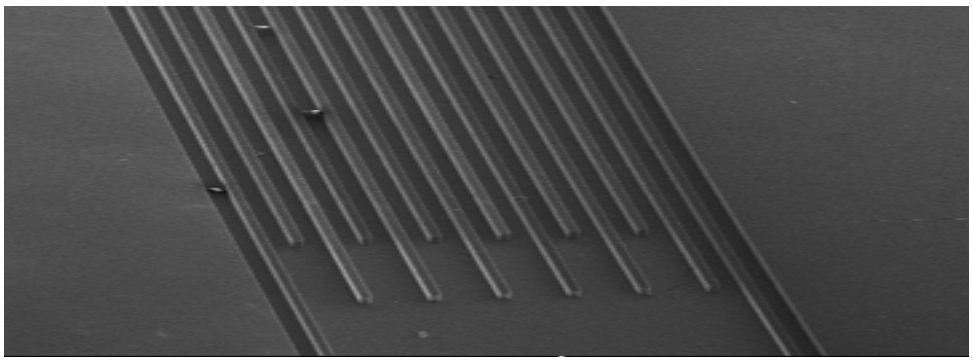

Fig. 1. Microfluidic channel obtained after optimizing fabrication steps

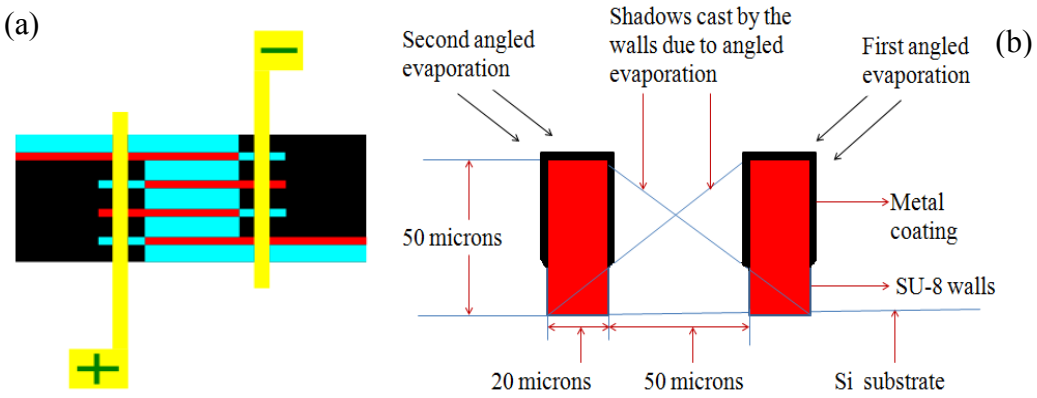

Fig. 2. (a) Top view of microfluidic channel. The long L-shaped electrodes are connected alternately to the fins by angular evaporation. The region coated with metal is the black region whereas the region uncoated with metal is the blue region. (b) Side view of the channel. Double angled evaporation prevents coating of metal on the regions shadowed by the sidewalls.

Summary and Future Work

Microfluidic channels have been fabricated successfully after resolving stress effects on the polymer and optimizing fabrication steps. Presently, work is being carried out on coating the channel walls to form electrodes. The channel will then be sealed with a glass slide and be tested for its resistivity by flowing de-ionized water and buffer solutions through it. On obtaining expected resistance values for DI water and buffer solution will conclude that, the electrodes thus formed are non-shorting and the technique of coating the channel walls by double-angle evaporation has been implemented successfully.

References

[1] E. Verpoorte and N. Rooij, "Microfluidics Meets MEMS," *Proceedings of the IEEE,* vol. 91, no. 6, pp 930-948, June, 2003.
[2] A. Campo and C. Greiner, "SU 8: a photoresist for high aspect ratio and 3D submicron lithography," J. Micromechanics and Microeng., vol. 17, R81, March, 2007.

RF-ELECTROMAGNETIC FIELDS INDUCED HEATING OF NANOCONSTRUCTS FOR CANCER THERAPEUTICS

Rohit Pande[*1,2], Wanda Zagozdzon-Wosik[1,2], Leiming Xie[2], Srimeenakshi Srinivasan[3], Biana Godin[1,3], and Jarek Wosik[1,2]
Microwave Characterization and High Frequency Bio-Engineering Group
[1]Department of Electrical and Computer Engineering,
[2]Texas Center for Superconductivity, University of Houston, Houston, TX 77204;
[3]Department of Nanomedicine, The Methodist Hospital Research Institute, Houston, TX 77030.

Abstract

Rapid advances in nanotechnology have led to the development of silicon based micro sized nanoporous vectors with nanopores of different sizes to accommodate drugs and nanoparticles such as gold, silica and iron oxide particles. In order to evaluate potential of these nano-vectors for hyperthermia and/or drug delivery, *rf* thermal properties of both magnetic and non-magnetic nanoparticles must be understood. In this work, in order to characterize metallic, dielectric, and magnetic types of nano-vectors' components and to study their *rf* heating efficiency, we have constructed a setup that employs both *rf* electric and magnetic fields in the MHz frequency range. The sample to be characterized was exposed either to *rf* magnetic or *rf* electric fields. We measured specific absorption rates (SAR) for gold, silica and iron oxide nanoparticles suspended in water based solutions. In order to evaluate SAR of only nanoparticles, the nanoparticles were separated from their colloidal suspensions by centrifugation and filtration and then characterized. We also studied the effect of change in the ambiance of nanoparticles (silica) by adding proteins like bovine serum albumin (BSA). Albumin concentrations from 0.5% to 4% w/v were used to prepare such surface-modified particles. Based on obtained results, feasibility of the development of clinical methods utilizing *rf* heating of nanoparticles uploaded into porous silicon micro particles will be discussed.

Introduction

Clinical effectiveness of heat therapeutics for cancer treatment has been well established for the past several years. Malignant tumors are known to be treated by *rf* hyperthermia and *rf* ablation techniques, in which cell temperatures are elevated to therapeutic levels of about 43-45 °C and above 56 °C, respectively.[1] However, insufficient temperature rise in tumor sites, poor temperature distributions, lack of selectivity and sometimes overheating leading to organ damage are the known demerits. Emerging field of nano-medicine and its innovative developments has given significant impetus to the research of cancer-treatment and its detection at early stages. By systemic injection of engineered nano-constructs and nano-vectors into the blood, chemotherapeutic agents and nanoparticles could be targeted to tumor sites while sparing normal cells.[2] Excellent tissue penetration of *rf* electromagnetic fields together with the nanoparticles serving as heating enhancers renders a targeted hyperthermia for medical diagnostics. Magnetic hyperthermia using iron oxide particles and its clinical trials have been reported. Hyperthermia using capacitively coupled *rf* fields has also been shown on gold nano-particles. To optimize nanoparticles for hyperthermia applications it is important to estimate their heat generation in terms of SAR, which is affected by various factors including nanoparticle coating or functionalization.

Design and Methodology

The schematic of the setup to investigate hyperthermia is shown in Figure 1. The apparatus is based on a high-Q LCR resonant circuit consisting of a solenoid and a parallel plate capacitor, which were built using oxygen free copper metal. Single crystal sapphire was chosen as a low-loss high dielectric constant material and as a sink for heat dissipation. The samples to be characterized are placed in a quartz tube and could be either a part of the solenoid or/and the capacitor. For temperature measurements, we used GaAs's band-gap based optical temperature sensor.

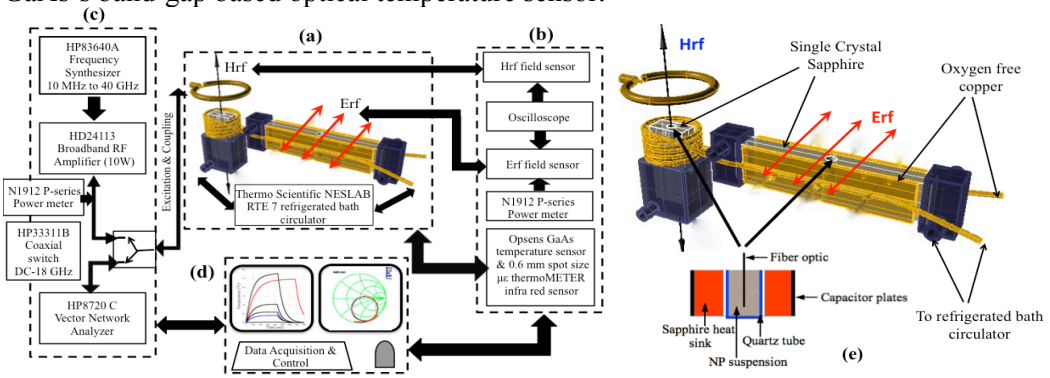

Fig. 1. (a) RLC resonator (b) Powering & coupling module (c) System parameters' measurement module (d) Computer controlled I/O module (e) Sample in capacitive cavity (expanded view).

Results and Conclusions

To characterize, nanoparticles encapsulated by the silicon nanovectors, thermographic data for gold, silica and SPIO nanoparticles are obtained following 400 seconds of exposure in *rf* electromagnetic fields. By dosimetric analysis, SAR values for the particles were calculated and compared with values known from literature. Influence of albumin on heating efficiency of silica particles modified in 0.5, 1, 2 and 4 % w/v albumin solution was investigated and it was concluded that adding albumin concentrations increases SAR of the bare silica particles (Fig. 2).

Particle	Conductivity of Supernatant filtered	SAR	
		E Field	H Field
10nm Au	1.57E-02	4.67E+05	4.78E+06
100nm Au	7.86E-03	8.47E+05	1.59E+06
100nm SiO2	8.17E-03	1.82E+03	3.14E+03
200nm SiO2	6.33E-03	2.21E+03	2.19E+03
10nm SPIO (1/8th)	2.01E-02	2.23E+05	2.35E+06
10nm SPIO (1/64th)	4.55E-03	1.66E+05	1.34E+06

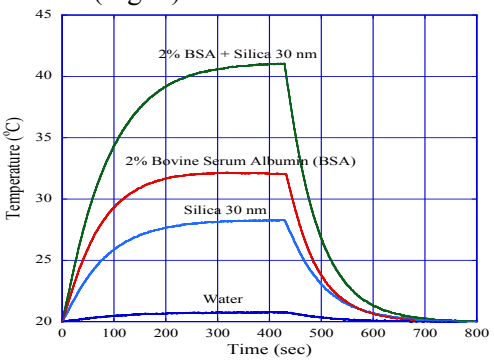

(a) (b)

Fig. 2. (a) Electric field and Magnetic field SAR extracted for gold, silica and SPIO nanoparticles. (b) Albumin enhanced heating for 30 nm silica particle in 2% w/v BSA solution.

References

[1] Paul Cherukuri et al., "Targeted hyperthermia using metal nanoparticles," *Advanced Drug Delivery Reviews*, vol. 62, pp. 339, 2010.

[2] B. Godin et al. , "An integrated approach for the rational design of nanovectors for biomedical imaging and therapy," *Adv Genet*, vol. 69, pp. 31, 2010.

A NOVEL ACTIVE LEARNING ALGORITHM FOR IDENTIFICATION OF CELL TYPES IN MULTIPLEX-STAINED HISTOPATHOLOGY IMAGES

R. Padmanabhan[1], V. Somasundar[1], B. Roysam[1], X. Liao[2], L. Carin[2], J. Hu[3], J. Zhu[3], and W. Lee[3]

[1] ECE Department, University of Houston, Houston, TX-77204

[2] ECE Department, Duke University, Durham, NC-27708

[3] Perelman School of Medicine, University of Pennsylvania, PA-19104

Abstract

Quantitative cell-based analysis of histopathological specimens requires a system for reliable identification of cell types. Unfortunately, experts introduce subjectivity and selection bias, and expend excessive effort, as they cannot judge the *quantitative* contribution of examples to machine learning. To overcome these limitations, we present a novel accelerated learning algorithm that *actively* aids the human expert in example selection.

Introduction

Histopathological analysis and angiogenic activation in human renal cell carcinomas requires a system for rapid, reproducible identification of endothelial cells and cell type-specific quantification of analyte expression. Training a classification algorithm requires the human expert to provide training examples. Human trainers are poor judges of the degree to which each new example is informative. This introduces subjectivity and selection bias. Our clinical study of angiogenic activation in human clear-cell renal cell carcinomas (ccRCC) and soft tissue sarcomas (STS) requires automated quantification of large batches (200 – 300 images/batch, ~1000 cells/image) of multi-spectrally imaged slides. Cell type identification algorithms are designed to learn from examples provided by a human expert. To overcome limitations due to imperfect human decisions, we present a novel algorithm based on the mathematical principle of submodularity [1] that *actively* aids the human expert in example selection. Given only one initial example of each cell type, this method automatically searches the cell measurements to identify the mathematically most informative subsequent examples for the user to label. This procedure converges rapidly, in about 10 iterations, and the convergence of machine learning is sensed automatically. Then, all cells in the batch of images are automatically labeled by type.

Analysis and Results

Deparaffinized formalin-fixed, paraffin-embedded ccRCC and STS sections were rehydrated and multiplex immunostained against various biomarkers to identify cell types of interest. Cell nuclei were segmented automatically [2], and their sizes, shapes, and chromatin texture were quantified. Other channels were quantified by association in 3-pixel wide perinuclear regions. These measurements were provided as input to the proposed algorithm. For the STS data, the method achieved a Positive Predictive Value (PPV) of **0.989** and a Negative Predictive Value (NPV) of **0.996** indicating excellent sensitivity and specificity. Performance of the method was quantified against full manual analysis (Table 1). For the ccRCC images, it achieved an accuracy of **95%** with just 60 examples when classifying tumor cells (TC) vs. endothelial cells (EC).

Table 1: **Confusion Matrix for EC identification (STS Data)**

		Manual Analysis (# cells)		
		EC	**Non-EC**	**Total**
Active Learning	**EC**	3,312*	106†	3,418
	Non-EC	352γ	71,316ψ	71,668
	Total	3,664	71,422	**75,086**

* True Positives, †False Positives, γFalse Negatives, ψTrue Negatives

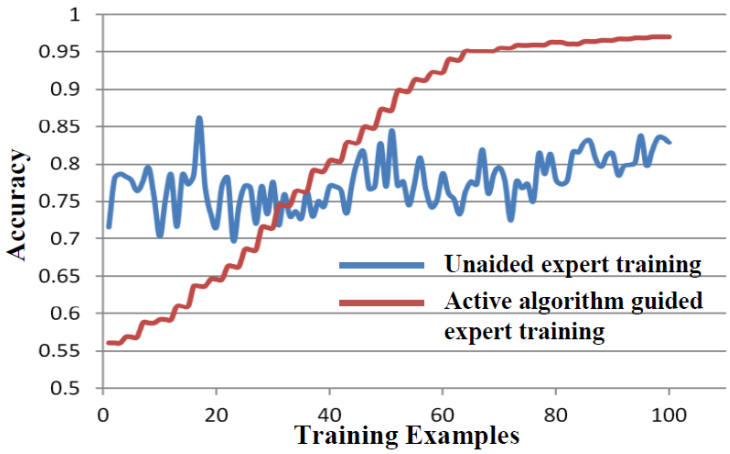

FIG.3. (Left) Comparison of unaided expert training performance (blue) with the active algorithm (red) for Tumor vs. Endothelial cell method in ccRCC slides (3,900 cells). The proposed method (red) achieves an accuracy of 95% with just 60 examples, and shows monotonic improvement. The performance of the unaided human trainer (blue) is much less accurate, and more variable, even after 100 examples.

References

[1] G. Nemhauser et al., *Mathematical Programming*, 14, 1978.
[2] Y. Al-Kofahi et al., *IEEE Trans Biomed Eng.*, vol. 57, 4, pp. 841-52, 2010.

Acknowledgement

This work was sponsored by NIH grants R01 EB005157-01, RO1 CA135509 & Defense Advanced Research Projects Agency (DARPA) MTO under the auspices of Dr. Jack Judy through the Space and Naval Warfare Systems Center, Pacific Grant/Contract No. N66001-11-1-4015

MICROWAVE DIELECTRIC RESONATORS FOR CHARACTERIZATION OF YBCO THIN FILMS LOSSES IN NORMAL AND SUPERCONDUCTING STATES

D. Ketharnath*[1,3], J. Krupka[4], E.Galstyan[2,3], V. Selvamanickam[2,3], and J. Wosik[1,3]
[1]Electrical and Computer Engineering Dept
[2]Mechanical Engineering Dept
[3]Texas Center for Superconductivity
University of Houston, Houston, USA
[4]Department of Electronic and Information Technology
Warsaw University of Technology, Poland

Abstract

We report on the non-destructive microwave frequency characterization of superconducting films. Single-post dielectric (SPDR) and rutile rod dielectric resonators operating at 9.4 GHz in quasi $TE_{01\delta}$ and at 13 GHz in TE_{011} modes were used to explore the correlation between superconducting and normal state surface resistance (R_s) of YBCO tapes. The SPDR with barium zirconium titanate (BZT) ceramic as the dielectric was used to measure the complex conductivity of the YBCO tape at normal state and the phase transition state while the rutile rod resonator was used for measurements in the superconducting state. The investigated tapes were made of $YBa_2Cu_3O_{7-x}$ films on Hastelloy-supported buffer and were deposited using the MOCVD technique. The buffer stack consists of aluminum oxide (Al_2O_3), yttrium oxide (Y_2O_3), and textured IBAD-MgO and $LaMnO_3$ layers [1]. Numerical simulations are done using Finite Element Method (FEM) in order to accurately evaluate the Q-factor and resonant frequency shifts for different sample conductivity and thickness. All simulations are performed using the commercially available software package HFSS (Ansoft Corporation). Experimental values of resonance frequency shifts and Q-factor are matched with the numerical simulations to extract the accurate conductivity of the YBCO tape.

Introduction

The HTS tapes in energy applications are constantly accessed for quality control of in-plane texture and uniformity by X-ray diffraction method. However, these tools do not provide direct information on the expected critical current performance of the film. To that end, our objective is to develop a non-contact evaluation technique that could correlate normal state properties during MOCVD film growth to superconducting properties. Majority of methods intended for characterization of material properties of superconductors at microwave frequencies employ resonators since they exhibit high sensitivity due to their large Q-factor values.

Design and Methodology

High sensitivity and Q-factor of the rutile rod dielectric resonator is utilized in the accurate loss measurements of the YBCO tapes in superconducting state since in this state the Q-factor predominantly depends on the losses in the sample due to negligible parasitic losses. The resonance and Q-factor shift are determined as the difference between resonator with superconducting sample and with a reference bulk copper sample. Above critical temperature (T_c) the sample is semi-transparent to electromagnetic field and hence R_s depends on the electrical properties of the film as well as the metal surfaces

behind the substrate. Since at higher temperatures the measured Q-factor of rutile rod resonator decays rapidly and becomes too low to extract Rs at normal state, for measurements above T_c, BZT ceramic SPDR resonators were used. The Q-factor due to the presence of superconducting film can be obtained from the formula, $Q_{YBCO}^{-1} = Q_s^{-1} - Q_{parasitic}^{-1}$, where, Q_{YBCO}, Q_S and $Q_{parasitic}$ are the Q-factors due to losses in the sample, measured sample under test and parasitic losses respectively. Figure 1 (a) and (b) show the schematic representation of the resonators used in the normal and superconducting state measurement respectively.

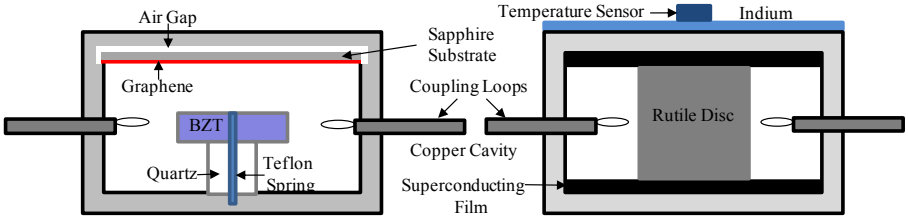

(a) (b)

Fig.1. Schematic representation of a) $TE_{01\delta}$ mode 13 GHz BZT SPDR ε_r is 27.93 at 300 K b) $TE_{01\delta}$ mode 9 GHz Rutile rod resonator ε_r is108 at 77 K.

Results and Discussion

Using two different configurations of SPDR and rutile rod resonator, the effective R_s of Hastelloy, Hastelloy/buffer/YBCO were measured at normal state and superconducting state. The simulated values of Q-factor and resonant frequency shift along with the experimental values are used to extract R_s of the YBCO tapes.

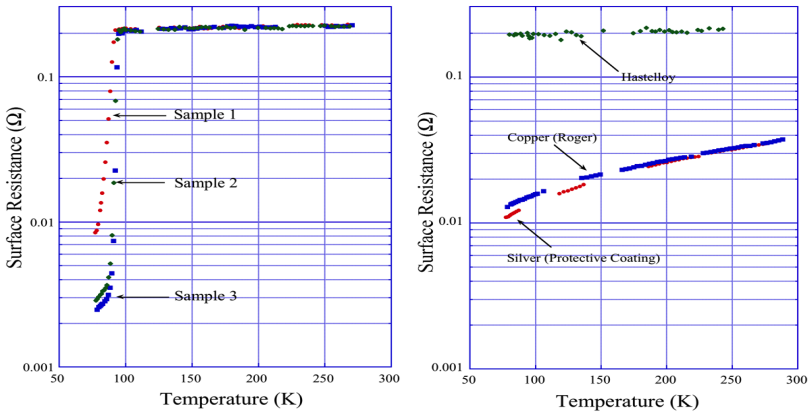

(a) (b)

Fig.2. Surface resistance R_s *vs*. temperature measured for (a) three $Zr_{0.06}Gd_{0.6}Y_{0.6}Ba_2Cu_3O_7$ samples (b) Hastelloy substrate; silver and copper measured for comparison.

References

[1] Y. Chen, V. Selvamanickam, Y. Zhang, Y. Zuev, C. Cantoni, E. Specht, M. Paranthaman, T. Aytug, A. Goyal, and D. Lee, "Enhanced flux pinning by $BaZrO_3$ and $(Gd,Y)_2O_3$ nanostructures in metal organic chemical vapor deposited GdYBCO high temperature superconductor tapes." *Appl. Phys. Lett.*, 94(6):062513–3, February 2009.

[2] J. Krupka and W. Strupinski, "Measurements of the sheet resistance and conductivity of thin epitaxial graphene and sic films". *Appl. Phys. Lett.*, 96(8):082101–3, February 2010.

ANALYSIS OF A LINEAR SERIES-FED RECTANGULAR MICROSTRIP ANTENNA ARRAY

Sohini Sengupta*, David R Jackson, and Stuart A Long
Applied Electromagnetics Laboratory
Department of Electrical and Computer Engineering
University of Houston
Houston, TX 77204-4005

Abstract

A simple yet accurate method of analysis for a linear series-fed microstrip antenna array is proposed here. This method involves relating the current on a given patch to the currents at the feed points on either side of the patch (i.e. direct coupling), and to the currents on the other patches in the array (thus accounting for mutual coupling). The approach used here results in a system of linear equations where the unknowns are the currents on the patches and the currents at the feed ports on the left and right edges of the patches. The solution of the system of equations thus gives the desired currents and voltages, from which the radiation characteristics and input impedance can be easily calculated for the array. The method of analysis proposed here combines the simplicity of a CAD approach with the accuracy of a full-wave numerical analysis.

Introduction

Linear series-fed arrays of microstrip antennas are frequently used for applications requiring antennas with moderately high gain where a minimum size of the feed network is desired [1-10]. Linear series-fed microstrip antenna arrays are compact, take up less real estate and have lower line radiation compared to other types of arrays such as those with a corporate feed network. The main disadvantage of linear series-fed microstrip antenna arrays is that they tend to be narrowband and the beam scan angle is quite sensitive to the frequency. However, due to the high sensitivity of the beam scan angle to frequency, a series-fed microstrip array can also be used as a frequency-scanned array. A typical linear series-fed microstrip array is shown in Fig.1. Usually, the array is fed at one end, with a load at the other end.

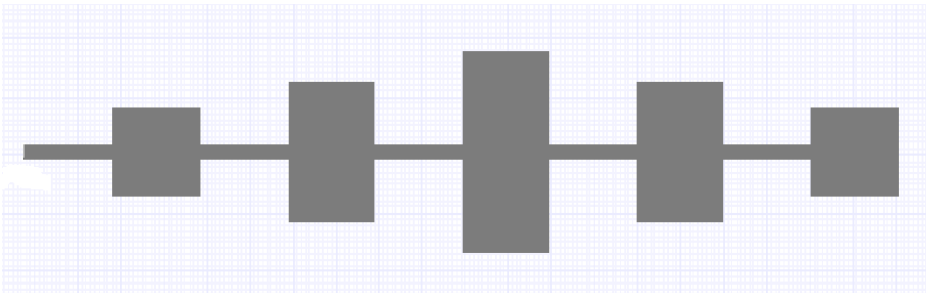

Fig.1. A typical linear series-fed microstrip antenna array fed at one end (on the left) with the other end left open-circuited.

A system of equations is developed by relating the currents at the feed ports on each patch and the currents on the patch elements using a set of defined canonical coefficients. The system of equations, having included the effects of mutual coupling between the

elements, can be solved for the unknown currents. This then yields the solution for the amplitude distribution, radiation pattern and input impedance of the array. The canonical coefficients can be found analytically or from simulations of a single element in Ansys Designer or HFSS. The amplitude distribution, radiation pattern and input impedance obtained from the proposed analysis are compared to the results of simulations using full-wave simulation software tools (Ansys Designer and Ansys HFSS), and also the simple transmission-line model.

Conclusions

The patch current amplitude distribution, radiation pattern and input impedance predicted by the proposed analysis method compare well with the results of full-wave simulations using Ansys Designer and Ansys HFSS. The proposed method of analysis has an accuracy comparable to that of the full-wave simulation methods without requiring full-wave numerical analysis of the entire array. The transmission-line model, which is often used to analyze series-fed microstrip antenna arrays, proves to be inadequate as it neglects feed reactance and mutual coupling. Thus the method of analysis proposed here can be used as an efficient tool in the analysis and design of large linear series-fed microstrip antenna arrays.

References

[1] R. Garg, P. Bhartia, I. Bahl, and A. Ittipiboon, *Microstrip Antenna Design Handbook*, Artech House, Boston/ London, 2001.

[2] R. B. Waterhouse, *Microstrip Patch Antennas: A Designer's Guide*, Kluwer Academic Publishers, Boston/Dordrecht/London, 2003.

[3] B. B. Jones, F. Y. M. Chow, and A. W. Seeto, "The Synthesis of Shaped Patterns with Series-Fed Microstrip Patch Array," *IEEE Transactions on Antennas and Propagation*, vol. AP-30, no. 6, Nov. 1982.

[4] T. Metzler, "Microstrip Series Arrays," *IEEE Transactions on Antennas and Propagation*, vol. AP-29, no. 1, January 1981.

[5] S. Otto, O. Litschke, J. Leib, and K. Solbach, "A Unit Cell Based Low Side Lobe Level Design for Series-Fed Array Antennas," *Proc. of the 2008 Asia-Pacific Microwave Conference (APMC)*, 10.1109/APMC.2008.4958556.

[6] D. G. Babas and J. N. Sahalos, "Synthesis Method of Series-fed Microstrip Antenna Arrays," *Electronics Letters*, vol. 43 no. 2, 18th Jan. 2007.

[7] C. Niu, J. She, and Z. Feng, "Design and Simulation of Linear Series-Fed Low Sidelobe Microstrip Antenna Array," *Proc. of the 2007 Asia-Pacific Microwave Conference (APMC)*.

[8] S. Otto, A. Rennings, O. Litschke, and K. Solbach, "A Dual-Frequency Series-Fed Patch Array Antenna," *Proc. of the 2009 European Conference on Antennas and Propagation (EuCAP)*.

[9] Z. Chen and S. Otto, "A Taper Optimization for Pattern Synthesis of Microstrip Series-Fed Patch Array Antennas," *Proc. of the 2nd European Wireless Technology Conference*, Rome, Italy, Sept. 2009.

[10] T. Yuan, N. Yuan, and L.-Wei Li, "A Novel Series-Fed Taper Antenna Array Design," *IEEE Antennas and Wireless Propagation Letters*, vol. 7, 2008.

SUPPORTING PER-FLOW END-TO-END QUALITY OF SERVICE PROVISIONING IN PACKETIZED OPTICAL BURST SWITCHING NETWORKS

Yiyong Zha* and Yuhua Chen
Systems Research Laboratory
Department of Electrical and Computer Engineering
University of Houston
Houston, TX, 77204-4005

Abstract

Optical Burst Switching (OBS) is one of the most promising solutions to DWDM based optical networks by avoiding the shortcomings of optical packet switching and optical circuit switching. However, lack of packet-level traffic management support is a major drawback of traditional OBS networks. In this paper, we propose a Packetized Optical Burst Switching Network to support arbitrary per-flow queueing schemes, which have both bandwidth and latency control. In particular, we propose a new algorithm with end-to-end QoS guarantee in Packetized OBS networks. The resulted resource allocation ensures the end-to-end QoS by providing absolute delay guarantees.

Introduction

In OBS networks, schedulers at the edge router operate at the granularity of formed bursts, which are collections of thousand of packets. New scheduling algorithms operated at the packet level are needed to meet the demand for better end-to-end Quality of Service (QoS) and delay sensitive applications. The well-known fair queuing scheduler Stratified Round Robin [1] has been designed to provide a bounded delay with a simple hardware implementation. The drawback of SRR is that it does not provide arbitrary end-to-end QoS guarantee when assigning weights. We stress that the end-to-end delay is a significant performance measure in end-to-end QoS provisioning in the service delivery system.

Methodology and Results

In this paper, we propose a Packetized Optical Burst Switching Network by extending virtual burst assembly to provide bandwidth to individual flows while flows share the optical bursts in the core network. In the scheduler's point of view, in order to serve the incoming traffic flows with some required service guarantees, the amount of resources that is assigned to the flow needs to be predetermined.

Under the network calculus [2] framework, for a system S with input and output functions R and R^*, a service curve $S(t)$ is possible, if $R^*(t) \geq R(t) \otimes S(t)$. The virtual delay in a work conserving fashion scheduler such as GPS, SRR, FIFO schedulers is defined as the time needed to handle the backlog traffic in the. The backlog at time t is defined as $B(t) = R(t) - R^*(t)$, thus, the delay is defined as:

$$B(t, d(t)) = 0$$

$$d(t) = \inf_{\tau \geq 0} \{R(t) \leq R^*(t+\tau)\}. \quad (1)$$

Applying the leaky bucket constraint to the input such as the arrival traffic is regulated by the arrival curve $A(t) = \min\{pt, qt + b\}$, the bandwidth allocation of a certain delay requirement can be predicted by:

$$r_{al} = \left\{ \begin{array}{l} \dfrac{pb}{(d_{re} - T_{tol})(p-q) + b}, T_{tol} - \dfrac{b}{p-q} \leq d_{re} \leq T_{tol} + \dfrac{b}{q} \\ q, d_{re} \geq T_{tol} + \dfrac{b}{q} \end{array} \right\} \quad (2)$$

In Fig. 1, the results show that the delay requirement is the upper bound for the delay of each packet. This means the proposed method can provide an end-to-end delay guarantee. As shown in Fig. 2, the end-to-end delay reduces as more bandwidth is allocated to the flow. The delay converges when the assigned bandwidth goes beyond the peak rate.

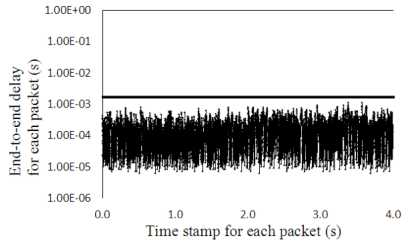

Fig. 1. Delay obtained from simulation compare to the delay requirement

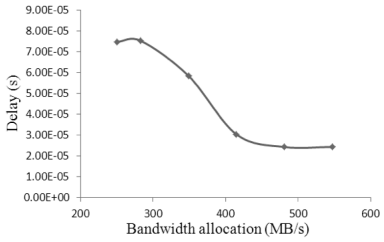

Fig. 2. Delay obtained from simulation with different bandwidth allocation

Conclusions

We proposed a novel bandwidth allocation algorithm to provide end-to-end QoS guarantee in Packetized OBS networks. Bandwidth assigned to each flow is based on our derived mathematical model on the end-to-end delay requirement. With this optimization, resource allocation in OBS networks can be performed dynamically. The minimum amount of resource assigned to each flow (application) is based on its delay requirement to provide the end-to-end delay guarantee.

Acknowledgment

This work was supported in part by the National Science Foundation (NSF) under Grant CNS-0708613, 0923481, 0926006, and the Texas Advanced Research Program (ARP) under Grant G096059.

References

[1] S. Ramabhadran and J. Pasquale, "The Stratified Round Robin Scheduler: Design, Analysis and Implementation," *IEEE/ACM Transactions on Networking, vol.14, no.6*, pp.1362-1373, Dec. 2006.

[2] J. L. Boudec and P. Thiran, "Network calculus: a theory of deterministic queueing systems for the Internet", *Springer Verlag LNCS 2050*, June 2001.

NON-RETINOTOPIC FRAMES OF REFERENCE: EFFECT OF INDUCING ELEMENT SIZE AND INTERACTIONS BETWEEN MULTIPLE FRAMES OF REFERENCE

Babak Noory*[1], Michael H. Herzog[3], and Haluk Ogmen[1,2]
1. Department of Electrical and Computer Engineering, University of Houston
2. Center for Neuro-Engineering and Cognitive Science, University of Houston
3. Brain Mind Institute, Ecole Polytechnique Fédérale de Lausanne (EPFL)

Abstract
A variation of the Ternus-Pikler (TP) paradigm [1] was used to study how non-retinotopic frames of reference (FoRs) depend on the spatial size of their inducing elements, and how multiple FoRs interact with one another. Our results show that the strength of non-retinotopic effect is independent of the size of inducing elements. Furthermore, while dynamic FoRs interact with each other significantly, static FoRs were found to have no effect on a dynamic one.

Introduction

Retinal image motion in the presence of visible persistence should result in a blurry and smeared view of the world. Yet we perceive the world and its moving objects clearly. Recent studies indicate that many visual attributes of a stimulus, such as motion itself, are computed according to non-retinotopic motion-based FoRs [2]. This study tests the dependence of non-retinotopic FoRs on the spatial size of inducing elements, and how multiple FoRs interact.

We modified the Boi et al.'s stimulus [2] to that of Figure 1. This stimulus includes four display frames, each consisting of three disks and three dots. Successive frames of stimulus display are separated by a blank frame for a fixed Inter Stimulus Interval (ISI). Depending upon the value of ISI, two different types of motion are perceived. *Group Motion (Fig. 1-A):* For long ISIs (> 200ms) observers perceive the disks to be moving as a group and the dot to be rotating. *Element Motion (Fig. 1-B):* for short ISIs (i.e. = 0 ms) observers perceive the leftmost disk in the first/third frame to be moving to the position of the rightmost disk in the second/fourth frame and vice versa. In this case, no motion is perceived for the other two disks, and the dots are perceived as moving up-down and left-right.

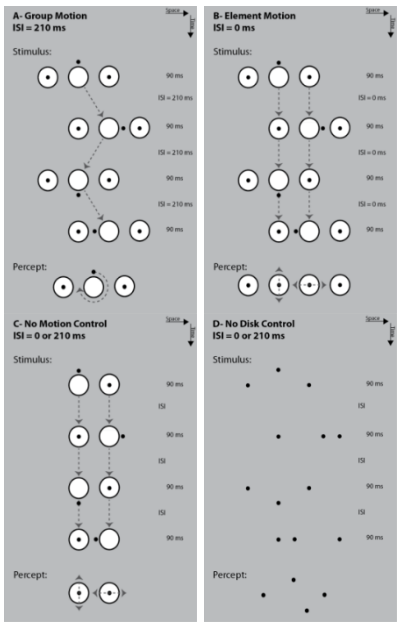

Fig. 1. Stimuli used in Experiment 1

Experimental Procedures

In Experiment 1, to test how the spatial size of the inducing elements (disks) influences the FoR, we placed the dot at a fixed distance and varied the disk size. In a 2-AFC design, observers reported dot rotation direction

(clockwise or counter-). Two control conditions were also included: i) in the "no-reference" control (Fig 1-D) dots were displayed in the absence of disks; ii) in the "no-motion" control, the outer elements in each frame were omitted (Fig 1-C). In Experiment 2, to study multiple FoR interactions, a set of four static or three dynamic squares were introduced above the disks. Dynamic squares moved opposite to the motion of the disks.

Results

The results for Experiment 1 (disk size) and Experiment 2 (multiple FoRs) are plotted in Fig. 2(A) and (B) respectively. Two-way repeated-measures ANOVA shows that experimental condition ($F_{3,32}$ = 51.1; $p < 0.001$), but not disk diameter ($F_{3,32}$ = 0.7; p=0.562), has a significant effect on performance. In Experiment 2, two-way repeated-measures ANOVA shows that experimental condition has a significant effect on performance ($F_{3,64}$ = 53.6; $p < 0.001$). One-way ANOVA shows that distance between the neighboring squares and the disks has a significant effect on performance in the dynamic neighbor experiment condition ($F_{3,16}$ = 17.3; $p < 0.001$), but not in the static neighbor condition ($F_{3,16}$ = 0.1; p = 0.957). In summary, neither variations in the inducing elements' size, nor presence of static neighboring references have a significant effect on the non-retinotopic FoR. A neighboring dynamic FoR, on the other hand, significantly interferes with the effects of the original non-retinotopic FoR.

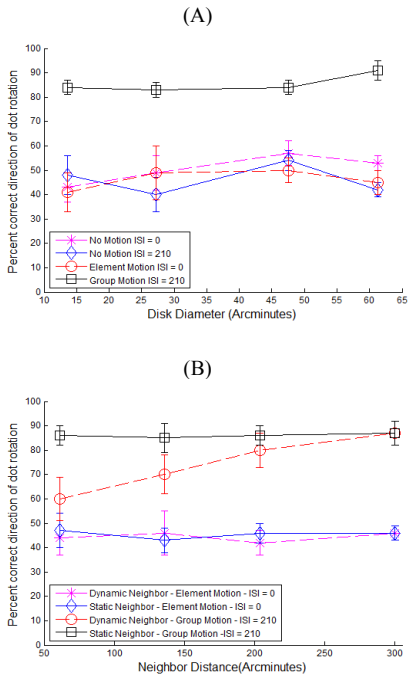

Fig. 2. Percent correct performance in detecting dot rotation direction, averaged across observers and plotted against (A) the disk diameter and (B) neighboring FoR (square objects) distance. Error bars correspond to ±1 SEM.

Discussion

Independence of FoR effect from inducing element size and interactions with dynamic, but not static, neighboring FoRs supports "motion segmentation" based frames of reference hypothesis. Both results argue against purely "object" based FoR hypothesis.

References

[1] J. Ternus, "Experimentelle Untersuchungen uber phanomenale Identitat," *Psychol. Forsch*., vol 7. pp. 81-136 (1926) Translated to English in W. D. Ellis (Ed.), "A Sourcebook of Gestalt Psychology," New York: Humanities Press (1950)

[2] M. Boi, H. Öğmen, J. Krummenacher, T. U. Otto, M. H.Herzog, "A fascinating litmus test for human retino- vs non-retinotopic processing," *Journal of Vision*, vol 9, (13):5, pp. 1–11, 2009.

NON-RETINOTOPIC FEATURE PROCESSING IN THE ABSENCE OF RETINOTOPIC SPATIAL LAYOUT

Mehmet N. Agaoglu[*1], Michael Herzog[2] and Haluk Ogmen[1,3]
[1]Department of Electrical and Computer Engineering,
University of Houston, Houston, TX, USA
[2]Laboratory of Psychophysics, Brain Mind Institute,
Ecole Polytechnique Fédérale de Lausanne (EPFL), Switzerland
[3]Center for Neuro-Engineering and Cognitive Science,
University of Houston, Houston TX USA

Abstract

It has been shown that non-retinotopic mechanisms are involved in dynamic perception of form of objects under normal viewing conditions when there is no occlusion. In this study, we investigated how features are processed in the absence of a retinotopic spatial layout of the stimulus. We brought together anorthoscopic perception [1] and the type of stimuli used in Ternus-Pikler paradigm [2] to probe whether attribution of features follows perceptual organizations or retinotopic layout. Our results show that feature attribution follows perceptual organizations. This finding demonstrates the ability of visual system to operate in non-retinotopic coordinates at fine feature processing level.

Introduction

The optics of the eye maps three-dimensional environment into two-dimensional images such that neighboring points in a visual scene project to neighboring points on the retina. This topography is preserved in early visual areas. It has been shown that this retinotopic representation is neither sufficient nor necessary for perception. Thus the fundamental question is to determine non-retinotopic bases of information processing. Using a Ternus-Pikler display, it was shown that features of a moving object can be perceived at locations where these features are not present [3]. However this method does not rule out the contribution of retinotopic processing. In contrast, anorthoscopic viewing constrains the retinotopic layout inside a narrow slit and introduces retinotopic conflict in that different parts of an object fall on the same retinotopic location as it moves behind the slit. Here by using a novel combination of these two paradigms, we investigated how features are attributed in the absence of retinotopic spatial layout.

Methods

We used a variant of the stimuli used in Ternus-Pikler paradigm (Fig. 1). The experiments consisted of "Connected Lines", "Basic Display", and the "Flash" conditions. In each trial, an offset was inserted randomly to one of the three elements in the display (probe Vernier). In the "Flash" condition, each element was flashed through a narrow slit (7.1^o x 17') whereas in the other conditions, the three-element display was moved behind the slit. Direction of motion was randomized across trials and in all conditions the smallest element always appeared first. Subjects were asked to attend a predetermined element in a given block and report the perceived direction of the vernier offset (left or right w.r.t. upper half).

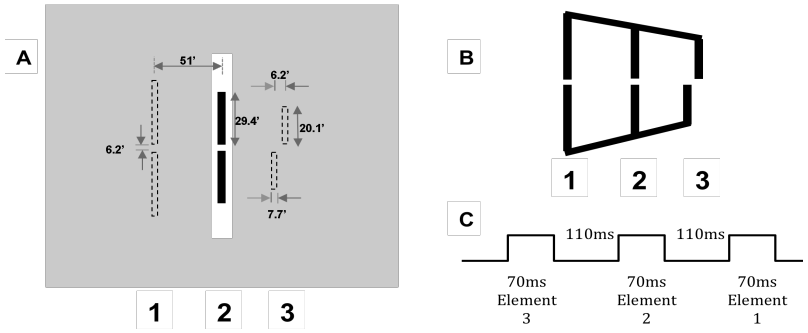

Fig. 1. Stimulus configurations presented behind the slit. (A) "Basic Display" and (B) "Connected Lines" conditions. (C) Time course of the "Flash" condition.

Results and Discussion

Fig. 2 shows the performance for "Connecting Lines" condition averaged over four observers. A RM-ANOVA showed that the physical location of the probe Vernier and the location of the attended line have no significant main effects ($F_{2,6}$=0.335, p=0.660 and $F_{2,6}$=0.261, p=0.683, respectively). However there is a significant interaction between the physical location of the probe Vernier and the location of the attended line ($F_{4,12}$ = 92.773, p<0.0001). Pre-planned t-tests (Table I) show that vernier offsets are attributed to the locations predicted by non-retinotopic processing hypothesis.

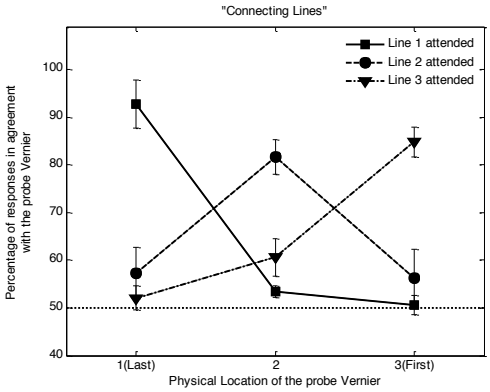

Fig. 2. Percentage of responses in agreement with the probe Vernier. Error bars represent ±SEM

Table I. Each point in Fig. 2 is tested for a significant difference from chance level. PL stands for physical location of probe Vernier

	Line 1 attended		*Line 2 attended*		*Line 3 attended*	
	p-value	t(3)	p-value	t(3)	p-value	t(3)
PL 1	0.004	8.399	0.268	1.357	0.460	0.845
PL 2	0.073	2.717	0.003	8.533	0.072	2.735
PL 3	0.781	0.305	0.376	1.036	0.001	11.479

Conclusion

The visual system can preserve perceptual, in contrast to retinotopic, organizations (e.g. grouping relations due to non-retinotopic factors such as motion) even when retinotopic representations are minimized.

References

[1] Zöllner, F. "Über eine neue Art anorthoscopischer Zerrbilder". *Annalen der Physik und Chemie: Poggendorffs Annalen*, vol. 117, pp. 477-484, 1862.

[2] J. Ternus, "Experimentelle Untersuchungen uber phanomenale Identitat," *Psychol. Forsch*., vol 7. pp. 81-136, 1926, Translated to English in W. D. Ellis (Ed.), "A Sourcebook of Gestalt Psychology," New York: Humanities Press, 1950.

[3] Ogmen, H., Otto, T. U., & Herzog, M. H. "Perceptual grouping induces non-retinotopic feature attribution in human vision", *Vision Research*, vol. 46, pp. 3234-3242, 2006.

IN-SITU STRESS MEASUREMENT DURING THIN FILM GROWTH

N. Dole* [1], D. Lee[2], P. Johnson[2], A. Papou[2], N. Brockie[2] and S.R.Brankovic[1]
Electrochemical Nanofabrication and Nanomaterials Synthesis Group,
[1]Department of Electrical and Computer Engineering,
University of Houston, TX 77204-4005.
[2]Texas Instruments Incorporation,
Santa Clara, CA 95052-8090.

Abstract

In the semiconductor and magnetic industry, thin films are preferred in device fabrication. The stress developed in these thin films during deposition carries great importance as it is an undesired phenomenon and causes change in several mechanical and electrical properties of the film [1]. Our research work mainly focuses on in-situ measurement of stress during film growth by electrodeposition. In this talk, we have made an effort to explain the reasons for stress during film growth with the help of in-situ stress measurements during deposition of magnetic alloys.

Introduction

Stress in thin films can be broadly categorized as intrinsic and extrinsic stress. Intrinsic stress is mainly due to the manner in which film growth takes place on the substrate as well as the epitaxial mismatch between the substrate and the film, coalescence of nuclei, grain growth, and incorporation of impurities during electrodeposition or phase transformations in the deposited film [1]. There are three modes of grain growth, namely Frank van der Merwe mode, Volmer Weber mode and the Strasnki Krastanov mode. Most of the polycrystalline and epitaxial films form by Volmer- Weber mode of growth [1].

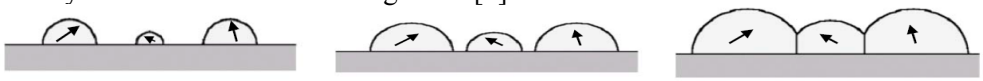

(a) (b) (c)

Figure 1: stages during Volmer Weber growth of polycrystalline films. (a) Nucleation on the substrate surface in the form of island (b) Islands grow as deposition progresses (c) Islands coalescence to form a continuous film.

Results and Discussions

The stress during film growth can be explained in three stages: precoalescence, coalescence and post coalescence as shown in Figure 2(a). When the film begins to grow, crystals with different orientations nucleate with higher surface to volume ratios exerting compressive stress on the substrate [2, 3]. As the film thickness increases, the crystals coalesce together to form continuous film, which contributes to the tensile stress [3]. After a critical thickness is reached, the stress in the post coalescence regime goes compressive due to the incorporation of excessive material in the lattice or grain boundaries. In our experiment set-up, the stress in the film is measured in terms of change in radius of curvature of the film. Using Stoney's equation, the stress can be calculated as,

$$\sigma = \frac{F/w}{t_f} = \frac{E_s * t_s^2}{(1-v_s) * 6 * r * t_f} [\frac{N}{m^2}]$$

where, E_s = Young's modulus, t_s = substrate thickness, v_s = Poisson's ratio, r = radius of curvature, t_f = film thickness. Figure 2(b) shows the in-situ stress measurements during deposition of Permalloy.

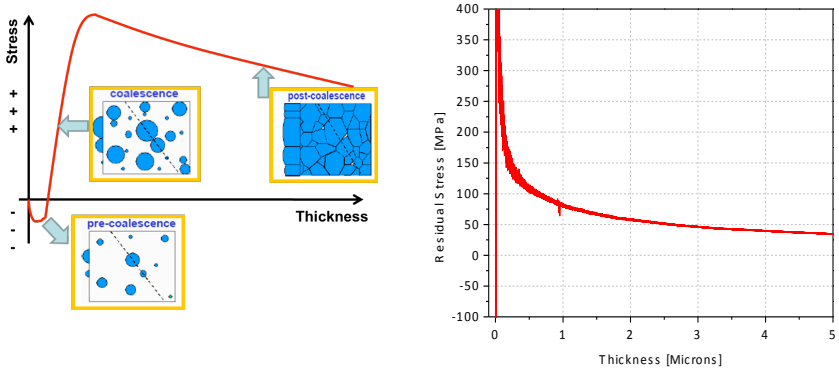

(a) (b)

Figure 2: (a) Explains the dependence of stress on the film thickness. (b) In-situ stress measured during electrodeposition of Permalloy.

Conclusion

We observed that the experimental results followed the theory and were used to explain and understand the stress during thin film growth. It was verified by stress measurement during deposition Permalloy and CoFe magnetic alloys. Thus, we have designed a state-of art system to measure the in-situ stress measurement during thin film growth by electrodeposition.

References

[1] C.V. Thompson and R. Carel, "Stress and grain growth in thin films," *J. of the Mechanics and Physics of Solids,* vol. 44, issue 5, pp. 657-673, May 1996.
[2] C.V. Thompson, "On the grain size and coalescence stress resulting from nucleation and growth processes during formation of polycrystalline thin films," *J. of the Materials Research,* vol. 14, issue 7, May 1996.
[3] R. Koch, D. Hu, and A. K. Das," Compressive Stress in Polycrystalline Volmer-Weber Films", *Phys. Rev. Lett.* , vol. 94, issue 14, Apr 2005.

UNDERPOTENTIAL DEPOSITION ON SUBMONOLAYER MODIFIED SINGLE CRYSTAL SURFACES

Qiuyi Yuan[*1], Stanko R. Brankovic[1, 2, 3]
[1]Department of Electrical and Computer Engineering
[2]Department of Chemical and Bimolecular Engineering
[3]Department of Chemistry
University of Houston
Houston, TX 77204-4005

Abstract

The deposition process of Pb underpotential deposition (UPD) on Pt modified Au (111) single crystal was studied in detail with STM and cyclic voltammetry (CV) results. Pt is deposited on Au (111) through spontaneous noble metal on noble metal deposition process. STM shows that there are four steps involved in the whole deposition. This provides a future possibility to enhance the catalysis property for the mixed-metal system.

Introduction

Thin film growth of uniform noble metal is of great interest due to its variety of application in electrocatalysts, microelectronics, and optical materials. The energy crisis requires people to develop novel energy resource other than petroleum. Fuel cell is one of the promising substitutions of the traditional energy.

Underpotential deposition (UPD) means the deposition which occurs at a more positive potential than the reversible Nernst potential, E_{rev}, when depositing metal on a foreign metal substate. This phenomenon can result in a submonolayer (SML) or monolayer (ML) growth can be formed during the UPD due to the strong interaction between the depositing metal ions and the metal substrate [1, 2].

To achieve better catalytic activity, we investigate here a novel UPD system of depositing metal Pb on a single crystal metal substrate Au (111) decorated by another noble metal such as Pt. Pt is deposited on Au (111) using spontaneous deposition. Then the Pt modified Au (111) is used as the substrate to study Pb UPD. The UPD process is studied in-situ by electrochemical STM.

Result and Discussion

The potential is swept from 750 mV to 100mV vs. Pb^{2+}/Pb pseudo reference electrode. Figure1 shows the cyclic voltammetry (CV) and STM result taken at different potentials.

At 770 mV only Pt decorated Au (111) can be observed (Fig.1A). As the potential gradually swept negative, the UPD of Pb is formed between Pt clusters. In Fig.1(B), at 200 mV vs. Pb^{2+}/Pb pseudo reference electrode, the partial Pb UPD is formed and at 100 mV, a full ML Pb is formed.

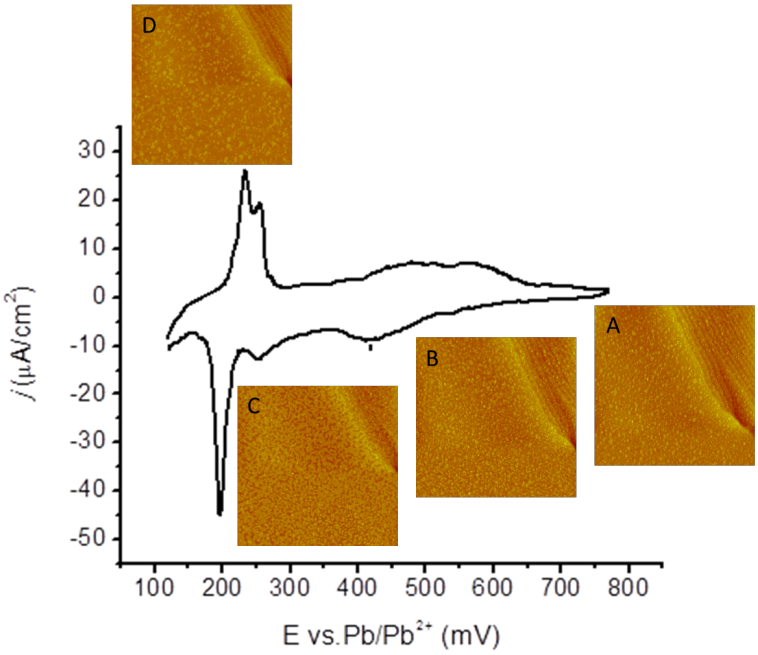

Fig. 1 STM and CV results: (A) Spontaneous deposition of Pt on Au(111) surface. (B) Applied Potential at 400mV vs. Pb2+/Pb pseudo reference electrode. (C) Applied Potential at 250mV. (D) Applied Potential at 100mV (full ML). Image size: 225 ×225 nm.

Conclusion

A new UPD system, Pb UPD on Pt modified Au (111) is proposed. By studying with CV and STM, and the help of image processing software, we can see that the UPD process consists of four steps. At first, deposition starts on Au terraces. During the second stage, Pb begins to deposit on Au terraces and around the existing clusters. With the growth of Pb, coalescence happens at the point of 200mV, corresponding to the main peak. In the final stage, Pb deposits on top of Pt clusters concurrent with the growth on Au terraces.

References

[1] S. R. Brankovic, *Functional Properties of Bioinspired Surfaces - Characterizations and Technological Applications*, Chapter 11, World Scientific, 2009.
[2] E. Herrero, L. J. Buller, and H. Abruna, "Underpotential Deposition at Single Crystal Surfaces of Au, Pt, Ag and Other Materials," *Chem. Rev.,* vol. 101, pp. 1897-1930, 2001.

GROWTH FROM BELOW: BILAYER GRAPHENE ON COPPER BY CHEMICAL VAPOR DEPOSITION1

Sirui Xing*, Wei Wu, and Shin-Shem Pei
Department of Electrical and Computer Engineering
Center for Advanced Materials
University of Houston
Houston, TX 77204

Abstract

The layer stacking of bilayer graphene grains synthesized by chemical vapor deposition (CVD) on Cu foil has been analyzed. Low-energy electron diffraction and microscopy indicate that smaller layer lies between Cu substrate and larger layer, which is contrary to the widely assumed wedding cake structure. These observations uphold a mechanism where the new layer nucleates and grows under the first layer. The underlayer mechanism assists achieving single uniform layers but presents challenges for growing bilayer films by CVD.

Introduction

Graphene growth by chemical vapor deposition (CVD) on metals has emerged as a promising technology for producing large-area films. Single-layer films have been successfully deposited over large areas on Ni[1] and Cu substrates.[2] The CVD growth of bilayer graphene (BLG) at wafer scale has also been demonstrated.[3] The energy dispersion of the electronic bands in AB-stacked BLG is quadratic, and a tunable bandgap is created by applying an electrical field perpendicular to the film.[4] Realizing a bandgap opens the door of digital electronics. The challenge is to develop a BLG technology that gives a uniform and reproducible bandgap over large areas. A better understanding of how BLG grows in CVD will aid this development and also improve the growth of single-layer graphene that is free of BLG.

In crystal growth, new layers typically nucleate and grow on top of prior layers. This mechanism has been assumed to occur during CVD growth of BLG and few-layer graphene (FLG) on metals and form wedding cake structure.[5]

In this report, we analyze BLG grains grown by CVD on Cu foils. We find that the smaller graphene layers lie below the larger layers, which offers persuasive evidence that the new layers nucleate and grow next to the Cu. C likely diffuses along the surface of the bare Cu, goes under the first graphene layer, and then diffuses to the edge of the buried layer. The facet and lattice rotation between the buried and overlying layers is the same within measurement error. For hexagonal grains of single-layer graphene grown by CVD on Cu, this termination is predominantly of zigzag type. SEM observations of facet directions can be used to assess the statistics of crystallographic alignment in bilayer stacks. We discuss the implications of underlayer growth for achieving uniform single-layer and BLG.

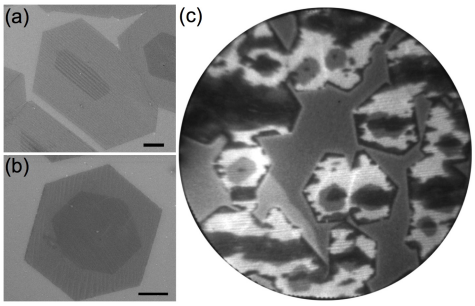

FIG. 1. (a,b) SEM and (c) PEEM images of graphene on Cu. In the SEM images, the medium- grey regions are faceted single-layer sheets. The darker regions, which are also faceted, have two graphene layers. The scale bars are 2 μm. PEEM field of view is 50 μm.

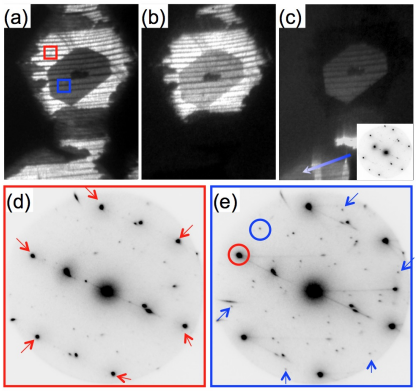

FIG. 2. (a) Bright-field and (b-c) dark-field LEEM images (11.5 x 15 microns). The grey hexagonal region near the center of (a) is BLG whose edges are rotated with respect to the surrounding bright first-layer sheet. (d) Selected-area LEED from the first-layer region marked by the red box in (a). Red arrows mark the single set of 6-fold graphene spots. (e) Diffraction from the BLG region marked by the blue box. The weak graphene spots marked in blue come from the buried layer. Dark-field image (b) is from the top-layer diffraction spot circled in red in (e). Dark-field image (c) is from the buried-layer diffraction spot circled in blue. The insert diffraction pattern in (c) is from the single-layer region marked by the arrow.

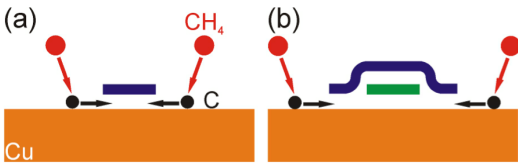

FIG. 3. Underlayer growth mechanism during CVD on Cu. The new graphene layer (green) nucleates below the first layer (blue), giving an inverted wedding cake whose small layers are below larger layers.

Acknowledgement

We thank S. Nie for graphene characterization and Q. Yu, J. Bao, K. F. McCarty for informative discussion.

References

[1] Q. Yu, J. Lian, et al. "Graphene segregated on Ni surfaces and transferred to insulators," *Applied Physics Letters*, vol. 93, no. 11, p. 113103, 2008.
[2] Wei, W., Q. Yu, et al. "Control of thickness uniformity and grain size in graphene films for transparent conductive electrodes," *Nanotechnology*, vol. 23, no. 3, p. 035603, 2012.
[3] S. Lee, K. Lee, and Z. Zhong, "Wafer Scale Homogeneous Bilayer Graphene Films by Chemical Vapor Deposition," *Nano Letters*, vol. 10, p. 4702, 2010.
[4] Y. Zhang, T.-T. Tang, et al. "Direct observation of a widely tunable bandgap in bilayer graphene," *Nature*, vol. 459, p. 820, 2009.
[5] Robertson, A. W. and J. H. Warner. "Hexagonal Single Crystal Domains of Few-Layer Graphene on Copper Foils," *Nano Letters*, vol. 11, no. 3, pp. 1182-1189, 2011.

SUPERIOR RADIATION AND DISLOCATION TOLERANCE OF IMM SPACE SOLAR CELLS

A. Mehrotra*[1], and A. Freundlich[1]
Center for Advanced Materials, Photovoltaics Research Group
[1] Department of Electrical and Computer Engineering
University of Houston
Houston, TX 77204-4005

Abstract

In this work we have evaluated thickness dependent efficiency of Inverted Metamorphic (IMM) solar cells as a function of radiation doses and dislocations and band gap of the bottom metamorphic InGaAs subcell. It is shown that for moderate to high doses of radiation, very high end of life performance (EOL) efficiencies can be afforded with substantially higher dislocation densities than those commonly perceived as acceptable for IMM devices. i.e even in the presence of dislocation densities as large as $2x10^7 cm^{-2}$,for typical $2x10^{15} cm^{-2}$ 1 MeV electron fluence a remaining power factor of >85% (ηEOL~28%) can be reached by a careful selection of InGaAs band gap. Finally these finding could in turn be used to simplify manufacturing (thinner graded buffers) or/and increase yield for IMM space cells.

Introduction

Inverted metamorphic multijunction (Fig. 1) solar cells have demonstrated AM0 efficiencies of ~33% [1]. But the major drawback in IMM solar cells is the presence of defects in InGaAs bottom sub-cell which cause reduction in minority carrier lifetime and result in efficiency degradation. Hence, thick buffer layer are used in order reduce these defects. Space radiation also causes reduction in diffusion length and lifetimes [2]. Hence solar cells in space slowly degrade due to presence of this radiation. It is been shown that thickness optimization of multijunction GaInP/GaAs solar cell would give better end of life performance (EOL) than conventional solar cells [3]. Therefore, in IMM by using thin devices, one would obtain low efficiencies at beginning of life (BOL) but would result in improved efficiency at end of life (EOL) than conventional thick devices.

Discussion

Dislocations present in metamorphic 1ev InGaAs sub-cell would decrease the efficiency of solar cell, hence buffer filtering techniques are commonly used in order to reduce dislocation density in InGaAs solar cell below 10^6 cm^{-2}. In IMM solar cell the current limiting sub-cell is the mid GaAs cell, which hints towards the use to degraded bottom InGaAs cell without having any effect on efficiency. Hence using high dislocation density in InGaAs one can still achieve the same efficiencies till GaAs sub-cell remains current limiting. Using thinner InGaAs cell with high dislocations maintains the VOC while the sub-cell is not too thin to become current limiting. Fig. 1 (b) shows that for dislocation densities of 10^6, 10^7 and $2x10^7$ cm-2 when optimized for $2x10^{15}$ cm^{-2} equivalent electron fluence, the EOL performance is the same for all solar cells since change is dislocation density doesn't lead to change in EOL efficiency. For example, for a radiation dose equivalent to a fluence of 10^{15} cm^{-2} 1 MeV electrons, the optimal design for the highest EOL performance becomes insensitive to the presence of dislocation

densities, which are smaller than 10^7 cm^{-2}.

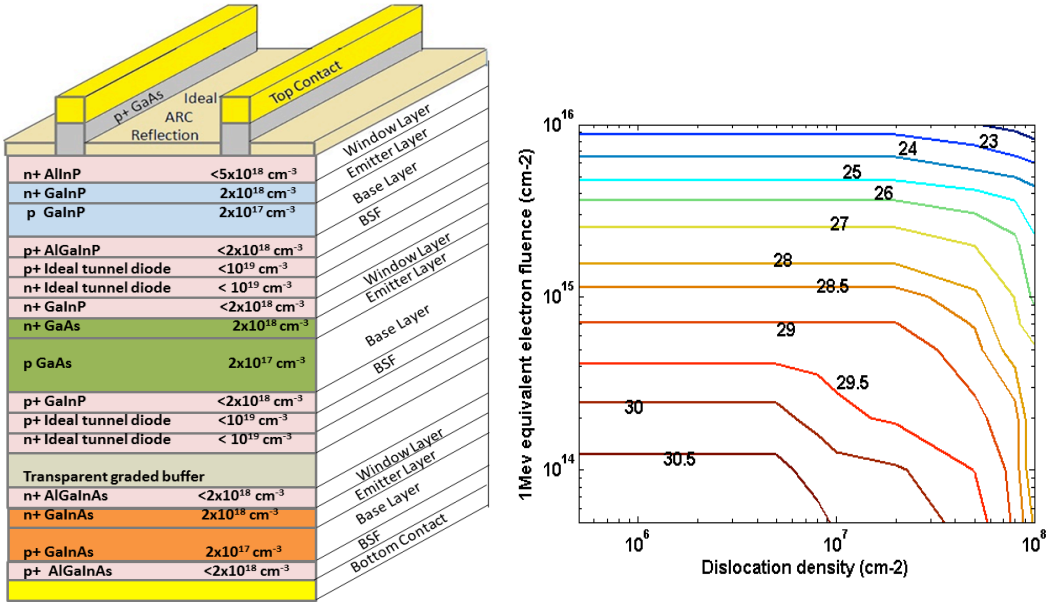

Fig. 1. (a) Structure of n on p GaInP/GaAs/GaInAs IMM solar cell device. (b) Optimized IMM efficiencies as a function of radiation dose and dislocation density, indicating defect tolerance limit for given EOL fluence.

Conclusion

It is shown that by optimizing the base-emitter thickness of IMM sub-cells for end-of-life performance, one can obtain power remaining factor ~0.9 for $10^{15}cm^{-2}$ 1MeV electron fluence. In addition these calculations indicate that for radiation doses in excess of an equivalent $2x10^{15}$ cm^{-2} 1 MeV electron fluence, the optimized design makes IMM insensitive to presence of dislocations ($<2x10^7$ cm^{-2}) in the InGaAs bottom sub-cell. The results suggest that by optimizing the device design, one can obtain nearly the same EOL efficiencies for highly dislocated metamorphic solar cells as those of an ideal defect free IMM. These findings could be of importance to the manufacture of current metamorphic space cells as to some extent they indicate possibilities for circumventing the need for sophisticated defect filtering techniques. Also for higher EOL efficiencies use of metamorphic InGaAs cell with band gap lower than 1.0ev (~0.95ev) has been demonstrated without the loss in device defect tolerant behavior.

References

[1] A.B. Cornfeld, D. Aiken, B. Cho, A.V. Ley, P. Sharps, M. Stan, and T. Varghese, "Development of a four sub-cell inverted metamorphic multi-junction (IMM) highly efficient AM0 solar cell", *Thirtyfifth IEEE PVSC*, pp. 105, 2010.

[2] T. Takamoto, M. Yamaguchi, S. J. Taylor, E. Ikeda, T. Agui, and H. Kurita, "High efficiency radiation resistant InGaP/GaAs tandem solar cell", *26th IEEE PVSC*, pp. 887-890, 1997.

[3] A. Mehrotra, A. Freundlich, and A. Alemu, "Optimized device design for radiation resistant and high dislocation solar cells for space", *Thirtyfifth IEEE PVSC*, pp. 2574-2577, 2010.

THIS PAGE IS INTENTIONALLY BLANK

ABSTRACTS FOR POSTER PRESENTATIONS

GENETIC ALGORITHMS AND LINEAR DISCRIMINANT ANALYSIS BASED DIMENSIONALITY REDUCTION FOR REMOTELY SENSED IMAGE ANALYSIS

Minshan Cui*[1], Saurabh Prasad[1], Majid Mahroogy[2], Lori M. Bruce[2], and James Aanstoos[2]
NCALM Research Group
[1] Department of Electrical and Computer Engineering
University of Houston
Houston, TX 77204-4005
[2] Department of Electrical and Computer Engineering
Mississippi State University
Mississippi State, MS 39762

Abstract

Remotely sensed data (such as hyperspectral imagery) is typically associated with a large number of features, which makes classification challenging. Feature subset selection is an effective approach to alleviate the curse of dimensionality when the number of features contained in datasets is huge. Considering the merits of genetic algorithms (GA) in solving combinatorial problems, GA is becoming an increasingly popular tool for feature subset selection. In this paper, we will present a new approach called Genetic Algorithm based Linear Discriminant Analysis (GA-LDA) to extract features in which feature selection and feature extraction are performed simultaneously to alleviate over-dimensionality and result in a useful and robust feature space.

Introduction

Hyperspectral Imagery (HSI) capture reflected radiation over a series of contiguous bands covering a wide range of the electromagnetic spectrum for every pixel in the image. However, analysis methods for such imagery first must reduce the dimensionality of this very high dimensional feature space to make any classification analysis tractable. However, identifying and selecting relevant features from a large set of features is not a trivial task. Genetic algorithms (GA) have become popular tools for various feature subset selection problems [1]. However, the most popular GA based feature selection strategy uses the training classification accuracy to optimize and find the "best" feature subset. This greedy search is only suitable for classification tasks that do not operate in high dimensional feature spaces. As the feature-space dimensionality increases, the amount of time required for such a search increases significantly.

In this work, we study two different metrics as potential filter functions for a GA based feature selection of high dimensional remotely sensed data: (1) Bhattacharyya distance (BD) [2], and (2) Fisher's ratio [3].

Proposed System

In this study, we propose an algorithm called Genetic Algorithm based Linear Discriminant Analysis (GA-LDA). In this proposed method, we first do GA based feature selection using BD or Fisher's ratio as a fitness function. After GA based feature selection, we apply an LDA projection to further project the subset of features on a reduced dimensional subspace optimized for classification. This algorithm is particularly

useful when LDA cannot be directly applied on the input feature space owing to its very high dimensionality.

Experimental Result

Figure 1 shows the classification accuracy versus number of training samples for the Indian Pines and corn crop dataset. From this figure, it is clear that the proposed GA-LDA based feature extraction technique outperforms the other two "baseline" approaches to classification including Stepwise LDA (SLDA) and LDA, especially when the number of available training samples is small.

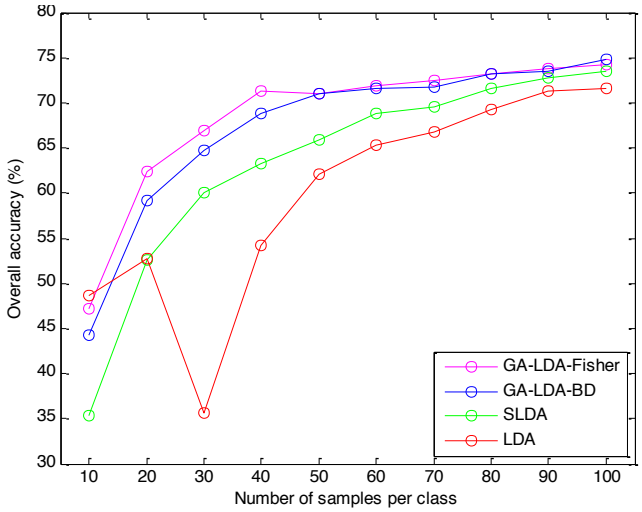

Fig. 1. Illustrating the benefits of the proposed GA-LDA feature reduction approach for the Indian pines dataset. GA-LDA-Fisher: Using fisher's ratio as the fitness function in GA-LDA; GA-LDA-BD: Using BD as the fitness function in the GA-LDA.

Conclusion

Experimental results presented in this paper indicate that a GA search is very effective at selecting the most pertinent features, while pruning out the most redundant features for classification tasks when an appropriate fitness function is employed. Akin to the conventional stepwise-LDA approach, we proposed a GA-LDA approach where GA first identifies a smaller subset of features upon which LDA is applied for final dimensionality reduction.

References

[1] H. Kim, C. Park, H. Yang and K. Sim, "Genetic Algorithm Based Feature Selection Method Development for Pattern Recognition," *SICE-ICASE*, 2006.
[2] C. Lee and D. Hong, "Feature Extraction Using the Bhattacharyya Distance," *IEEE International Conference on Systems, Man, and Cybernetics*, 1997
[3] T. Dat and C. Guan, "Feature selection based on fisher ratio and mutual information analysis for robust brain computer interface," *IEEE International Conference on Acoustics, Speech and Signal Processing*, 2007.

AUTOMATIC SEGMENTATION OF BURULI IMAGES

Rui Hu*[1], Tarun Wadhawan[2], and George Zouridakis[1,2,3]
Biomedical Imaging Lab
[1] Department of Electrical and Computer Engineering
[2] Department of Computer Science
[3] Department of Engineering Technology
University of Houston
Houston, TX 77204-4005

Abstract

Buruli ulcer, a disease caused by infection with Mycobacterium ulcerans, is one of the most neglected but treatable tropical disease. In this paper, a color-based segmentation scheme is proposed to detect the border of skin lesions in Buruli images. Firstly, segmentations from different color spaces by thresholding are fused to form an initial contour; subsequently, a level set approach is applied on both illumination and color channels; finally, decisions for each pixel are made by a SVM classifier. Experimental results on 26 images show that the proposed method outperforms other state-of-art segmentation approaches for Buruli images.

Introduction

Buruli ulcer, a skin disease caused by the infection with Mycobacterium ulcerans, is the third most common mycobacterial disease after tuberculosis and leprosy and mainly affects remote rural African communities [1]. However, if patients seek treatment at the early stage, antibiotics can prove to be successful to prevent the irreversible deformity and long-term functional disability. So detecting Buruli disease in the early stage is of particular importance.

Automatic segmentation is often the first and important step in the computerized analysis of skin lesion images, since it affects the accuracy of the subsequent steps. Numerous methods have been developed for border detection in dermoscopy images. For instance, adaptive thresholding [2] automatically choose the color component with the highest entropy and set up a threshold based on the histogram. Erkol et al. [3] proposed a method based on the Gradient Vector Flow (GVF) snakes with an automatic initialization. Silveira et al. [4] applied the Level Set method which has been successfully used in many medical imaging problems with the requirement of user interaction of two mouse clicks. In this paper, we present a novel color-based segmentation scheme to detect lesion borders in Buruli images.

Methods

The proposed method consists of three steps: contour initialization, contour evolution, and pixel classification. At the first step, a global thresholding method is applied to color components of La*b*, HSV, YCbCr, and Lu*v* color spaces respectively, following a voting system to fuse the preliminary segmentations into an initial contour. Subsequently, we applied level set approaches to the color channel in which segmentation result is most correlated to initial contour and the gray scale image to obtain two masks. Finally, pixels belonging the common foreground and background of these two masks are considered as lesion and normal skin respectively. For the remaining pixels, decisions are made by a

SVM classifier based on pixel values of RGB and Lu*v* color space. Fig. 1 illustrates an example of the proposed scheme.

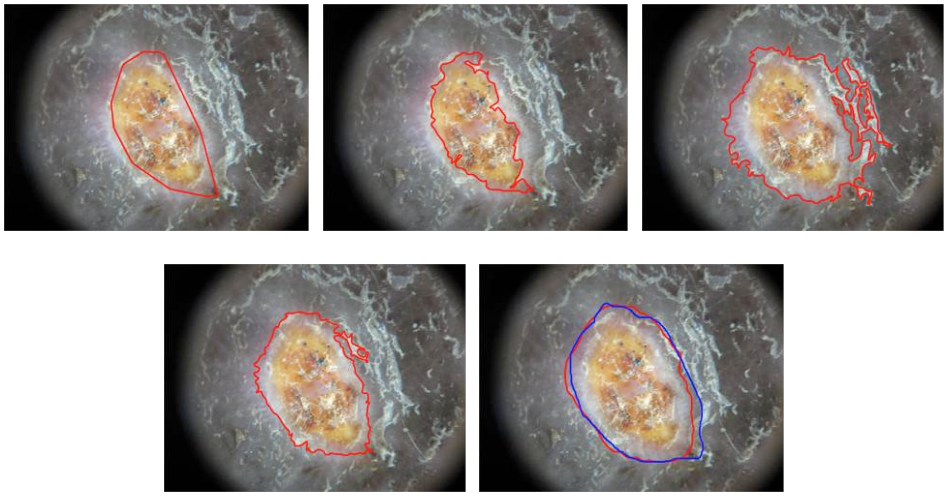

Fig. 1. Example of color-based segmentation scheme. From top to bottom and left to right,: a) initial contour; b) contour evolution in color component; c) contour evolution in illumination component; d) decision after pixel classification; e) Segmentation after post-processing (red) and manual segmentation from a dermatologist (blue).

Results

The proposed method is tested on a dataset of 26 dermoscopy images of Buruli disease. Using baseline manually segmented skin lesions from a dermatologist, the segmented lesions from four different methods are compared based on XOR error, as Tab. 1. shows.

Table1. Classification performance using different sampling strategies

Methods	Thresholding	GVF Snake	Level-set	Color-based
Accuracy(%) std	59.51±27.81	75.09±12.02	73.46±19.78	81.03±8.72

References

[1] M. Boleira, O. Lupi, L. Asiedu, et al, "Buruli Ulcer," *An Bras Dermatol*. vol. 85, no. 3, pp. 281-298, Jun. 2010.

[2] M. Carlotto, "Histogram analysis using a scale-space approach," *IEEE trans. on PAMI*, iss. 1, vol., no. 9, pp. 121-129, Jan. 1987.

[3] B. Erkol, R. Moss, R. Stanley, et al, "Automatic lesion boundary detection in dermoscopy images using gradient vector flow snakes," *Skin Res Technol*. vol., 11, pp. 17-26, 2005.

[4] T. Chan, B. Sandberg, and L. Vese, "Active contours without edges for vector-valued images," *J. Vis. Commun. Image Repres*., vol. 11, no. 2, pp. 130–141, 2000.

Acknowledgements

This work was supported in part by NIH grant no. 1R21AR057921 and the Texas Learning and Computation Center at the University of Houston.

PARALLEL RAMAN MICROSPECTROSCOPY USING PROGRAMMABLE MULTI-POINT ILLUMINATION

Ji Qi* and Wei-Chuan Shih
NanoBioPhotonics Group
Department of Electrical and Computer Engineering
University of Houston
Houston, TX 77204-4005

Abstract

We present a novel parallel Raman microspectroscopy scheme for simultaneously collecting Raman spectra from multiple points. This scheme is realized by projecting a multiple-point laser illumination pattern using a spatial light modulator (SLM) and wide-field Raman imaging collection. We demonstrate the performance of this scheme using uniform samples, trapped polymer microparticles and fixed polymer microparticles with mixed molecular composition within a ~ 80 x 80 μm^2 field of view. This scheme enables the acquisition of Raman spectra from as many as 60 points simultaneously using a single illumination pattern and detector recording frame without scanning.

Introduction

Raman spectroscopy can provide molecular information via inelastic light scattering without physical contact. Coupled with microscopic imaging, Raman microspectroscopy is a powerful technique for material analysis, for example, stress and temperature measurement in silicon and compositional analysis of polymer microparticles [1]. Three methodologies are commonly employed in contemporary Raman microspectroscopy, namely, point-scan, line-scan and global illumination [1]. The point-scan operation involves the collection of Raman spectra in a point-by-point fashion. Since Raman scattering is a relatively weak phenomenon, the laser spot dwelling time at each point is typically on the order of milliseconds to seconds. Typically, conventional point-scan Raman mapping is a time-consuming process and can take as long as a few hours to map a 80 x 80 μm^2 region.

To improve efficiency, parallel acquisition has been implemented based on time-sharing or power-sharing schemes. In the former one, the laser is rapidly scanned over multiple points of interest during the time of a single CCD recording frame [2, 3]. In the latter one, the laser is shaped into an elongated line and the entire line is imaged by a single CCD frame [1, 4, 5]. A key difference, however, lies in the temporal power fluctuation within a CCD frame: for time-sharing, the total laser power is focused on one spot at any given time but for power-sharing the laser power is distributed on all spots. Another significant difference is that there is no scanning within each frame for power-sharing. Recently, the time-sharing approach has been demonstrated to provide flexibility for imaging multiple points not aligned on a line, which is particularly advantageous for sparse samples such as bacteria or environmental particles [2].

In this paper, we present a novel power-sharing approach that allows the simultaneous imaging of multiple points not aligned on a line. This is achieved by combining programmable multi-point laser illumination with wide-field Raman imaging.

Methods

785 nm output of a CW Titanium: sapphire laser (Spectra-Physics 3900S) is expanded to ~ 1 cm in diameter before the spatial light modulator (LCOS Hamamatsu). The output from the SLM is fed into an inverted microscope (Olympus IX71). A dichroic mirror (Semrock LPD01-785RU-25) is placed in the microscope turret for epi-Raman acquisition via a microscope objective (Olympus UPLSAPO 60XW, 1.2 NA). The Raman light is filtered by a long pass filter (Semrock LP02-785RS-25) and sent into a spectrograph (Acton 2300i) with a TE cooled CCD camera (Princeton 400BR-excelon).

Results

The spatial (x-y-z) resolution of proposed Raman microspectroscopy system is ~ 0.9, 0.9 and 4.5 μm, respectively by scanning across 0.5 μm polystyrene beads. The spectral resolution of our system is ~ 8 cm^{-1}. We have analyzed mixed populations of polystyrene and PMMA microparticles. Since tightly focused laser spots can readily form optical traps, the proposed scheme can trap multiple microparticles in arbitrary spatial (x-y) plane within 80 x 80 μm^2 and up to 10 μm in axial (z) direction.

Conclusion

In conclusion, we have demonstrated a novel scheme for parallel Raman microspectroscopy by combining programmable multi-point illumination and wide-field Raman imaging. This scheme provides flexibility to simultaneously image multiple points not aligned along a line in contrast to traditional power-sharing scheme using a line-shape illumination while retaining other features such as non-scanning, 100% duty cycle and constant power distribution on all spots within one CCD frame. This novel scheme may be applicable for ultra-high throughput Raman microspectroscopy and imaging, particularly when the sample is sparse or has unevenly distributed information density. In addition, this scheme can be effectively combined with optical traps with 100% duty cycle for facile multiplexed trapping and simultaneous Raman microspectroscopy.

References

[1] S. Schlucker, M. D. Schaeberle, S. W. Huffman, and I. W. Levin, "Raman microspectroscopy: A comparison of point, line, and wide-field imaging methodologies," *Anal Chem*, vol.75, pp. 4312-4318, 2003.
[2] L. Kong, Z. P, P. Setlow, and Y. Li, "Multifocus confocal Raman microspectroscopy for rapid single-particle analysis," *J Biomed Opt*, vol. 16, 120503, 2011.
[3] R. Liu, D. S. Taylor, D. L. Matthews, and J. W. Chan, "Parallel Analysis of Individual Biological Cells Using Multifocal Laser Tweezers Raman Spectroscopy," *Appl Spectrosc,* vol. 64, 1308-1310, 2010.
[4] J. Qi, P. Motwani, J. Wolfe, and W.-C. Shih, "High-throughput Raman and Surface-enhanced Raman Microscopy," in *SPIE Photonics West*, (SPIE, San Francisco), 2012.
[5] K. A. Christensen and M. D. Morris, "Hyperspectral Raman microscopic imaging using Powell lens line illumination," *Appl Spectrosc*, vol. 52, pp. 1145-1147, 1998.
[6] V. Nikolenko, B. O. Watson, R. Araya, A. Woodruff, D. S. Peterka, and R. Yuste, "SLM microscopy: scanless two-photon imaging and photostimulation with spatial light modulators," *Frontiers in Neural Circuits* 2, 14, 2008.

ON-DEMAND TRACING OF MICROGLIA PROCESSES

H. T. Cheung* and B. Roysam
Bio-Imaging Analytics Research Group
Department of Electrical and Computer Engineering
University of Houston
Houston, TX 77204-4005

Abstract

Tracing microglia accurately is an important step of learning how microglia respond to neural probes. The problem with current state-of-the-art approach to tracing is that they trace all microglia simultaneously in a tree-building step. This forces a constraint that all the centroids of the microglia be known ahead of time before tracing is done and that we must keep information about all microglia in memory and cannot parallelize this process. We propose to use a new method of only selecting the region in which a microglia lies and tracing it, without knowledge of the other microglia around it. This process will thus be memory-efficient, parallelizable, and on-demand.

Introduction

Modern confocal-fluorescent microscopy allows for imaging very large spaces by taking multiple overlapping 3D tiles of the tissue to be studied. These tiles are then put through a registration process [1] and mosaicing is performed to produce a very large montage. This large montage itself is already problematic to fit into the main memory of contemporary personal computers. The state-of-the-art tracer based on the unpublished work on Amit Mukherjee currently does critical point detection, which require at least 10 times the size of the input image as temporary working space. Furthermore, the tree-building process, which is a modified Prim's Algorithm [2], forces the tree-building process to be run sequentially. This combination of memory-inefficiency and sequential processing means that this tracing process will not scale in memory-efficiency or speed with the size of the image. The Microglia Region Tracer allows for lesser memory-consumption by only keeping and is fully parallelizable, needing no communication between different threads of tracing.

Tracing is done in 4 main steps: First, registration is performed on the tiles of the image. This registration process produces a "joint transform" file. The montage is not generated here (so we do not have to keep a copy of the entire image in memory) and instead a small region-of-interest is extracted and passed onto the next step. Secondly, we take the region of interest (ROI) image and extract "critical points". Third, the Frangi's vesselness measure is applied [3]. This enhances the tube-like structures in the image. Lastly, the tree-building step is performed. The tree-building builds a minimum-spanning tree using Prim's Algorithm [2].

Currently, the input images are 20 GB and takes 3-4 hours to process with 512 GB of RAM. This is not a terrific situation in the face of whole rat-brain images, which are projected to be a terabyte or more. This tracer hopes to reduce this to a more manageable size that can be run on the more modest machines in the lab with 8 GB. An additional benefit of this tracing method is that the speed will scale inversely proportional with the amount of processors in the system. The MicrogliaRegionTracer has invariant memory-consumption relative to the input image size and the execution time scales linearly with

the size of the image and inversely proportional to the number of processors available.

References

[1] G. Yang, C. V. Stewart, M. Sofka, and C. Tsai, "Registration of challenging image pairs: initialization, estimation, and decision", *IEEE Transactions on Pattern Analysis and Machine Intelligence,* vol.29, no.11, pp.1973-1989, Nov. 2007.
[2] R. C. Prim, "Shortest connection networks and some generalizations." *Bell System Technical Journal*, vol. 36, pp. 1389-1401, 1957.
[3] A. F. Frangi, W. J. Niessen, K. L. Vincken, and M. A. Viergever. "Multiscale vessel enhancement filtering" *MICCAI'98 Medical Image Computing and Computer-Assisted Intervention*, pages 130–137, 1998.

FEATURE SELECTION FOR QUANTIFICATION OF GLIAL MORPHOLOGY IN RESPONSE TO NEURAL PROSTHETIC IMPLANTATION

A. Cheong* and B. Roysam
Bio-Image Analytics Laboratory
Department of Electrical and Computer Engineering
University of Houston
Houston, TX 77204-4005

Abstract

Quantitative analysis was performed on three-dimensional images of rat brains that received neural implants. The application of L-Measure, a quantitative measurement tool for neuronal reconstructions, on the images revealed certain limitations in describing the overall cell shape, the cell orientation, and the soma as well as viewing the data at multiple scales. Additional metrics were developed and some methods of L-Measure were reworked to enhance the quantitative study of neurites within a program called the FARSIGHT 3D Trace Editor.

Introduction

Microglia are the main form of immune defense within the brain. Their role in the protection and maintenance of the brain makes them a target of study of neurological diseases. Microglia can be classified into three states: ramified, amoeboid, and activated. In each state, microglia takes on a particular structure. In the case of studying the effects of neural implantation, the brain slice reveals a majority of amoeboid-like microglia gathering at the implant site after one week and a majority of activated (highly-branched) microglia after six weeks. A healthy and unaffected brain shows microglia in a ramified (resting) state. The quantitative feature analysis allow for the objective comparison of microglia in their various states as well as the study of the cell variations within a state.

L-Measure computes 43 unique metrics and all except for helix and fractal dimension are incorporated in the FARSIGHT 3D Trace Editor [1]. The trace editor is a program used for visualizing neuronal images and performing cluster edits on traces, which are a collection of 3D points and their radii modeling the soma and the processes of each cell in an image [2]. The measurements are obtained from the traces and presented in a table where each row list the computed features of a cell: the soma surface area, the diameter of the processes, the path length of the processes, and so on. Each metric, except the locations and counts such as the number of branches, is summarized as a minimum value, average value, maximum value, and standard deviation. A total of 55 unique metrics are currently computed in the Trace Editor.

Methods

An addition of 11 metrics have been added to describe glial morphology (Table 1).

Table 1. Metrics to describe glial morphlogy.

Metrics	Description
Skewness X,Y,Z	The x, y, and z distance of the soma centroid from the center of the computed bounding box

	of a cell.
Euclidean Skewness	The straight line distance of the soma centroid from the center of the computed bounding box of a cell.
Azimuth (-180º to 180º)	Angle of a segment on the x-y plane.
Elevation (-90º to 90º)	Angle of a segment extending in the z direction from the azimuth.
Branch Pt to Soma Euclidean Distance	Straight line distance from the branch point to the soma point.
Tip to Soma Euclidean Distance	Straight line distance from the terminal tip to the soma point.
Magnitude of Tips	The overall magnitude from the summation of the Tip to Soma Euclidean Distance.
Azimuth of Tips	The azimuth angle of the Magnitude of Tips.
Elevation of Tips	The elevation angle of the Magnitude of Tips.

Discussion

Since L-Measure currently provides quantitative information only at the cell level, the current work is to expand the quantitative analysis across multiple levels to provide information at the segment level and below as well as the information above such as the cell-to-cell level. With each additional level, new features emerge such as the density and nearest neighbor measurements at the cell-to-cell level. The manipulation of data at multiple levels will further enhance the quantitative analysis of neurites. For each level, the applicable features are put into a heat map, or some other graphical representation of data, to obtain a hierarchy of features to reveal correlations between features. While L-Measure computes the same statistics (min, mean, max, and standard deviation) for every metric, not every metric should have these statistics such the counts, which only computes one number for each cell. Since these statistics should not be applied to soma position and the counts, not every feature can be correlated through direct comparison of the min, mean, and max. A method that takes into account feature dependencies upon other features needs to be applied to the data. Other alternative methods, such as the comparison of distributions, are being considered to obtain more accurate feature correlations.

Conclusion

The proposed metrics along with L-Measure are designed to set a quantitative standard for researchers to use for analyzing neurites and compare results. Analyzing data at multiple levels as well as adding new metrics will provide insight to understanding cell morphology. Additional metrics still need to be implemented and validated for a quantitative description of the overall cell shape.

References

[1] R. Scorcioni, S. Polavaram, and G.A. Ascoli, "L-Measure: a web-accessible tool for the analysis, comparison and search of digital reconstructions of neuronal morphologies," *Nature Protocols*, vol. 3, pp. 866-876, Apr. 2008.
[2] http://www.farsight-toolkit.org/wiki/Trace_Editor

EMBEDDED SYSTEM BASED MONITORING SYSTEM FOR SUBSEA PIPELINES

Deepthi Badam*[1], Dr. Abdelhak Bensaoula[2]
Nitrides Materials and Devices Laboratory
[1]Departments of Electrical and Computer Engineering
[2]Departments of Physics and Electrical and Computer Engineering
University of Houston
Houston, TX 77204-4005

Abstract

The concept of employing embedded systems with sensor network to monitor subsea oil pipelines systems has been investigated by many researchers. This paper presents demonstration of a monitoring system using energy harvesting, microcontrollers and sensors and wireless communication. Underwater pipeline motion should be monitored periodically to prevent cracks, stress, leakage of oil, etc. which are a major threat for transportation of oil from seabed to platform atop sea. The temperature of the fluid in pipeline systems should be monitored because at certain low temperatures, hydrocarbons and gases solidify and form deposits, which are a major threat for oil transportation. The proposed system provides continuous data regarding acceleration, orientation and temperature of the pipelines, using integrated energy harvesting, sensors and microcontrollers.

Introduction

Major threats to underwater pipelines are hurricanes, earthquakes, third party interferences, pipeline corrosion etc. Oil Exploration companies constantly thrive to build a risk free pipeline system with full-scale returns. Especially, offshore oil exploration is more hazard prone and expensive, requiring voluminous research, technically qualified professionals, modern equipment for exploration, etc. for a break-even. Continuous monitoring of pipeline position, orientation and temperature is a major requirement for the safety and integrity of the pipeline system and also for the personnel working underwater or atop the sea. Monitoring systems can be achieved with the help of *embedded systems using sensors*, through *fiber optic sensing, periodical visual checking*, and several other methods.

Monitoring System Design

We have designed an embedded system, integrated on the pipe, which includes sensors to monitor its motion, position and temperature. The information can be transmitted using both an optical link and a wireless RF link. A receiver system located on a remotely operated vehicle (ROV) was also designed. The two systems communicate via an LED/photo detector pair and/or an RF transceiver. Fig. 1 shows the basic monitoring system using embedded systems communicating with sensors.

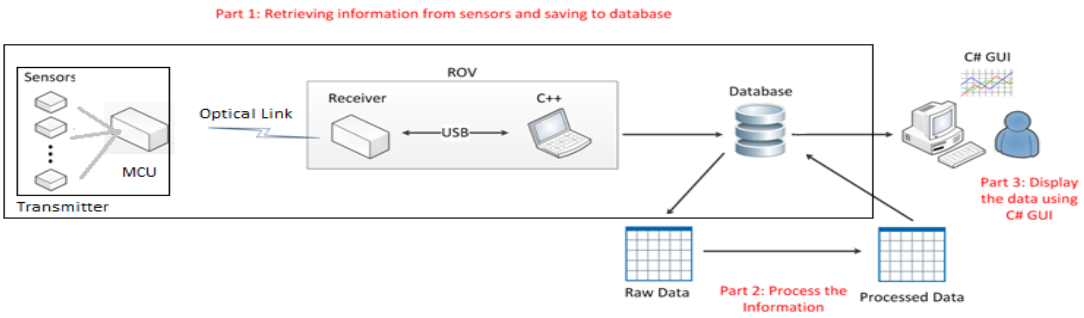

Fig.1 Basic Monitoring System

Microcontrollers and Sensors

The microcontrollers are selected for the purpose of communicating with the sensors and transmitting the data from the sensors to an ROV as seen in Fig 1. The data received in the ROV is processed to get meaningful information such as motion, orientation or the temperature of the pipeline. The microcontrollers are made to communicate with the ROV via an optical or RF link. The sensors used for pipeline motion and orientation consist of an accelerometer and magnetometer. Temperature is monitored through a thermistor.

The microcontrollers used for communicating with the sensors are MSP430 F2274 /FR5739 from TI. The microcontrollers communicate with sensors via the protocol I2C.In the case of optical communication the Microcontrollers and ROV communicate using UART protocol. In case of RF communication the microcontroller board has a transceiver (CC2500) attached to it. The transceiver communicates with similar transceiver on the ROV end for data transmission using SimpliciTI protocol. RF communication is tested using the development kits ez430 RF2500 that comes with the microcontrollers F2274 and transceiver CC2500.

References

[1] Application notes, Data Sheets, sample Codes from TI website on MSP430 FR5739/F2274 &CC2500. - http://www.ti.com/
[2] Application notes, Data Sheets, sample Codes from FreeScale website on Mag3110 and MMA845x. - http://www.freescale.com/

Acknowledgment

This work is part of the "Smart Joint Project" with Dr. Abdelhak Bensaoula, Alan Price, Sofiane Amara-Madi (University of Houston), in collaboration with Dr. Mounir Boukadoum (UQAM, Canada).

AN EMPIRICAL CHARACTERIZATION OF CONCRETE CHANNEL AND MODULATION SCHEMES WITH PIEZO-ELECTRIC TRANSDUCERS AND TRANSCEIVERS

Sai Shiva Kailaswar*[1] and Dr. Rong Zheng[2]
Wireless System Research Group
[1]Department of Electrical and Computer Engineering
[2]Department of Computer Science

Abstract

Structural Health Monitoring (SHM) is playing a vital role in improving the safety and maintainability of critical engineering structures. It is mainly used in the damage detection which adversely effect the throughput of the system. A network comprised of piezoelectric sensors and actuators can be used to monitor the concrete structures. The system comprise of data acquisition system to collect the data for further data analysis. Inspecting these nodes has become an arduous task due to the presence of high electromagnetic attenuation in concrete channels. A neoteric communication system is designed to understand the concrete channel in terms of typical response, diversity, bandwidth and linearity. The concrete channel was investigated with various types of approaches using different kind of signals and modulation schemes and tested using the proposed communication system. Bit Error Rate (BER) and Total Harmonic Distortion created by components in system are estimated.

Introduction

Concrete structures are found everywhere such as buildings, roads, bridges, and dams. If we look around standing at any random place on earth, we will encounter at least one concrete structure. They make life easier and comfortable. If we want to live longer, then the concrete structures around us should be long lasting. So, their importance in the modern world cannot be underestimated. Continuous monitoring of concrete structures is very much essential to prevent any disastrous events. Structural Health Monitoring (SHM) systems are modeled to test the health and performance by continuously monitoring the structures like bridges, dams, buildings, stadiums, platforms, airframes, or wind turbines. It is the process of invoking the damage detection scheme in concrete structures. Structural Health Monitoring is playing a vital role in improving the safety and maintainability of critical engineering structures. Continuous monitoring of structures is required as the catastrophic events can occur in an abrupt and unexpected manner. SHM systems help in detecting the damage with minimal human interaction.

Experiment Setup for measuring the transfer function of concrete channel

This experiment (Fig. 1) collects the samples of the input signal, amplified signal and the output signal. The collected samples were used for further data processing and analysis. Coherent detection method was used to find the frequency response of the channel. Experiment was performed for different sampling rates.

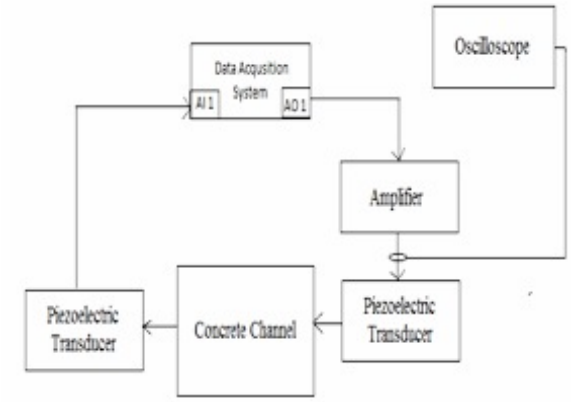

Fig. 1. Experimental setup

Communication System Design

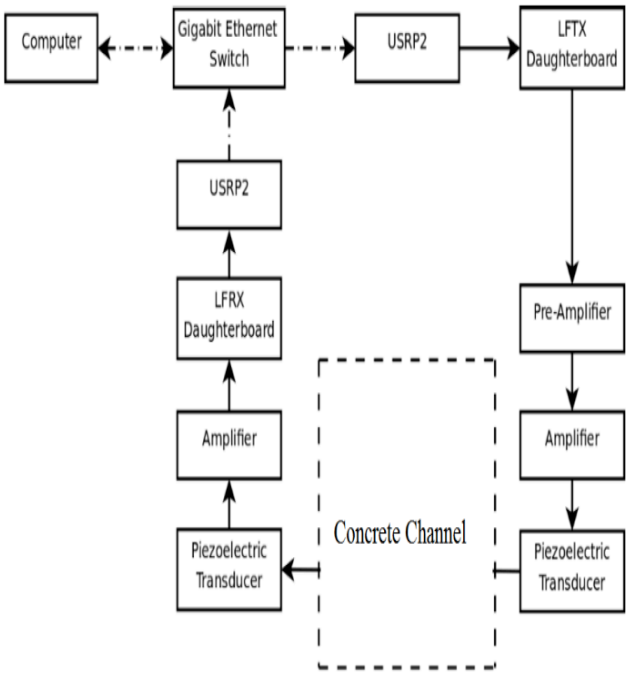

Fig 2. Block diagram of the communication system

A communication system (Fig. 2) was designed to evaluate the channel for different modulation schemes. GNU radio, an open source software development kit provides signal processing blocks to implement software radios is used to design the communication system in computer. Universal Software Radio Peripheral (USRP) connects the hardware to the computer using gigabit Ethernet switch. USRP is used to transmit and receive the signals from hardware. USRP has ADC and DAC to communicate between computer and hardware. This setup was used to implement different modulation schemes and to calculate SNR and BER from the received data. Multiple Input Multiple Output (MIMO) and Single Input Multiple Output (SIMO) setup are also to be implemented based on the same experimental setup.

References

[1] Joshua M. Kovitz, Rong Zheng, Gangbing Song, Zhi Ding, "Characterization of a concrete channel and feasibility testing of a concrete communications channel", *REU Student Research Program*

[2] http://gnuradio.org/redmine/projects/gnuradio/wiki/WhatIsGR

BIOMEMS DEVICE FOR REVASCULARIZATION OF ISLTES OF LANGERHANS

S. A. Das*[1, 3], F. Merchant[2] and W Zagozdzon-Wosik[1]
BioMEMS for Biological Samples at Cellular level Research Group
[1] Department of Electrical and Computer Engineering
[2] College of Technology
[3] Texas Center of Superconductivity
University of Houston
Houston, TX 77204-4005

Abstract

The Islets of Langerhans contain beta cells that secrete insulin to control the glucose level in the body. In treatment of diabetes type I, these islets can be extracted from a donor and transplanted. To alleviate damage of their vasculature caused by extraction, and to enable continuous flow of nutrients and oxygen, revascularization of the islets is critical. Our project is focused on in vitro culturing of endothelial cells on vascular-like network patterned Si substrates to form blood vessels and induce interaction of these blood vessels with the islets. We have evaluated the influence of substrate material properties such as mechanical, chemical and electrical, topology and topography, porosity and various environmental cues using 2D, 3D as well as sheet based configurations that will enable vascularization. To enable biodegradability of the substrate on implantation, we have fabricated and tested porous Si substrates with different pore size and porosity.

Introduction.

We have designed a BIOMEMS device, which provides mechanical support and specific patterns that facilitate vascular network formation for controlled EC growth and its interaction with islets. Patterns mimicking vascular network were implemented on silicon dioxide, nitride and borides as the substrate and their biocompatibility with endothelial cells and islets were examined. Both 2D and 3D scaffolds with structures in matrices of different geometries were fabricated using Si technology, to determine factors that affect cell growth and proliferation. In order to study the biodegradability needed for implantation of the device, porous silicon substrates were fabricated and tested.

Materials and design

Vascular-like network patterns in 2D were fabricated by optical lithography (Negative Futurrex photoresist) on silicon oxide, silicon nitride and titanium boride. The geometry and proximity of the patterns as well as their material layer properties and surface passivation, facilitated inter-cellular interaction during the process of adhesion, spreading and locomotion. To observe the contact guiding effect on cell growth and islet interaction in 3D, we made the 3D vascular network scaffold using optical lithography (Positive Futurrex photoresist) followed by wet and/or dry processes to form V and trapezoidal grooves. Grooves on the patterned network, for EC growth, were in sizes ranging from 5 to 60 μm width and 3.5 μm to 25 μm depth. The holes on the patterned network, for islets, were in the range of 100 μm to 500 μm diameter and 30 μm deep.

Human umbilical vein endothelial cells (HUVEC) were cultured to confluence, split and seeded on the cleaned and sterilized substrates for culturing. Cell cultures were maintained at 37°C with 5% carbon dioxide. The islets were introduced on the substrate

when a confluent monolayer of endothelial cells were observed. The cultured cells and islets were observed via transmitted light and fluorescence confocal microscopy using fluorescence dyes. Cellular interaction and formation of a monolayer of vascular networks on the substrate was observed.

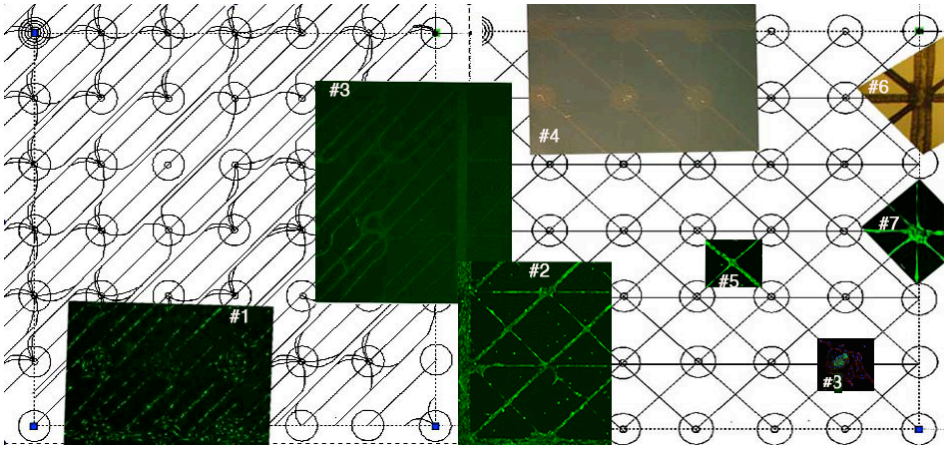

Fig. 1. Superimposed images of two substrate arrays for cell patterns in our BioMEMS, with endothelial cells growth and islet interaction obtained by optical or confocal microscopy
#1, #2, #3, #5 and #7: Confocal images of endothelial cells growing only on boride line and circle patterns indicating contact guidance in 2D.
#4: Optical image of endothelial cells adhering, growing and proliferating on TiB_2 patterns in 2D.
#6: Optical image of patterned grooves have V and trapezoidal shaped crossections. Cells mechanically interlock and grow in grooves if filled with gelatin.
#8: Confocal images of interaction of endothelial cells and islet. Blue (DAPI)-Endothelial cell nucleus. Green (Insulin)- Islet . Red (PECAM)- Endothelial cell membrane.

The porous silicon is electrochemically prepared by anodisation in HF Ethanoic solution at different current density for varying pore size and porosity.

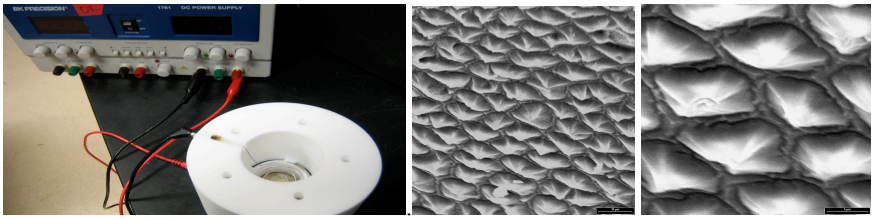

Fig. 2. Experimental setup for porous silicon fabrication. SEM images of porous silicon.

Results

Endothelial cells and islets responded to contact guiding selectively depending on the material and geometry used as well as on surface preparation. Adhesion, elongation, and growth of endothelial cells and their proliferation were obtained on biocompatible boride material. Porous silicon will be integrated as the substrate to enable biodegradability.

References

[1] L.T.Canham (Ed.), Properties of Porous silicon, *IEEE*, Stevenage (UK) 1997.
[2] G. Korotcenkov, B.K. Cho, "Silicon porosification: State of the art", *Critical reviews in Solid States and Material Sciences,* Taylor and Francis, 2010.

WHAT DRIVES LOCAL HOMEOSTATIC REGULATION OF SLEEP: LEARNING OR ATTENTION?

Ziyang Li*[1] and Bhavin R. Sheth[1,2]
[1]Department of Electrical and Computer Engineering
[2]Center for Neuro-Engineering and Cognitive Science
University of Houston
Houston, TX 77204-4005

Abstract

Studies have shown that increase in slow-wave activity (SWA) in specific regions of the sleeping brain is correlated with overnight improvement in performance on an attentionally demanding motor learning task. We wondered if the local, homeostatic regulation of sleep is associated with learning or with attention. In order to address this issue, we developed a "no learning" condition that purportedly places equivalent demands on attention but does not lead to learning. Sleep was monitored with classical polysomnography. Furthermore, high density electroencephalographic (EEG) data were recorded during sleep, and the average EEG power density of SWA for the first 30 min. of non rapid eye movement (nREM) sleep was computed. Behavioral performance before and after sleep were compared. The findings suggest that both the learning and "no learning" conditions produced a local increase in SWA in the parietal cortical region, and the spatial patterns across the scalp in the two conditions were statistically similar. No correlation was found between the overnight performance improvement which represents the overnight learning and the SWA change in the highlighted region. Our results indicate that overnight homeostatic regulation of sleep is not associated with overnight learning.

Introduction

During nREM sleep, neurons in cerebral cortex undergo slow oscillations, which appear in the EEG trace as SWA with frequencies less than 4 Hz. SWA during sleep increases as a function of prior wake, and decreases to baseline levels early in sleep. Thus, SWA is homeostatically regulated with the level of SWA controlled by the level of activity during prior wake [1]. Studies claim that the magnitude of synaptic change in cortical circuits during wake prior to sleep directly influences the intensity of SWA observed later during early nREM sleep. On the other hand, learning tasks typically demand high levels of attention and SWA intensity could be driven by attention demand instead.

A motor learning task is one way to compare these ideas. Successful motor task performance depends crucially on both learning and a high level of attention [2]. Here, we designed motor tasks (conditions) that variably engage learning mechanisms and/or place variable demands on attention and observed a) how these variations affected local components of sleep homeostasis and b) correlated changes in SWA in these conditions with different aspects of post-sleep performance.

Methods

Participants were required to do the out-and-back movements to a target using a pen-like cursor with their dominant hand on a digitizing tablet while the target and cursor position were displayed on the computer screen. Tasks recorded three errors: directional error,

linear error and timing error, along with the movement trajectories, and decided whether it was a "hit" or "miss" based on three judgments, as is shown on figure 1. A combined error (CE) measure that integrated three deviations was used to measure performance. Each participant (n=10) was trained and tested on three different conditions on three separate nights that were at least one week apart. The conditions differed in the amount and degree of rotation between the actual hand movement direction and displayed cursor movement direction. The "no rotation (NR)" and "random rotation (RR)" conditions did not engage learning mechanisms, while the "single rotation (SR)" and "random rotation (RR)" conditions were attentionally demanding. Brain signals were recorded using a 64+8-channel EEG system (BioSemi, Inc.) for each subject while (s)he slept immediately after the motor task. Sleep stage scoring was outsourced (Morpheus, WideMed, Inc.).

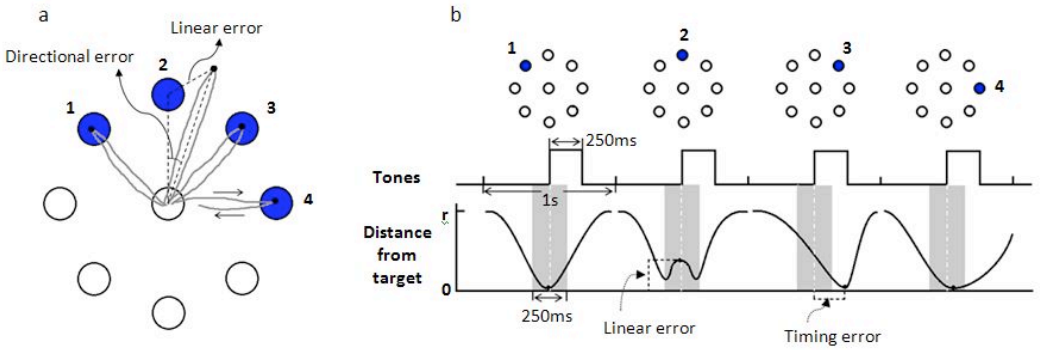

Fig. 1. Illustration of the task and measurement with four example movements, 1 is a successful hit, 2, 3 and 4 illustrate large linear error, large timing error and no-return, respectively.

Results

Behavioral results - Pre-post-sleep behavioral performances for three conditions were compared. Combined error (CE) on SR significantly decreased ($p<0.01$) overnight, while no significant change in CE on the RR or NR (control) conditions were found. In addition to CE, five other parameters of task performance were also compared.

Scalp EEG results - Topological plots of average power density in the delta band (SWA) for the first 30 min. of nREM sleep on SR/NR and RR/NR were compared. Both showed a local increase in the left parietal region, contralateral to the hand used. A statistical comparison of the two percentage change topological plots yielded significant similarity indicating similar changes in SWA in the learning (SR) and no-learning (RR) conditions.

Correlation results - No significant correlation between the overnight CE decrease in the SR condition and SWA increase in the parietal region was found, again arguing against the idea that overnight learning drives local increase in SWA across the cortical surface.

References

[1] R. Huber, M. F. Ghilardi, M. Massimini, and G. Tononi, “Local sleep and learning,” *Nature*, vol. 430, pp. 78-81, July 2004.

[2] M. F. Ghilardi, C. Ghez, et al. “Patterns of regional brain activation associated with different forms of motor learning,” *Brain Research*, vol. 871, pp. 127-145, April 2000.

DEISGN OF A MULTI-CHANNEL TMS COIL

Ruoli Jiang*, Ben H. Jansen, Bhavin R. Sheth, and Ji Chen
Department of Electrical and Computer Engineering
University of Houston
Houston, TX 77204-4005

Abstract

Most behaviors arise from the interaction between different brain areas. Investigations of the causal involvement of particular brain areas and interconnections in behavior require an external stimulation system with reasonable spatio-temporal resolution. Current trans-cranial magnetic stimulation (TMS) technology is limited to stimulating a single brain area once in a given trial. Here, we present a feasibility study for a novel TMS system based on multi-channel reconfigurable coils, and present computer simulations and bench experiments to show its feasibility. With this hardware, researchers will be able to stimulate multiple brain sites in any temporal order in a trial.

Introduction

Interactions between different brain areas affect most behaviors. These areas receive and send neural information asynchronously in time. Studying the flow and processing of information in the brain demands the ability to stimulate multiple brain sites in any temporal order with reasonable spatial resolution. Transcranial magnetic stimulation (TMS) is such a technology that provides an external stimulus to the brain.

TMS is a noninvasive method to cause depolarization or hyper-polarization in the neurons of the brain. TMS systems generate a brief, high current pulse that is fed into a coil of wire, called the magnetic coil, which is placed above the scalp. A magnetic field is produced with lines of flux passing perpendicularly to the plane of the coil. Subsequently, an electric field is induced inside the cortex, perpendicularly to the magnetic field.

However, current TMS technology has some limitations. The location of stimulus is uncertain to some degrees because the coils are relatively large. Since the coil is held by hand, coil movement is also inevitable. Furthermore, the stimulation is limited to a single, fixed location. The brain is a complex inter-connected network; information processing involves multiple brain areas. In order to investigate the brain function, we need to stimulate multiple brain sites in any temporal order.

Method

We are developing a wire-mesh coil. It is constructed using x-directional and y-directional wires, laid relatively close to each other but otherwise electrically insulated. By varying the direction and/or strength of the current on each wire, we can configure this wire-mesh coil into a standard loop coil and figure-eight coil of varying size.

Bench Experiment

In order to validate the proposed approach, experimental investigations have been performed. Eight x-directional and eight y-directional grooves were cut in a plywood board. Multi-strand copper wire was placed in the grooves to form a figure-eight coil. A

plastic container filled with a saturated solution of pure salt (NaCl) in water was placed on top of the board to simulate the environment inside the skull. The figure-eight coil was connected to a Magstim Rapid stimulator which provided the current pulses. A probe was placed into the saline on top of the figure-eight coil to measure the amplitude of magnetic field. The result is shown in Figure 1

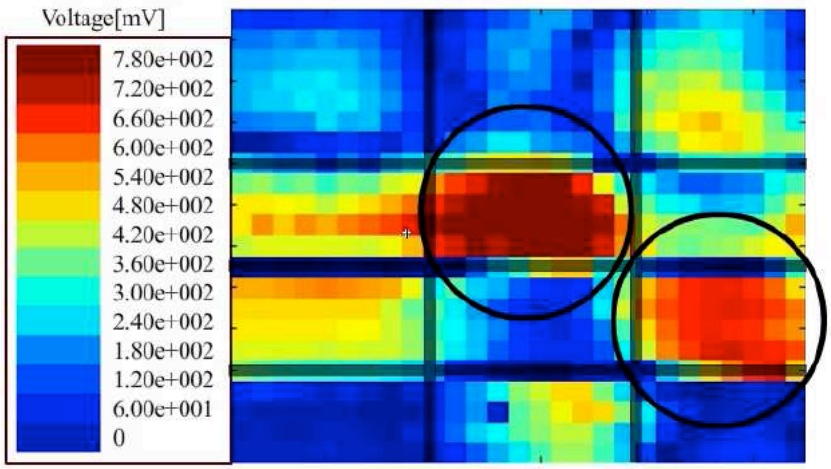

Fig. 1. Magnetic field measured 1 cm above plane of wire-mesh coil. Straight lines show the location of the wires that make up the mesh coil. The circles denote the areas with high magnetic field.

As can be seen, peak values of the induced magnetic field occur at the two branches of the figure-eight coil. This result matches those produced through a simulation using Ansoft Maxwell 12. Also, these simulations showed that a current, perpendicular to the line connecting the areas of maximum magnetic field, is produced.

Conclusions

The proposed wire-mesh reconfigurable coil is relatively easy to fabricate.

However, our wire-mesh system has some limitations. For example, it can produce only four induced current directions (45, 135, 225 and 315 degrees), which are achieved by varying the current directions. Also the bench experiments and simulations show that there are also significant fields and currents outside the intended stimulation area arising from the wires feeding the figure-eight coil. We are currently exploring alternative configurations to minimize these effects.

INVESTIGATION OF FEED LINE EFFECTS ON FIELDS FROM BROADBAND OVER POWER LINE COMMUNICATIONS

Anthony Y. Lau*, David R. Jackson, and Donald R. Wilton
Applied Electromagnetics Laboratory
Department of Electrical and Computer Engineering
University of Houston
Houston, TX 77204-4005

Abstract

With the advent of broadband over power line (BPL) for high-speed data transmission and emerging interest in grid modernization, the appeal of signal transmission on a power line above the earth is significant. One important issue is the nature of the fields in the vicinity of the power line, since regulatory agencies place restrictions on the intensity level. The field surrounding the feeding structure and lines for a two-wire system over the earth is examined here. Various models are used in the investigation, ranging from very simple to more sophisticated. In the simplest approach, the earth is modeled as a perfect conductor, and simple image theory [1] is used. A more sophisticated approach, which uses the spectral-domain immittance (SDI) method [2] to account for the finite conductivity of the earth, is also used in the investigation.

Introduction

In March 2004, a technology agenda to diversify the availability of broadband carriers was released by the White House that spurred the deployment of broadband over power line technology [3]. With the June 2011 White House grid modernization initiative [4], BPL has gained a part in the development of a clean-energy economy. However, there are some issues with the technology such as the radiated fields from BPL signals. BPL systems basically use a technology that overlays radio frequency signals on transmission lines designed for power-line frequencies. BPL operates across a band from 2 to 30 MHz while power distribution operates around 50 or 60 Hz [5]. Since BPL uses a pair of power lines as the waveguiding structure, the broadband signal is essentially being transmitted on a structure intended for another frequency that differs by several orders of magnitude. Further, the feeding mechanisms that connect the signal source to the power lines have the potential to be effective field emitters. This raises concern regarding emissions produced by BPL signals and corresponding interference issues. Figure1 shows a simple perfectly-conducting earth model that was used to generate the pattern in Fig. 2.

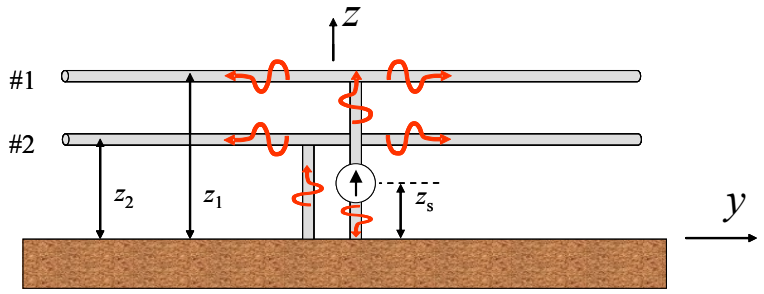

Fig. 1. Model of BPL system used in producing the fields shown in Fig. 2 Note that the power pole is not shown but it does exist between the two vertical wires (gray vertical lines).

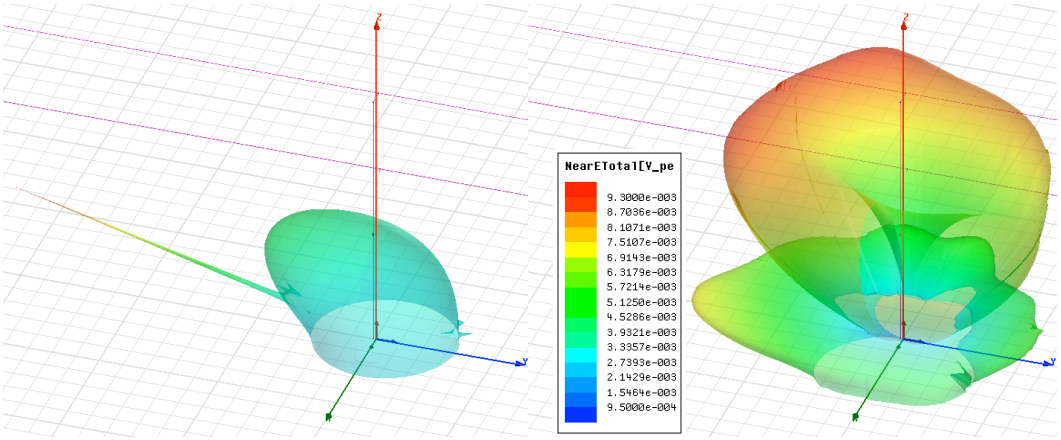

(a) (b)

Fig. 2. Magnitude of the total electric field from a 1V source observed at 30 meters from the base of the power pole using the model in Fig. 1 (a perfect conducting earth) for (a) 3 MHz and (b) 30 MHz, obtained via the electric field integral equation (EFIE) method of moments (MoM) [6] technique that demonstrate the potential for radiation emission by a BPL system. The power lines can be seen as the dotted lines.

References

[1] Pozar, David M. *Microwave Engineering*, 3rd Ed. Hobroken: John Wiley & Sons, 2005.

[2] T. Itoh, "Spectral Domain Immittance Approach for Dispersion Characteristics of Generalized Printed Transmission Lines," *IEEE Trans. Microwave Theory and Techniques*, vol. 28, no. 7, pp. 733-736, July 1980.

[3] "Promoting Innovation and Economic Security Through Broadband Technology" The White House, 26 Apr. 2004. Web. 2 Jan. 2007

[4] OSTP, CEQ, DOE, USDA, DOI, NIST. *Administration Announces Grid Modernization Initiatives to Foster a Clean Energy Economy and Spur Innovation*. Building the 21st Century Grid. Washington: GPO, 13 July 2011. Print.

[5] Olsen, Robert G. *Technical Considerations for Broadband Powerline (BPL) Communication*. WA: WA State UP, Feb. 2005.

[6] Harrington, Roger F. *Field Computation by Moment Methods*. New York: IEEE Press, 1993.

PHOTOVOLTAIC CHARGING OF PLUG-IN HYBRID ELECTRIC VEHILES WITH A SMART GRID INTERFACE

P. Goli*[1,2] and W. Shireen[1,2]
Power Electronics and Renewable Energy Systems Research Lab
[1] Department of Electrical and Computer Engineering
[2]College of Technology
University of Houston
Houston, TX 77204-4005

Abstract

It has been estimated that, there will be one million Plug-In Hybrid Electric Vehicles (PHEVs) by the end of this decade. There is a growing risk that, this proliferation in the number of PHEVs will trigger extreme surges in demand while charging them during rush hours. To mitigate this impact, a unique charging station architecture is proposed in which the rate of charging of the PHEVs is controlled in such a way that the impact of charging during peak load period is not felt on the grid. The power needed to charge the plug-in hybrids comes from grid-connected photovoltaic generation or the utility or both. A unique control strategy based on DC bus voltage sensing is proposed for the above system for efficient transfer of energy. By using the proposed control strategy, the operations of charging station can be categorized into four modes: grid-connected rectification, PV charging and grid- connected rectification, PV charging, PV charging and grid-connected inversion.

Introduction

There would be one million plug-in hybrid electric vehicles on the road by the year 2015 [1, 2]. This will add extra load to the already overloaded U.S grid. Though the increase in awareness about PHEVs is a healthy development, it's the customer who makes the final call as to when and how to charge their vehicles, which could mean challenges for electric utilities and charging service providers. Hence, there is an immediate need to develop charging station infrastructure integrating renewable energy with smart grid technologies. The proposed charging station will charge the PHEVs from the photovoltaic system, thus reducing the stress on the grid. When the grid is at peak and solar power is insufficient to charge the PHEVs then the charging station would enable vehicle charging to be delayed or temporarily interrupted. The charging station also includes an energy storage unit (ESU) which consists of a battery bank to store energy during off peak hours which can be used during emergencies to charge the PHEVs.

Proposed Architecture

The proposed charging station architecture is presented in block diagram in Figure 1. The main components of the charging station are the PCU, PV array, energy storage unit and the controller. The PCU consists of a DC/DC boost converter, which also performs the function of maximum power point tracking (MPPT), a DC/DC buck converter with battery management system (BMS), an energy storage unit (ESU) and a DC/AC bi-directional grid tied converter. The BMS prevents the PHEV from getting overcharged and also controls the rate of charge when the situation demands. The ESU will support the charging of PHEV when there is no power available either from the grid or the PV system. The battery pack in the ESU can be charged by the grid during off peak hours.

The controller monitors and controls the direction of power flow in the system. As shown in Figure 1 the operation of the control algorithm is based on five inputs among which $V_{DC.bus}$, SOC and I_{DTR} are used for taking decisions to determine the direction of power flow [3, 4]. By using the proposed control strategy, the operations of charging station can be categorized into four modes: grid-connected rectification, PV charging and grid-connected rectification, PV charging, PV charging and grid-connected inversion.

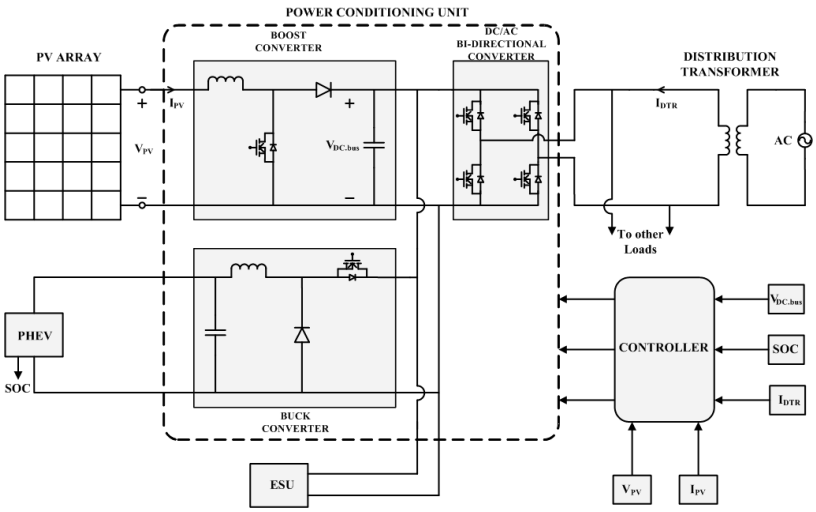

Fig. 1. Detailed block diagram showing the PCU and controller in detail

Conclusions

This paper proposes a charging station architecture by using a combination of photovoltaic system and smart charging strategies. A unique control strategy based on DC bus voltage sensing, which decides the direction of power flow is presented. The proposed charging station architecture in a parking lot features advantages such as low cost, pollution free environment, and low maintenance. Therefore, charging a PHEV using solar power is one of the most attractive options, to create an energy-wise, cost effective, and overall sustainable society.

References

[1] J. Voelckar, "One Million Plug-in Cars by 2015" *IEEE Spectrum*, vol. 48, issue 4, pp 11-13, April 2011.

[2] S.W. Hadley, "Evaluating the impact of Plug-in Hybrid Electric Vehicles on regional electricity supplies," *Bulk Power System Dynamics and Control - VII. Revitalizing Operational Reliability, 2007 IREP Symposium*, vol., no., pp.1-12, 19-24 Aug. 2007.

[3] G. Gamboa, C. Hamilton, R. Kerley, S. Elmes, A. Arias, J. Shen, and I. Batarseh, "Control strategy of a multi-port, grid-connected, direct-DC PV charging station for plug-in electric vehicles," *Energy Conversion Congress and Exposition (ECCE), 2010 IEEE* , vol., no., pp.1173-1177, 12-16 Sept. 2010.

[4] Z. Li, T. Wu, Y. Xing, K. Sun, and J.M. Gurrero, "Power control of DC microgrid using DC bus signaling," *Applied Power Electronics Conference and Exposition (APEC)*, 2011.

DYNAMIC MPPT CONTROL OF A PV MODULE UNDER FAST CHANGING OPERATING CONDITIONS

R. Kotti*[1,2] and W. Shireen[1,2]
Power Electronics and Renewable Energy Systems Research Lab
[1]Department of Electrical and Computer Engineering
[2]College of Technology
University of Houston
Houston, TX 77204-4005

Abstract

This paper presents a new high performance, dynamic maximum power point tracking method of a photovoltaic (PV) module under fast changing operating conditions. A DC-DC boost converter serves as a Power Conditioning Unit (P.C.U) to coordinate the operating point with the maximum power point of the PV module. The proposed algorithm uses a scanning technique, to measure the maximum power delivering capacity of the panel and extracts the same by the proposed algorithm under different operating conditions. The algorithm is simple to implement and easy to execute with high tracking efficiency. The proposed method is successfully implemented, analyzed and verified in Mat-lab/Simulink software. The results obtained for various load and irradiation conditions at very short time intervals verify that the proposed maximum power point tracking (MPPT) control provides a fast and efficient tracking.

Introduction

Today photovoltaic power generation contributes nearly 0.089% of the total global power demand. Power generated using PV technology is increasing drastically; this increase can be witnessed clearly from 7.5GW production in 2009 to 17GW production in 2010. The increase is estimated to touch 1% of total power generation by 2030 [1]. The impediments we are facing in this low maintenance, fuel absent, noise and pollution free system are installation cost and efficiency. The installation cost is going down due to improvements in panel productions due to advances in PV physics. The low efficiency is due to the offset that's always present in coordination of the maximum power point and operating point of the PV panel due to the system characteristics. The efficiency can be improved by tracking and extracting the maximum power available at all operational conditions dynamically by using a maximum power point tracking (MPPT) algorithm. The highest efficiency of the PV panels available at present is 21%, which can be improved to 30% in real time scenarios depending on the tracking efficiency of the MPPT algorithm incorporated.

There are many MPPT algorithms that have been proposed and compared to track the maximum power point. The most widely used ones are "Hill climbing Algorithm", "Perturb & Observe (P&O)" and their modifications. These algorithms provide good results for stable and slow varying irradiation conditions and temperature. The major drawback of these algorithms is that the system oscillates about the MPPT and fails for shading condition, where multiple peaks comes into play. There is always a tradeoff between accuracy and speed. The incremental conductance method is a bit more sophisticated and gives a stable MPPT, with a variable step size to track MPPT. This algorithm holds well as long as $\Delta P/\Delta V$ truly provides the measure of distance from

maxima. Which is true for slow irradiations and moreover the P-V slope changes with change in irradiation level. The algorithms based on PV module MPP locus characterization and single parameter control made quite an impact in tuning the approach of MPPT in a different direction. These gave a satisfactory result based on the constraints imposed on them, but the complexity of the design and implementation proved to be disadvantageous. With the increase of PV installation in urban regions a new problem, shading came into existence. Many algorithms were proposed to find the MPPT under shading condition. Other widely used MPPT techniques are the constant voltage (CV) and constant current (CC). CV and CC are based on the fact that the MPP voltage and MPP current bear approximate linear relationship with open circuit voltage and short circuit current respectively. These methods offer a very fast tracking but the linear approximation may result in a slight deviation from the actual MPPT. Also there is a power loss when the circuit is short circuited for obtaining the proportionality constant K which is dependent on temperature.

The method proposed is a successful simulated attempt to avoid all the constraints or disadvantages posed for the earlier discussed methods. The approximation seen in CV & CC methods does not exist and the power loss in sensing the maximum power is reduced to 0.01%. The fast irradiation, temperature and load change does not affect the efficiency of the algorithm as seen in 'HCS', 'P&O' and 'INC' and even the global maximum is found under shading conditions through scanning.

References

[1] Renewables 2011 Global Status Report. www.ren21.net.

[2] T. Esram, P.L. Chapman, "Comparison of Photovoltaic Array Maximum Power Point Tracking Techniques," *Energy Conversion, IEEE Transactions*, vol.22, no.2, pp.439-449, June 2007.

[3] S. Jain, V. Agarwal, "Comparison of the performance of maximum power point tracking schemes applied to single-stage grid-connected photovoltaic systems," *Electric Power Applications, IET,* vol.1, no.5, pp.753-762, Sept. 2007.

[4] Xiao Weidong, W.G. Dunford,"A modified adaptive hill climbing MPPT method for photovoltaic power systems," *Power Electronics Specialists Conference, 2004.PESC 04.2004 IEEE 35th Annual*, vol.3, no., pp. 1957- 1963 Vol.3, 20-25 June 2004.

[5] Dong-Yun Lee, Hyeong-Ju Noh, Dong-Seok Hyun, Ick Choy , "An improved MPPT converter using current compensation method for small scaled PV-applications," *Applied Power Electronics Conference and Exposition, 2003. APEC '03. Eighteenth Annual IEEE*, vol.1, no., pp. 540- 545 vol.1, 9-13 Feb. 2003.

[6] S. Yuvarajan, Xu Shanguang, "Photo-voltaic power converter with a simple maximum-power-point-tracker," *Proceedings of the 2003 International Symposium on Circuits and Systems, 2003. ISCAS '03*, vol.3, no., pp. III-399- III-402 vol.3, 25-28 May 2003.

[7] S. Patel, W. Shireen, "Fast converging digital MPPT control for photovoltaic (PV) applications," *Power and Energy Society General Meeting, 2011 IEEE* , vol., no., pp.1-6, 24-29 July 2011.

COLLABORATIVE COMPRESSIVE SENSING BASED DYNAMIC SPECTRUM SENSING AND MOBILE PRIMARY USER LOCALIZATION IN COGNITIVE RADIO NETWORKS

Lanchao Liu*[1], Zhu Han[1], and Zhiqiang Wu[2]
Wireless Networking, Signal Processing and Security Research Group
[1] Department of Electrical and Computer Engineering
University of Houston
Houston, TX 77204-4005
[2] Department of Electrical Engineering
Wright State University
Dayton, OH 45435

Abstract

In wideband cognitive radio (CR) networks, spectrum sensing is one of the key issues that enable the whole network functionality. Collaborative spectrum sensing among the cognitive radio nodes can greatly improve the sensing performance, and is also able to obtain the location information of primary radios (PRs). Most existing work merely studies the cognitive radio networks with static PRs, yet how to deal with the situations for mobile PRs remains less addressed. In this paper, we propose a collaborative compressive sensing based approach to estimate both the power spectrum and locations of the PRs by exploiting the sparsity facts: the relative narrow band nature of the transmitted signals compared with the broad bandwidth of available spectrum and the mobile PRs located sparsely in the operational space. To effectively track mobile PRs, we implement a Kalman filter using the current estimations to update the location. To handle dynamics in spectrum usage, a dynamic compressive spectrum sensing algorithm is proposed. Joint consideration of the above two techniques is also investigated. Simulation results validate the effectiveness and robustness of the proposed approach.

Introduction

The rapid development in wireless communication has given rise to a tremendous demand on scarce spectrum resources. Nowadays, most frequency spectrum bands are under-utilized due to the fixed spectrum assignment policy. To increase the spectral efficiency, cognitive radio (CR) [1] has emerged as a promising technology to enable access of unoccupied frequency. One fundamental task of each CR nodes in cognitive radio network is spectrum sensing [2] i.e. to detect the presence of the licensed users, also known as the primary radio (PR) nodes, as well as the available unoccupied spectrum. Furthermore, the proliferation of CR devices has fostered the demand for context-aware applications, in which the location information of PRs is viewed as one of the most significant contexts.

In wideband spectrum sensing, CR nodes have to scan multiple frequency bands, which causes long sensing delay or incurs higher computational complexity. Generally, the occupied bands of PRs are often narrow compared to the overall bands scanned. In addition, the active PRs distributed sparsely in the operational area. These spasities in spectrum occupation and locations inspire researchers to adopt the recently emerging compressive sensing (CS) [3-5] technology, which is now widely utilized in wireless communication [6], to effectively sample the wideband signals. By utilizing the fact that a signal is sparse or compressible in some domain, the CS technique can powerfully

acquire a signal from a small set of randomly projected measurements with the sampling rate much lower than the Nyquist sampling rate. Then, efficient methods such as basis pursuit (BP) [7], orthogonal matching pursuit (OMP) [8] can be used to reconstruct the original signal. Once the signal is recovered, the spectrum usage and location information of the PRs can be identified.

Exploiting the CS technique, the spectrum sensing and PR localization problem are well studied in [9]. However, existing work mostly investigated the CR network with static PRs. In general, many factors in practice (such as the mobility of PRs and the dynamical spectrum usage) may significantly compromise the detection performance in spectrum sensing. Thus, a more efficient sensing mechanism is needed to handle the dynamics in a practical cognitive radio network.

In this project, we extend our previous work [10] on compressive spectrum sensing to the spectrum sensing and localization problem. To track the location changes of mobile PRs, we implement a Kalman filter to predict the locations of PRs accurately in an intelligent way. Furthermore, dynamic spectrum sensing algorithm is adopted to update the spectrum usage information quickly and reliably. Joint consideration of Kalman filter and dynamic spectrum sensing is also proposed so as to reduce the searching region and reduce the complexity. Simulation results show efficiency and effectiveness of our proposed approach.

References

[1] E. Hossain, D. Niyato, and Z. Han, *Dynamic spectrum access in cognitive radio networks*, Cambridge University Press, 2009.

[2] I. F. Akyildiz, B. F. Lo, and R. Balakrishnan, "Cooperative spectrum sensing in cognitive radio networks: a survey," *Physical Communication (Elsevier) Journal*, Vol. 4, No. 1, pp. 40-62, Mar. 2011.

[3] D. Donoho, "Compressed sensing," *IEEE Transactions on Information Theory*, Vol. 52, No. 4, pp. 1289-1306, Apr. 2006.

[4] E. Candes, and T. Tao, "Near optimal signal recovery from random projections: Universal encoding strategies? " *IEEE Trans. on Information Theory*, Vol. 52, No. 12, pp. 5406-5425, Dec. 2006.

[5] R. Baraniuk, "Compressive sensing," *IEEE Signal Processing Magazine*, Vol. 2, Iss. 4, pp. 118-121, Jul. 2007.

[6] Y. Li, Z. Han, H. Li, and W. Yin, *Compressive Sensing for Wireless Networks*, contract with Cambridge University Press, 2012.

[7] S. S. Chen, D. L. Donoho, M. A. Saunders, "Atomic decomposition by basis pursuit," *SIAM Journal on Scientific Computing*, Vol. 20, No. 1, pp. 33-61, 1998.

[8] J. Tropp, A. Gilbert, "Signal recovery from random measurements via orthogonal matching pursuit," *IEEE Transactions on Information Theory*, Vol. 53, Iss. 12, pp.4655-4666, Dec. 2007.

[9] J. -A. Bazerque and G. B. Giannakis, "Distributed spectrum sensing for cognitive radio networks by exploiting sparsity," *IEEE Transations on Signal Processing*, Vol. 58, Iss. 3, pp. 1847-1862, Mar. 2010.

[10] J. Meng, W. Yin, H. Li, E. Hossain, and Z. Han, "CollaborativebSpectrum Sensing from Sparse Observations in Cognitive RadiobNetworks," *IEEE Journal on Selected Topics on Communications, special issue on Advances in Cognitive Radio Networking and Communications*, Vol. 29, Iss. 2, pp. 327 - 337, Feb. 2011

DEVICE FINGERPRINTING TO ENHANCE WIRELESS SECURITY USING NONPARAMETRIC BAYESIAN METHOD

Nam Tuan Nguyen*[1], Guanbo Zheng[2], Zhu Han[1] and Rong Zheng[2],
Wireless Networking, Signal Processing and Security Research Group
[1]Department of Electrical and Computer Engineering
[2]Computer Science Department
University of Houston
Houston, TX 77204-4005

Abstract

Each wireless device has its unique fingerprint, which can be utilized for device identification and intrusion detection. Most existing literature employs supervised learning techniques and assumes the number of devices is known. In this paper, based on device-dependent channel-invariant radio-metrics, we propose a non-parametric Bayesian method to detect the number of devices as well as classify multiple devices in a unsupervised passive manner. Specifically, the infinite Gaussian mixture model is used and a modified collapsed Gibbs sampling method is proposed. Sybil attacks and masquerade attacks are investigated. We have proven the effectiveness of the proposed method by both simulation data and experimental measurements obtained by USRP2 and Zigbee devices.

Introduction

Due to the broadcast nature of wireless medium and programmability of wireless devices, identity of legitimate wireless devices can be easily spoofed. For instance, an ioctl system call in the Linux kernel can modify the MAC address of a network interface card. Modifying or replacing the EPROM in a phone would allow the configuration of any ESN (Electronic Serial Number) and MIN (Mobile Identification Number) via software for cellular devices. Once the device identity is compromised, multiple attackers can masquerade as a single legitimate user, or a single attacker can assume multiple legitimate identities. In both cases, many forms of attacks can be launched including Sybil attacks, masquerade attacks, resource depletion, traffic injection, denial of service, etc.

Existing solutions to the detection of identity spoofing roughly fall into two categories, namely, active detection and passive detection. In active detection, additional messages are exchanged among many network entities. For instance, cryptographic based schemes can be used to either authenticate users or elicit user specific responses [5]. In [6], a simple active method is proposed for discovering facts about the chipset, the firmware or the driver of an 802.11 wireless device by observing its responses (or lack thereof) to a series of crafted non-standard or malformed 802.11 frames. Active detection methods require extra message exchange. Furthermore, responses that are firmware, driver, OS dependent can be spoofed as well. In contrast, passive detection methods extract device or location specific features from message transmissions. Device specific features typically include, clock skew, sequence number anomalies, timing, and various RF parameters. Location dependent features are typically radio signal strength (RSS) vectors measured at trusted devices. The disadvantage of location based features is that RSS measurements are time varying and have low spatial resolutions. Devices a few meters apart in an indoor environment may have similar RSS features. In this paper, we propose

to use device dependent radio-metrics as fingerprints to detect identity spoofing. A radio-metric is a component of radio signal such as amplitude, frequency, phase or any feature derived from those components. Each device creates a unique set of radio-metrics in its emitted signal due to hardware variability during the production of the antennas, power amplifiers, ADC, DAC, etc. As a result, radio-metrics cannot be altered post-production and thus provide a reliable means for identification. Choosing which radio-metrics to form the device fingerprints is technology dependent. Different modulation techniques have different sets of radio-metrics.

Our approach differs from existing work in the following aspects. First, the features selected are channel invariant. Second, it is a passive detection method that does not require out-band message exchanges. Third, most importantly, our method is based on an unsupervised clustering approach. There is no need to register legitimate devices and obtain training sequences to set up a database of feature space of legitimate devices. Furthermore, it does not assume a priori knowledge regarding the number of devices present in the networks. We model the feature space of a single device as a multi-variable Gaussian distribution with unknown parameters, and that of multiple devices (of the same or different device IDs) as an infinite Gaussian mixture (though only a finite subset are observed). We develop a non-parametric Bayesian approach to unsupervised clustering with an unbounded number of mixtures. Specifically, we define a prior over the likelihood of devices using the Dirichlet distribution [9] . Based on the properties of the Dirichlet distribution, we derive a Gibbs sampling algorithm that can be used to sample from the posterior distribution, and determine the number of clusters. Output of the algorithm is given in the following figure:

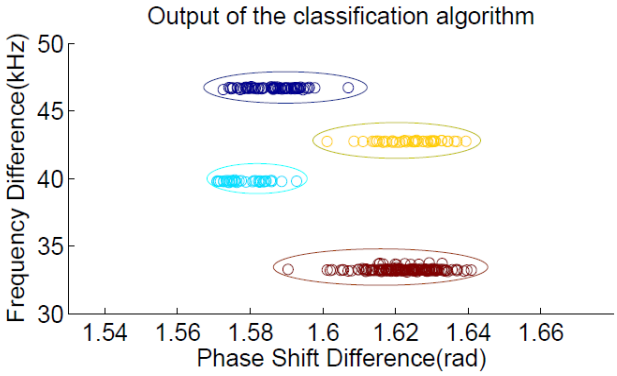

Figure 1. Collected fingerprint of 4 devices.

References

[1] K. Xing and X. Cheng, "From Time Domain to Space Domain: Detecting Replica Attacks in Mobile Ad Hoc Networks", in proceedings of the *29th Conference on Information Communications*, San Diego, California, USA, March 2010.
[2] S. Bratus, C. Cornelius, D. Kotz, and D. Peebles"Active behavioral Fingerprinting of Wireless Devices", in proceedings of the *1st ACM Conference on Wireless Network Security*, Alexandria, VA, USA, March 2008.
[3] Y. W. Teh, Dirichlet Processes, *Encyclopedia of Machine Learning*, Springer, New York, 2007.

ROBUST REFLECTOR PLACEMENT IN 60GHZ MMWAVE WIRELESS PERSONAL AREA NETWORKS

Guanbo Zheng*[1] and Rong Zheng[1, 2]
[1] Department of Electrical and Computer Engineering
[2] Department of Computer Science
University of Houston
Houston, TX 77204-4005

Abstract

This work addresses the problem of minimum reflector placement and explicitly account for network dynamics due to blockages of direct paths in mmWave WPANs. Our main goal was to 1) Characterize the geometric constraints of link connectivity in 60GHz mmWave WPANs, 2) Propose a robust formulation for the minimum reflector placement problem in mmWave WPANs to combat link blockage based on the D-norm uncertainty, and complete 3) Evaluation using the CPLEX solver is provided to validate our formulation and model. Detailed contributions will be discussed.

Introduction

The mmWave radio has several unique physical characteristics. First, the propagation and attenuation loss are much more severe in 60 GHz band. The penetration loss is also much higher through some typical building materials [1-2]. To combat such significant signal degradation, by using steerable beamforming on both transmitter and receiver sides, mmWave radio can obtain significant gain in received signal strength, while incurring negligible interference from other radios [3-4]. In the case of non-line-of-sight paths, reflectors can be utilized to relay data between pairs of transmitters and receivers.

In this paper, we address the minimum reflector placement problem, which finds the minimum number of reflectors and their best placements from a set of candidate locations subject to the bandwidth and robustness constraints. Two vertex-disjoint paths (one is denoted as the primary path and the other as the secondary path) are provisioned for each pair of transmitter and receiver, which allows immediate switch of routing to the secondary path in case of channel degradation or blockage on the primary path, thus avoiding the disruption of service to upper layer application.

Network Model and Problem Formulation

Fig. 1 gives the simple model to demonstrate the visibility region of two mmWave devices, DEV1 and DEV2. The visibility region of DEV1 is a bounded polygon composed by the line segments in dark yellow and its transmission radius. As shown in the shadow area, there is an overlapped visibility region between DEV1 and DEV2, which is the candidate region for placing reflectors.

We consider an mmWave WPAN with a set of N mmWave links. Each link $i \in N$ is associated with a trasmitter s_i, a receiver d_i and a flow rate r_i. Reflectors are the devices that can relay transmission between transmitters and receivers, which can be placed at a set of K candidate locations. There exists a set of M obstacles with known locations.

The robust minimum reflector placement (RMRP) problem can be formally stated as:

$$\begin{aligned}
\text{Minimize}_{\mathbf{x},\mathbf{y},\mathbf{z}} \quad & \sum_k z_k \\
\text{subject to} \quad & \sum_{i \in L_k} \eta_i x_{ik} r_i \tau_{ik} + g_k(\mathbf{y_k}, \mathbf{r}) \leq z_k, \forall k, \\
& \tau_{ik} = \frac{1}{R_{s_i,k}} + \frac{1}{R_{k,d_i}}, \\
& \sum_{k=1}^{K} x_{ik} = \eta_i, \sum_{k=1}^{K} y_{ik} = 1, \forall i \in \Omega. \\
& x_{ik} + y_{ik} \leq 1, \forall i \in L_k, \forall k \\
\text{variables} \quad & x_{ik}, y_{ik}, z_k \in \{0,1\}, \forall i \in \Omega, k = 1, \ldots, .
\end{aligned}$$

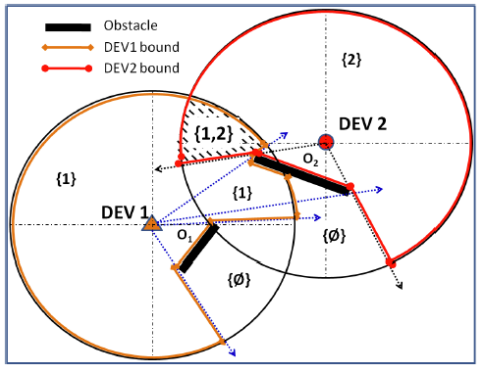

Fig. 1. The overlapped visibility region

Performance Evaluation

In the simulation, N mmWave devices (red triangles) and M obstacles (black bars) are uniformly placed in a 100m x 100m region. The reflectors (blue dot) are located in grid points in this area with a separation d_0 between neighboring reflectors. The transmission radii of mmWave devices and reflectors are 30m.

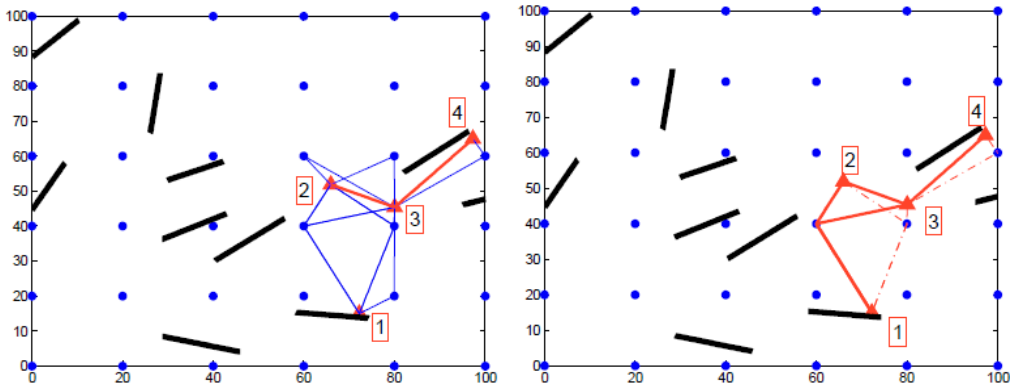

(a) The network before RMRP (b) The network after RMRP

Fig. 2. Performance of RMRP.

Fig. 2(b) shows the result of RMRP, where solid red lines are the primary paths, and dashed lines are the secondary paths. Only three reflectors are used after applying RMRP.

References

[1] C. Anderson and T. Rappaport, "In-building wideband partition loss measurements at 2.5 and 60 GHz," *IEEE Trans. on Wireless Comm*, vol. 3, no. 3, pp. 922–928, May 2004.

[2] F. Giannetti, and etc, "Mobile and personal communications in the 60 GHz band: A survey," *Wireless Personal Comm*, vol. 10, no. 2, pp. 207–243, July 1999.

[3] C. Yiu and S. Singh, "Empirical capacity of mmwave wlans," *IEEE Journal Selected Area in Communications*, vol. 27, no. 8, pp. 1479–1487, Oct. 2009.

[4] S. Singh, R. Mudumbai, and U. Madhow, "Interference analysis for highly directional 60-GHz mesh networks: The case for rethinking medium access control," *IEEE/ACM Transactions on Networking*, vol. 19, no. 5, pp. 1513 – 1527, Oct 2011.

RECONFIGURABLE ROUTER DESIGN IN DWDM-BASED NETWORKS

Wenhao Chen*, Linsen Wu, Lei Wang, and Yuhua Chen
Systems Research Laboratory
Department of Electrical and Computer Engineering
University of Houston
Houston, TX 77204-4005

Abstract

As the data transmission speed increases in the fiber network, single switching method cannot cost effectively meet the requirements of heterogeneous services. *Reconfigurable Asymmetric Optical Burst Switching* (*RA-OBS*), which allows different switching methods working in the same *dense wavelength division multiplexing* (*DWDM*) [1] network, is proposed to solve the dilemma. In this paper, we present burst scheduling schemes for the DWDM multi-mode switching router. We also evaluate the burst blocking probability under limited *optical to electrical* (*O/E*) and *electrical to optical* (*E/O*) converters. The results will shed light on future *RA-OBS* router designs.

Introduction

There are three principle switching technologies in the current *DWDM* network. Inherited from electrical packet switching, optical packets in *electrical packet switching* (*EPS*) mode are converted to the electrical domain at each hop. Similar to the circuit switching in traditional *public switched telephone networks* (*PSTNs*), the control signals in *optical circuit switching* (*OCS*) informs the core node to create an optical path exclusively for the service before the establishment of the service. In the *optical bursting switching* (*OBS*) mode [2], a control packet manages the lightpath configuration ahead of the data burst transmission. The data bursts arrive later take advantage of the transparent optical domain transmission, thus eliminating the use of *O/E* and *E/O* converters. The proposed *RA-OBS* router makes full use of the above three switching technologies.

Methodology and Results

The evaluation of the *RA-OBS* router consists of both the hardware testbed design and software simulation. In the hardware design, we verified the effectiveness of the *RA-OBS* scheduling and implemented the scheduler in the FPGA using Verilog-*HDL* (*hardware description language*) with a pipeline design method. In order to test the effectiveness of the scheduler, we created different scheduling scenarios in our testbed. In Fig. 1, we show

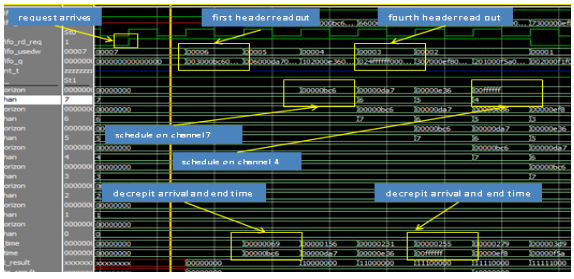

Fig. 1. Circuit simulation of concurrent *EPS* setup and *OBS* burst scheduling in hardware testbed

the operations of concurrent *EPS* setup and *OBS* burst scheduling. Each configuration scheduling request can be complete in O(1) runtime.

We also evaluated the burst blocking probability versus the number of electronic switching ports allocated for wavelength conversion in the *OBS* mode using software simulation. Each *DWDM* link carries 12 data channels. The control channel has no packet drop. The bandwidth of each channel is set to 10 Gigbits per second. Traffic arrival follows a Poisson process with a traffic rate of 10 Gigbits per second during the ON_TIME, and a traffic rate of 0 during the OFF_TIME. We define the traffic load as ON_TIME by OFF_TIME. The result in Fig. 2 shows improvement of blocking probability when more *O/E/O* ports are assigned to the *OBS* mode. The *O/E* and *E/O* converts can be configured to *share per link* (*SPL*), or *share per node* (*SPN*). This becomes an important design consideration especially when the traffic is asymmetric. We evaluated the case where one core node needs to deliver traffic to two edge nodes but each edges has a different traffic demand. As shown in Fig. 3, the SPN design performs much better than when the traffic load among different ports are asymmetric.

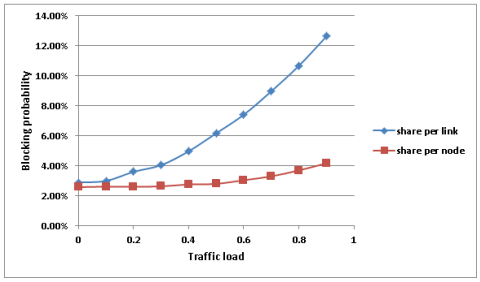

Fig. 2. Burst blocking probability in share per link and share per node configuration

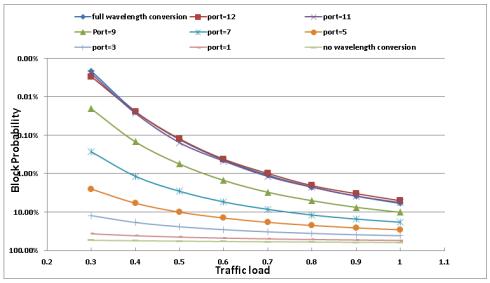

Fig. 3. Burst blocking probability versus number of *O/E/O* ports assigned

Conclusion

The paper proposed a new asymmetric router design. We have implemented the scheduoing algorithms in the FPGA hardware for the network testbed. The traffic blocking probability of the *RA-OBS* router is also evaluated under limited *O/E* and *E/O* converter conditions. For asymmetric traffric, the effectiveness of the *SPN* configuration is also verified in the router design.

Acknowledgment

This work was supported in part by the *National Science Foundation* (*NSF*) under Grant CNS-0708613, 0923481, 0926006, and the *Texas Advanced Research Program* (*ARP*) under Grant G096059.

References

[1] Y. Chen, W. Tang, "Concurrent DWDM Multi-Mode Switching: Architecture and Research Directions," *IEEE Communications Magazine*, May 2010.

[2] Y. Chen, P. Verma, "Optical burst switching – an emerging core network technology," *Internet Networks – Wired, Wireless, and Optical Technologies*, K. Iniewski, Ed. CRC Press, Taylor & Francis Group, pp. 265-290, 2010.

REAL-TIME DYNAMIC RESOURCE SHARING FOR SCALABLE RECONFIGURABLE ASYMMETRIC OPTICAL ROUTERS

Vikram Shete* and Yuhua Chen
Systems Research Laboratory
Department of Electrical and Computer Engineering
University of Houston
Houston, TX 77204-4005

Abstract

Dense Wavelength Division Multiplexing (*DWDM*) is a promising solution for next generation networks. However an all-optical-packet switched *DWDM* network cannot be practically realized due to limitations on optical technologies. We explore the possibility of using a hybrid approach by leveraging the electronic buffering options while retaining majority of network traffic in the optical domain. Traditional allocation methods rely upon available optical channels and their usage. In this work we deploy the Optical/Electrical/Optical (O/E/O) channels based on real-time measurements of load-variation experienced by the output ports. Blocking probability is used as a performance metric to determine resource allocation. Preliminary results indicate that real-time dynamic resource sharing over optical routers with large channel counts can be achieved in terms of blocking, energy consumption, and resource utilization.

Introduction

Optical technologies have proven to be the perfect solution to the ever increasing bandwidth requirements. Coupled with *DWDM,* it can offer bandwidths exceeding terabits. However this has pushed the contemporary electronics to its intrinsic limit. Consider a typical example where a single link carries 500 channels each with a capacity of 10 Gbps in a router with 16 ports. At the peak of the operation this optical router processes 80 Tb of data per second. This is extremely expensive to build an electronically packet switched router of such capacity due to O/E/O conversion. All optical packet switched networks are not amenable as short duration light pulses cannot be stored in large amount for a longer duration. Large buffers are at the heart of packet switching. Hence recently the research community has looked into hybrid shared-buffer techniques [1] . In our work, we provide electronic buffering to optical circuit switching and optical burst switching only during contention among bursts and/or circuits and electronic packet arrivals, allowing majority of the traffic to pass the router optically, which significantly reduces the cost and energy consumption of the routers.

Methodology

In this work we explore the possibility of real-time allocation and sharing of resources and performance of such policies. More specifically, we propose a *Dynamic Resource Allocator* (*DRA*) for a *Multi-mode Reconfigurable Asymmetric OBS* (*RA-OBS*) router [2]. The *DRA* executes a real-time algorithm, which considers past variations in load and blocking as inputs to predict the future needs. It then assigns additional resources to the needy ports or demand resources from affluent ports. The *DRA* monitors real time performance of all ports and compares it with a built-in optimized performance database. It then creates a difference map as shown in Fig. 1 and re-allocates resources. A difference map gives a snapshot of all transactions the *DRA* must perform in order to

keep the overall penalties to minimum. A high penalty is incurred during a transaction with a stable port whereas a lower penalty is incurred while dealing with a port with larger load variations. Fig. 2 shows the blocking probability with and without the proposed DRA algorithm.

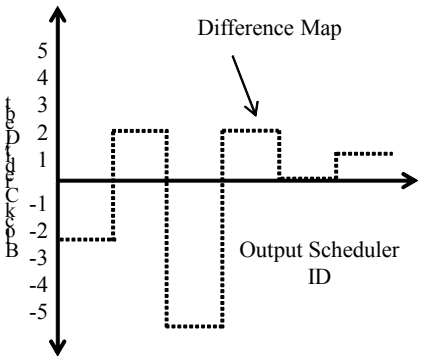

Fig. 1 Difference map

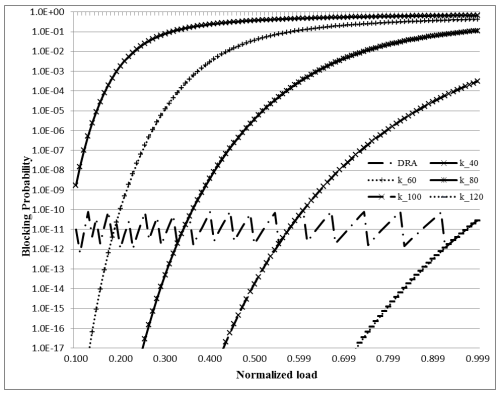

Fig. 2 Blocking probability with and without DRA

Error! Reference source not found. shows the performance of the router with and without the proposed *DRA* mechanism. The popular notion is that the blocking probability increases with increasing load for a given number of resources (servers). However every time resources increase blocking decreases. Our algorithm aims at ensuring that the blocking probability of any given output port remains within a desirable range or as determined by the operator without increasing the total resources of the router.

Conclusion

We present a novel technique of leveraging electronic buffering by sharing the expensive O/E/E ports among different switching modes within a reconfigurable asymmetric optical router. Our approach embeds a mathematical model into the system for improving performance. Hybrid resource sharing is a promising approach for large-scale DWDM networks. In future we will evaluate the performance of our architecture under a variety of load distributions for different applications.

Acknowledgment

This work was supported in part by the National Science Foundation (NSF) under Grant CNS-0708613, 0923481, 0926006, and the Texas Advanced Research Program (ARP) under Grant G096059.

References

[1] Z. Zhenghao and Y. Yuanyuan, "Performance analysis of Optical Packet Switches enhanced with electronic buffering," in *Parallel & Distributed Processing, IEEE International Symposium on*, pp. 1-9, 2009.

[2] Y. Chen and W. Tang, "Reconfigurable asymmetric optical burst switching for concurrent DWDM multimode switching: architecture and research directions

[Topics in Optical Communications]," *Communications Magazine, IEEE,* vol. 48, pp. 57-65, 2010.

DESIGN AND CHARACTERIZATION OF METAL-POLYMER BASED ARTIFICIAL CORE-SHELL NANO DIELECTRICS FOR CAPACITOR APPLICATIONS

D. Musuwathi Ekanath*[1], A. Bensaoula[1,2], N. Badi[3] and D. Starikov[3]
[1] Department of Electrical and Computer Engineering
[2] Department of Physics
University of Houston
Houston, TX-77204-4005
[3] Integrated Micro Sensors, Inc.
10814 Atwell Drive, Houston, Texas 77096

Abstract

This paper summarizes our results on loading of silver nano particles, coated with either silica or a polymer, in a polymer matrix. Polymers have great processability, mechanical flexibility and electrical break down strength, but possess very low dielectric strength. The dielectric properties of the polymer can be tuned to desired characteristics by introduction of nano fillers. Effective medium theories are used for theoretical predictions. COMSOL multiphysics software is used to simulate the nano particles in a polymer medium.

Introduction

More than 40% of devices in a modern electronic board are passive devices. The passive devices are charge storage devices, rather than charge driving devices. Hence reduction in the size of these passive devices, without degrading their performance should free a large amount of space on general printed circuit boards. Extensive interest is being directed toward research of nano dielectrics because of their promising applications in energy storage solutions as both discrete and embedded capacitors. There is growing demand for capacitors that can store a large amount of energy and deliver it instantaneously.

Increasing Capacitance

The general capacitor equation is given by

$$C = \frac{\varepsilon A}{d} \tag{1}$$

Where C is the capacitance, Ɛ is the dielectric constant, A is the area of the metal plates and d is the distance of separation. Increasing the area would in turn, consume more space on the board. By decreasing the distance between the plates, a very small applied voltage can cause shorting of the metal plates. Hence the only possible way to increase the capacitance without degrading any of its properties is to increase the dielectric constant. The dielectric constant can also be termed as relative permittivity.

The polymer dielectrics, as mentioned previously, may have very low value of permittivity. Introduction of metal nano fillers, increases the dielectric constant of the polymer, but brings down its dielectric strength. Hence there should be a proper trade-off in maintaining both properties. The loading of the metal nano particles, shouldn't

increase beyond a particular threshold value, after which the polymer acts as a conductor, rather than a dielectric. This threshold is called the percolation threshold. The effective permittivity is at its maximum possible value at this threshold. The loading corresponding to this threshold is called the critical fraction of loading. The dielectric constant of the polymer used in this case is around seven.

Predictions and Results

The effective medium theories and percolation theory have been implemented to predict the possible dielectric constant at particular fraction of loading. The percolation theory proved to be better than that of the effective medium theory, since the effective medium theory neglects the metal-polymer interaction at high frequencies. Drude-Loentz model was used to determine the dielectric constant of the silver nano particle. The percolation theory predicted the dielectric constant as high as 1400 at a fraction of loading 0.16. The laboratory experiments led to the result of 40.67. The fraction of loading corresponding to this result is predicted to be around 0.04, using percolation theory.

Conclusion

The dielectric constant thus has been increased from 7 to 40.67. The implementation of this dielectric in capacitors can increase its performance multiple times, by using a very small space on a board. The same dielectric could also be used instead of a gate insulator in a CMOS device. However, device integration issues are far too complicated for easy adaptation of this process directly.

References

[1] K.W. Jacobsen, P. Stoltze and J. K. Nørskov, "A semi-empirical effective medium theory for metals and alloys", *Surf. Sci.* vol. 366, p. 394, 1996.
[2] Geoffrey Grimmett, "*Percolation*", Springer link, 1991.
[3] D. Musuwathi Ekanath, N. Badi, A. Bensaoula, "Modeling and Simulation of Artificial Core-Shell Based Nanodielectrics for Electrostatic Capacitors Applications" *COMSOL conference*, Boston, 2011.

PHOTOLUMINESCENCE PROPERTIES OF SILICON NANOWIRES

Yang Li* and Jiming Bao
Bao Research Group
Department of Electrical and Computer Engineering
University of Houston
Houston, TX 77204-4005

Abstract

Silicon nanoscale materials have promising optoelectronic properties and attractive for photonic applications. In this report, we studied the photoluminescence (PL) effect of the silicon nanowires excited by 532nm laser. Two PL bands were detected in our study. The origin of this IR band is discussed. Laser-induced thermal effect on the Si nanowires is observed and discussed.

Introduction

The indirect band gap structure of bulk Si limits its application in the optoelectronics field due to the low efficiency in light emitting. Si nanostructures, such as Si nanowires and Si nanocrystals have been suggested to be the candidate to solve the problem. In 1990, L. T. Canham reported the strong PL effect on porous Si [1]. So far, the PL band around 1.6 eV attracts most of the attention. The mechanism of this band is still under debate. Possible explanations include quantum confinement effect, surface state, and defect-center luminescence [2]. As a contrast, little work has been done about the PL in the IR band and we tried to clarify the reason for this PL band.

High power laser can increase the local temperature of the Si nanowires, which will do damage to the sample. High temperature will result in blackbody radiation that could affect the light emission spectrum [3]. Taken these factors into consideration, we place the Si nanowire in water so as to minimize the laser-induced heat effect.

Experiment and Results

The Si nanowire used in the experiment is shown in fig.1.

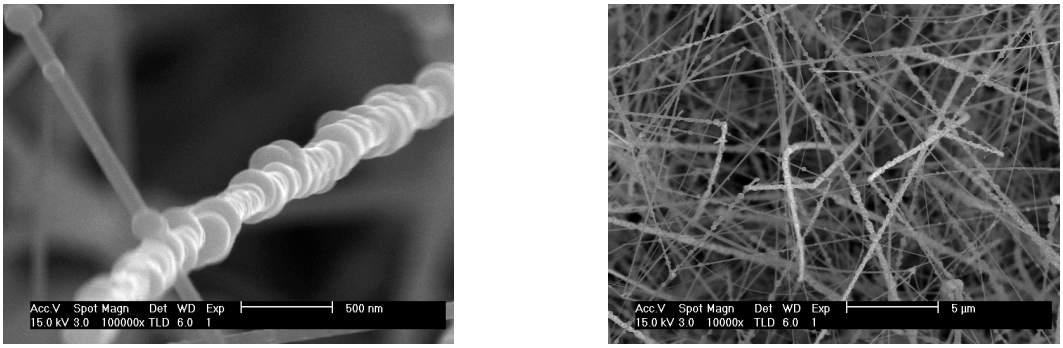

a b

Fig. 1. SEM image of the Si nanowires

We observed two PL bands, one around 750 nm and the other around 950 nm, as shown in Fig.2. The PL band around 1.6 eV is much stronger than it is in the IR band. As the power of the laser increased, the intensity of the light emitted increased as well. By measuring the Raman spectrum, we can calculate the temperature of the sample. Further work will be done to determine the origin of the two PL bands.

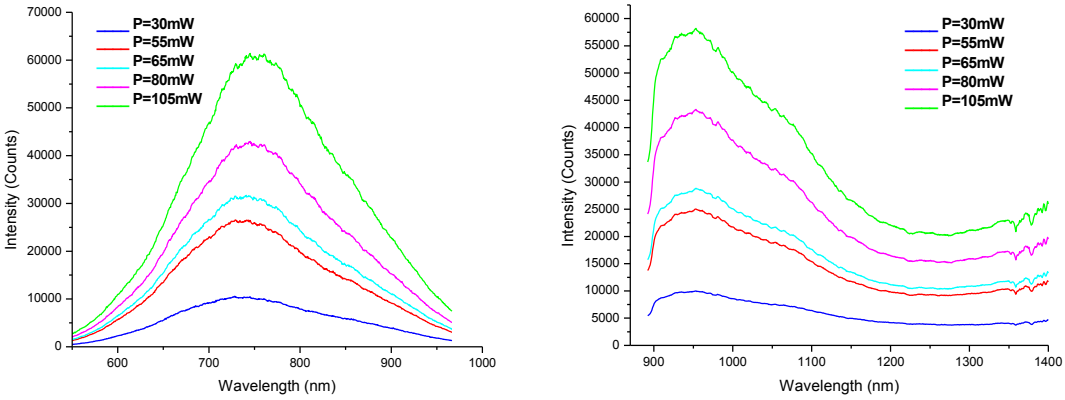

Fig. 2. PL spectra of Si nanowires. (a) exposure time = 0.1s; (b) exposure time = 2s

References

[1] L. T. Canham, "Silicon quantum wire array fabrication by electrochemical and chemical dissolution of wafers," *Appl. Phys. Lett.*, vol. 57, pp. 1046-1048, Sep. 1990.

[2] L. H. Lin, X. Z. Sun, R. Tao, Z. C. Li, J. Y. Feng, and Z. J. Zhang, "Photoluminescence origins of the porous silicon nanowire arrays," *J. Appl. Phys.,* vol. 110, Oct. 2011.

[3] L. Khriachtchev, "Optical and structural properties of silicon nanocrystals and laser-induced thermal effects, " *J. Electrochem. Soc.,* Vol. 159, pp. K21-K26, 2012.

ELECTROCHEMICAL SYNTHESIS OF MAGNETIC MATERIALS AND NANOSTRCUTURES FOR MGNETIC RECORDING AND MEMS APPLICATIONS

Jinnie George*[1], Rachit Sharma[2], and Stanko R.Brankovic[1]
Electrochemical Nanofabrication and Nanomaterials Synthesis Group
[1] Department of Electrical and Computer Engineering
[2] Department of Industrial Engineering
University of Houston
Houston, TX 77204-4005

Abstract

CoFe alloys have been extensively used in the fabrication of magnetic recording heads. One of the most important parts in these devices is the magnetic read head sensor. In this work, we have presented the magnetoresistance curves for electrodeposited nanocontacts, which demonstrate very high magnetoresistance values. These sensors are crucial in achieving high storage capacity for hard disks.

Introduction

Research in the recording industry is fueled by the need to increase the areal density or the number of bits stored in a unit area. This means that more number of bits are packed in a square inch of disk, compelling research to make bit size smaller. In order to make the bits readable, the signal to noise ratio should be sufficiently high, meaning that the magnetoresistance ratio should be high. Hence, industry made a transition from inductive thin film heads to the GMR (Giant Magnetoresistive) and TMR (Tunneling Magnetoresistive) heads. The ballistic magnetoresistance (BMR) phenomenon has succeeded in giving MR values as high as 3000% and these structures were produced by electrodeposition [1, 2]. However, there have been many controversies over the BMR phenomenon and the fabrication techniques [3]. In order to avoid these issues, a new technique was devised to build these electrodeposited nanocontacts. These nanocontacts showed properties related to both the ballistic and tunneling magnetoresistance.

Results and Discussions

We used a top down approach to build these read sensors. The nanocontact has been electrodeposited with CoFe and this structure was sandwiched in between two magnetic layers of Permalloy and Cobalt. The diameter of these nanocontacts is of the order of around 60 nm. We devised more than 100 such sensors and the nanocontacts were electrodeposited with CoFe with different concentrations of Fe^{3+} and saccharin and tried to understand the MR values as a function of the contact resistance. These alloys also had minimum values of stress and the in-situ stress was determined previously in our lab.
One such magnetoresistance curve is as shown in figure 1. These experiments have been repeated and show good reproducibility. The MR values are as high as about 1000%. Sometimes there is an inversion of the MR curves as shown in figure 2. This is a property of the TMR devices and this phenomenon is called as Resonant Tunneling of the devices [4]. We observe that there is a universal scaling principle that is observed. The universal scaling principle is a property of the ballistic magnetoresistance devices. Thus the mechanism involved in the functioning of these devices is still not clear and can be a combination of the BMR and TMR devices. If the domain wall width is less than the mean free length of the nanocontacts, then the reflection in case of spin up and spin

down electrons is very high, resulting in a very high resistance.

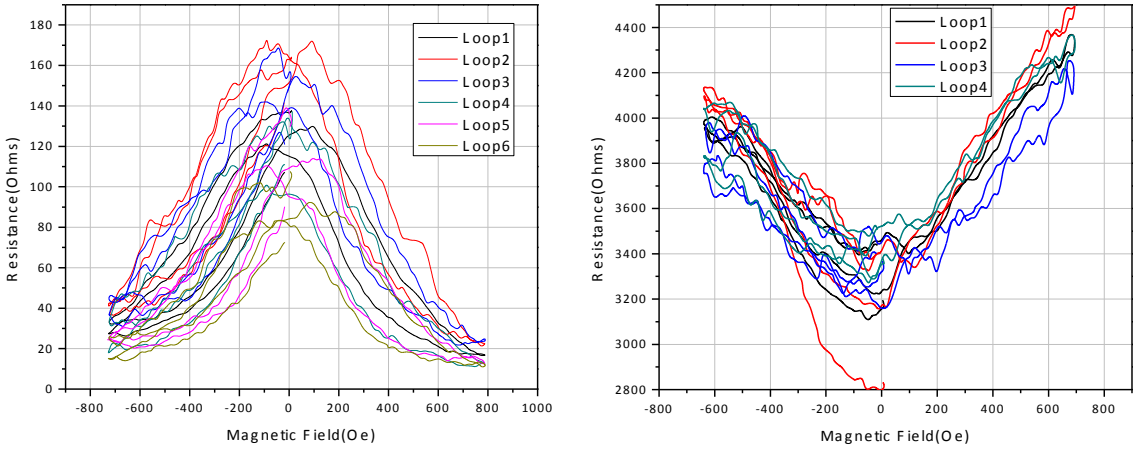

Fig 1: (left) A typical MR curve for nanocontact with diameter ~60nm and (right) Inversion of MR curves.

Conclusion and Future Work

The top-down nanocontact devices that were built did not have an issue of the unknown oxide formation and also showed promising results in terms of the MR values. The next step in this project would be to perform the low temperature measurements to determine whether the device functions like BMR or TMR device. This can be understood by studying the IV curves of these devices at temperatures as low as 4K. The IV curve is a characteristic of a device and shows linear or conductive (ohmic) curve if it is a BMR device and exponential curve if it works by the principle of tunneling.

References

[1] Garcia, N., et al., "Negative and positive magnetoresistance manipulation in an electrodeposited nanometer Ni contact", *Physical Review Letters*, **85** (14), pp. 3053-3056, 2000.
[2] Chopra, H.D. and S.Z. Hua, "Ballistic magnetoresistance over 3000% in Ni nanocontacts at room temperature", *Physical Review B*, **66** (2), p. 020403, 2002.
[3] Egelhoff, W.F., et al., "Artifacts in ballistic magnetoresistance measurements" (invited), *Journal of Applied Physics*, **95** (11), pp. 7554-7559, 2004.
[4] Tsymbal, E.Y., O.N. Mryasov, and P.R. LeClair, "Spin-dependent tunnelling in magnetic tunnel junctions", *Journal of Physics-Condensed Matter*, **15** (4), pp. R109-R142, 2003.

NEURAL CORRELATES OF PATH GUIDED APPARENT MOTION PERCEPTION USING FMRI: A PRELIMINARY STUDY

Michel Akselrod*[1,2], Michael Herzog[2], and Haluk Ogmen[1]
Center for Neuro-engineering and Cognitive Science
[1]Department of Electrical and Computer Engineering, University of Houston
[2]Brain & Mind Institute, LPSY, EPFL

Abstract

We present our preliminary results from a study where we investigated the spatial specificity and selectivity of the perceptual filling-in process during apparent motion perception [2]. A paradigm called path guided apparent motion [1] allows to displace the perceived path of motion towards an arc shaped luminance cue. It was used to compare fMRI BOLD signals during path guided apparent motion and linear apparent motion perception at locations close to the V1 representations of both paths of motion. Results show that BOLD signals are higher at locations corresponding to their respective percept. This suggests that low-level visual information from early visual areas is integrated in the computation of perceived motion and used for filling-in the perceived path of motion in early visual areas.

Introduction

Perception of moving objects is one of the most important processes carried out by the visual system for our understanding of the world. But how is motion computed in the visual system ? The most simple explanation is that successive stimulations of adjacent receptive fields creates a "path of motion". This mechanism is implemented in the so-called spatiotemporal receptive fields. During perception of apparent motion, two spatially distinct stimuli are successively flashed and intermediate receptive fields on the path of motion are not physically stimulated. However, observers still experience smooth motion perception. Apparent motion perception has been observed over larger distances than the size of these spatiotemporal receptive fields [2]. Therefore another mechanism must be underlying this process. Recent studies have determined that a perceptual filling-in process occurs in early visual areas [2]. In the present study, a paradigm called path guided apparent motion is used to investigate the spatial specificity and selectivity of the filling-in process. For simple apparent motion, a square is displayed in the upper-right part of the screen for the first frame and in the lower-right part for the second frame, with an ISI between the two frames (150ms-ISI-150ms), resulting in the perception of straight vertical motion (Fig.1). For path guided apparent motion, the same stimulus is used except that an arc shaped luminance cue is flashed for 10 ms after 20 ms of ISI, resulting in the perception of curved motion (Fig.2). Therefore low level information is somehow integrated and interpreted during the process underlying apparent motion perception. Furthermore it seems that during this process surrounding regions adjacent to the most probable path of motion (linear) are also considered. Using fMRI as imaging tool, the retinotopic specificity and selectivity of the filling-in process is evaluated by comparing BOLD signals for different experimental conditions.

Fig.1: Linear Apparent Motion with perception of straight motion

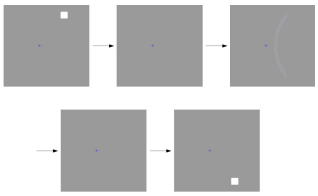

Fig.2: Path Guided Apparent Motion with perception of curved motion

Experimental Procedure

Cortical representations of different parts of both types of motion were first mapped. Then fMRI data were collected for passive viewing of six experimental conditions: apparent motion, real motion, flicker (squares simultaneously flickering), path guided apparent motion, curved real motion and flickering luminance cue. Using GLM analysis, BOLD signals for each conditions were compared for regions close to V1 representations of both paths of motion. The expected results are summarized in Table1.

Table 1: Expected results according to retinotopic strength of stimuli and potential horizontal spreading of signals

Midpoint of	**Highest signal**					**Lowest signal**
Straight motion	Real motion	Apparent motion	Curved real motion	P. g. apparent motion	Flickering cue	Flicker
Curved motion	Curved real motion	P. g. apparent motion	Flickering cue	Real motion	Apparent motion	Flicker

Results

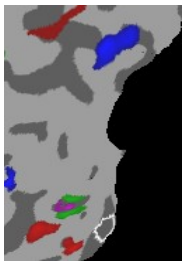

Fig.3: V1 representations of upper square (red), lower square (blue), midpoint of motion path for straight motion (green), curved motion (pink), selected patch for analysis (white)

The mapping of cortical representations of upper square (red), lower square (blue), midpoint of motion path for straight (green) and curved (pink) motion are presented in Fig.3. BOLD signals % change for a selected patch on linear motion path (averaged over white patch) are shown in Fig.4 and for the location on curved motion path (averaged over pink patch) in Fig.5.

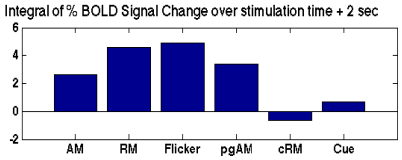

Fig.4: Integral of % BOLD Signal change for path of linear motion (averaged over white patch)

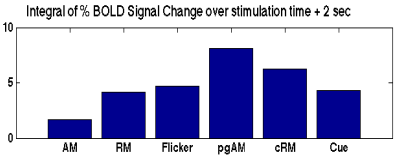

Fig.5: Integral of % BOLD Signal change for path of curved motion (averaged over pink patch)

Discussion

In this preliminary study, we collected and analyzed data only from a single subject. Some predicted results are observable. High response for path guided apparent motion condition on the path of straight motion and high response for flicker condition for both paths of motion are hard to explain. Future experiments will have more subjects and will include attentional control as well as mapping of the whole paths of motion.

References

[1] R. N. Shepard, S. L. Zare, "Path-Guided Apparent Motion", *Science 1983 May*
[2] L. Muckli, A. Kohler, N. Kriegeskorte, W. Singer, "Primary Visual Cortex Activity along the Apparent-Motion Trace Reflects Illusory Perception", *PLoS Biol. 2005 August*

STATISTICAL MODELING OF VISUAL MASKING

Sevda Agaoglu*, Mehmet N. Agaoglu, and Haluk Ogmen
Center for Neuro-Engineering and Cognitive Science
Department of Electrical and Computer Engineering
University of Houston

Abstract

Visual masking is defined as the reduction in visibility of one stimulus, called the target, by another stimulus, called the mask. It is a well-known and widely-used paradigm. The goal of this study was to investigate if the masking effect results from an increase in guess rate (modeled as the weight of a uniform distribution in a mixture model) or from a decrease in stimulus encoding precision (modeled by the inverse of the variance of a Gaussian distribution). Results show that reduced encoding precision provides a more parsimonious explanation than an increase in guess rate for the masking effects in the masking by noise paradigm.

Introduction

Visibility of a stimulus, called the target, can be reduced by a second, spatio-temporally overlapping or flanking stimulus, called the mask. This phenomenon is called visual masking. Masking can be divided into categories (see Fig. 1) in terms of temporal aspects (*forward and backward masking*) and spatial aspects (*para-metacontrast, noise and pattern masking)* [1]. In this study, we aim to shed light on how masking occurs from a statistical perspective. How does the mask affect the visibility of the target? Does the signal produced by the mask increase the guess rate or decrease the precision of the mechanisms encoding features of the target?

Methods

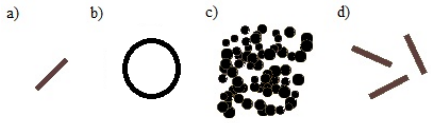

Fig. 1. Stimuli configurations
a) Target
b) Para-Metacontrast mask
c) Noise mask
d) Pattern mask

Subjects were asked to fixate at the center of a screen placed 100 cm away. Target and mask pair given in Fig. 1a and 1c, respectively, were presented at 6 deg eccentricity. Stimulus onset asynchrony (SOA), i.e., the time delay between the onset of the target and the onset of the mask, (ranged from -100 to 150 ms). Target and mask durations were 10 ms. The task was to report the orientation angle of the target bar. Error was calculated as the difference between reported and actual angles for each trial. Error values were binned and normalized to extract the probability density functions for each SOA value. We fitted the models shown in Fig. 2 to determine the contributions of each factor. Five subjects participated in the experiments.

Results and Discussion

Fig. 3A shows the masking function for one subject. A sample error PDF and the corresponding fits of Gaussian and Gaussian+Uniform mixture models are shown in Fig.

3B, for SOA = -10 ms. 3C provides an example of how model parameters vary as a function of SOA.

Finally, Fig. 3D is an illustration of the plots of residuals for a fixed SOA. Analysis of the entire data set by Kolmogorov-Smirnov test shows that the Gaussian+Uniform mixture model performs slightly better than the Gaussian model. In order to take into account the differences in the number of parameters in the two models, we run a repeated-measures ANOVA on adjusted R^2 coefficients obtained from the two models. This analysis shows no significant difference between the two models [$F_{1,4}$=2.13, p=0.218].

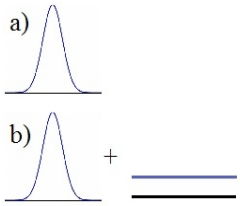

Fig. 2. Models
a) Gaussian
b) Gaussian + Uniform

Conclusion

A process whereby the mask reduces the precision of encoding provides a more parsimonious explanation than an increase in the guess rate for the masking effects in the masking by noise paradigm.

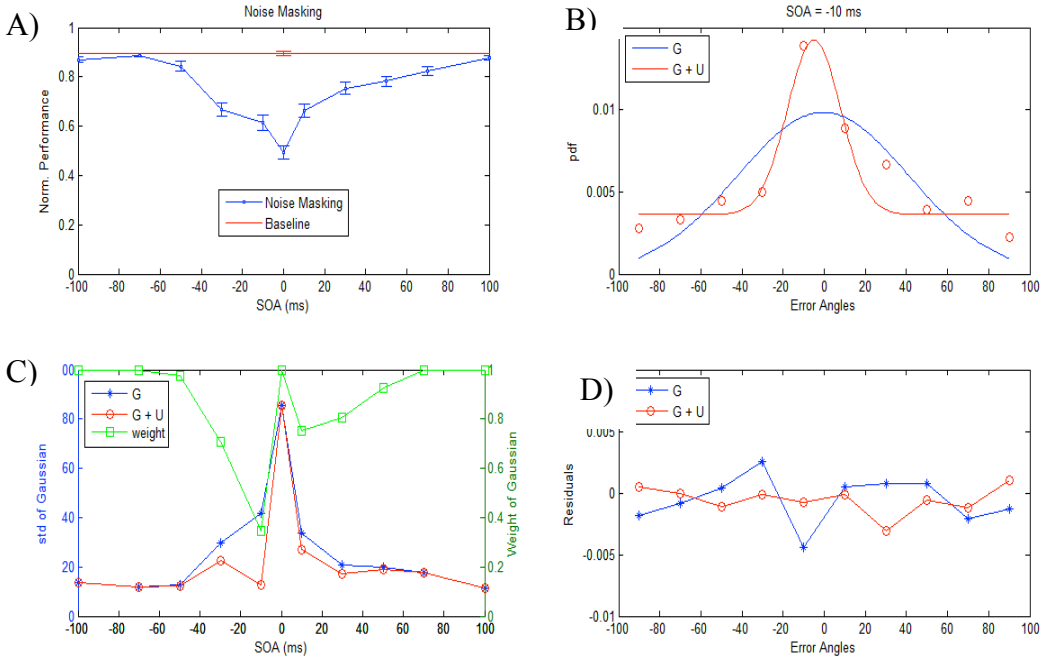

Fig. 3. (A) Masking function for noise masking from one subject. Error bars represent +/-1 SEM. (B) Illustration of error distribution for SOA -10ms. Red curve shows the best fit for Gaussian+Uniform model and blue curve represents the best fit of the Gaussian model. (C) Standard deviation of the Gaussian component in each model is plotted against SOAs. Green curve shows the weight of the Gaussian distribution in the mixture model. (D) An example of residual distribution. All results are from observer GJ.

References

[1] Breitmeyer, B. G. and Ogmen, H., *Visual masking: Time slices through conscious and unconscious vision* (2nd edition). Oxford, UK: Oxford University Press, 2006.

TESTING STATISTICAL MODELS FOR MULTI-ATTRIBUTE ENCODING OF MOVING STIMULI

D. Huynh*, S. P. Tripathy, H. E. Bedell, H. Öğmen
Center for Neuro-Engineering and Cognitive Science
Department of Electrical and Computer Engineering
University of Houston
Houston, TX 77204-4005

Abstract

In this research, we tested whether statistical models of memory can explain how different features of moving objects, viz. motion direction, position, and color, are encoded. Statistical modeling was implemented so as to decompose behavioral data in terms of components whose parameters allowed us to analyze and compare predictions of each model. We found that none of the proposed models was consistent with the results. We suggest that a hybrid model must be constructed to fully characterize the properties of stimulus encoding.

Introduction

VWM refers to the memory system that stores visual information for short periods of time. Recent studies lead to several competing models of VWM. The first model claims that VWM consists of a fixed number of discrete "*slots*", which are capable of holding four to five visual items, one in each slot. The second one suggests that VWM is a single limited memory "*resource*" divided among all items. In addition, there are two alternatives called "*slots + resources*" and "*slots + averaging*" [2]. Similar to the "*slots*" model, these two models also consist of a fixed number of memory slots, but a shareable resource can be distributed unequally between them. The key differences between the models are: (1) whether or not a capacity limit is involved; and (2) how the precision of storing each item depends on the number of visual items. Since the capacity and precision of VWM may be partly decided by the encoding process, the present study was designed to examine if these models were applicable to this stage of information processing based on the distinct predictions they make on observers' performance in a Multiple-Object-Tracking (MOT) task.

Methods

We extended the method and the MOT paradigm used in [1] for multiple stimulus attributes. In addition to direction of motion and position, we also used object color in our study. We presented observers (N=4) with a number of circular moving objects of unique colors on the display. After objects stopped moving, they were immediately removed from the display and the observers were asked to report the remembered motion direction or position or color of a randomly selected object. Here, we applied the cross-feature cuing technique, where one feature was used as a cue to report another feature, for all combinations of the three object features. We then measured response errors and carried out statistical modeling of error distribution for each feature. The distribution of error can be described by the following equation:

$$P_\theta(\theta) = (w)N(\mu_t, \sigma_t) + (1 - w - m)U(-180,180) + (m)S_{i=1;i\neq t}^{T}[N(\mu_t + \theta_{i,t}, \sigma_m)] \,.$$

where $P_\theta(\theta)$ is the PDF function of error variable θ. The first two terms in the right-hand-side (RHS) represent responses to the target object selected for report (Gaussian distribution with mean μ_t and standard deviation σ_t) and random guesses (Uniform Distribution). The third term in the RHS corresponds to misbinding/confusion responses, in which the observer gets confused and reports another object instead of the cued target. $S_{i=1;i\neq t}^{T}[.]$ denotes a selection operator implying that we are selecting from (*T-1*) non-target objects the object that is most likely causing confusion. The third term is also a Gaussian with mean shifted by $\theta_{i,t}$ from the first Gaussian and standard deviation σ_m (Note that $\sigma_m = \sigma_t$). *w* and *m* are the weighting factors of the first and third terms, respectively. Fig.1 shows the predictions of the four models on the parameters σ_t (standard deviation = precision^{-1}) and *1-w-m* (guessing rate).

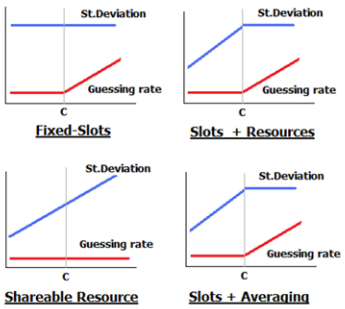

Fig.1. Predictions of the four models: Std.Deviation and Guessing Rate as functions of the number of visual items. C represents the theoretical capacity limit (typically 4-5 items)

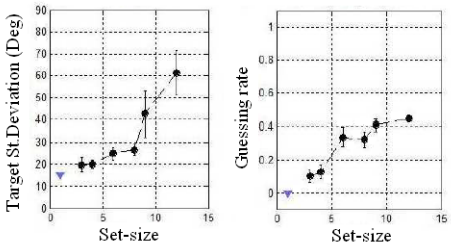

Fig.2. Mean Std.Deviation and Guessing Rate as functions of set-size (seven set-sizes were used: 1, 3, 4, 6, 8, 9, 12). The triangles show the results for the case of single object (set-size=1). Error bars correspond +/-SEM

Results

We applied Maximum Likelihood method with the Expectation Maximization algorithm to obtain estimates of the parameters above. In all cases, we observe a linear increase of both the standard deviation (SD) and the guessing rate (GR). Results from a two-way repeated-measured ANOVA with cue-type and set-size as two factors show significant main effect of set-size in all cases (**Cue Position/Color - Report Direction** SD: $F(5,15)=7.164$, $p=0.0013$; GR: $F(5,15)=23.46$, $p<0.0001$; **Cue Position/Direction - Report Color** SD: $F(5,15)=11.28$, $p=0.0001$; GR: $F(5,15)=19.39$, $p<0.0001$; **Cue Direction/Color - Report Position** *(reported separately for the horizontal-x and vertical-y components)* SDx: $F(5,15)=3.12$, $p=0.0379$; SDy: $F(5,15)=9.691$, $p=0.0003$; GRx: $F(5,15)=9.721$, $p=0.0003$; GRy: $F(5,15)=10.98$, $p=0.0001$). Figure 2 shows the results for the case of cueing color and reporting motion direction.

Conclusions

None of the proposed models is sufficient to explain the data. A hybrid model, which takes into account other factors, such as visual attention and eye movements, is necessary to describe feature encoding.

References

[1] C. Shooner, S. Tripathy, H. Bedell, and H. Öğmen "High-capacity, transient retention of direction-of-motion information for multiple moving objects", *Journal of Vision*, 10(6):8, 1-20, (2010).

[2] W. Zhang, and S. J. Luck "Discrete fixed-resolution representations in visual working memory", *Nature*, 453, 233-235, (2008).

AUTHOR INDEX